



저작자표시-비영리-변경금지 2.0 대한민국

이용자는 아래의 조건을 따르는 경우에 한하여 자유롭게

- 이 저작물을 복제, 배포, 전송, 전시, 공연 및 방송할 수 있습니다.

다음과 같은 조건을 따라야 합니다:



저작자표시. 귀하는 원저작자를 표시하여야 합니다.



비영리. 귀하는 이 저작물을 영리 목적으로 이용할 수 없습니다.



변경금지. 귀하는 이 저작물을 개작, 변형 또는 가공할 수 없습니다.

- 귀하는, 이 저작물의 재이용이나 배포의 경우, 이 저작물에 적용된 이용허락조건을 명확하게 나타내어야 합니다.
- 저작권자로부터 별도의 허가를 받으면 이러한 조건들은 적용되지 않습니다.

저작권법에 따른 이용자의 권리는 위의 내용에 의하여 영향을 받지 않습니다.

이것은 [이용허락규약\(Legal Code\)](#)을 이해하기 쉽게 요약한 것입니다.

[Disclaimer](#)

이학박사 학위논문

**Synthesis of Plasmon-Enhanced  
Fluorescence-Active Nanostructures and  
Their Applications**

플라즈몬 강화 형광 활성 나노구조의 합성 및 응용

2021년 2월

서울대학교 대학원

화학부 무기화학

황재호



# Synthesis of Plasmon-Enhanced Fluorescence-Active Nanostructures and Their Applications

플라즈몬 강화 형광 활성 나노구조의 합성 및 응용

지도교수 남 좌 민

이 논문을 이학박사 학위논문으로 제출함

2021년 2월

서울대학교 대학원

화학부 무기화학

황 재 호

황재호의 박사학위논문을 인준함

2021년 2월

위 원 장 :

김성근

(인)

부 위 원 장 :

남좌민

(인)

위 원 :

이윤환

(인)

위 원 :

민갈희

(인)

위 원 :

박준원

(인)



## **Abstract**

# **Synthesis of Plasmon-Enhanced Fluorescence-Active Nanostructures And Their Applications**

Jae-Ho Hwang

Department of Chemistry

The Graduate School

Seoul National University

Plasmon-enhanced fluorescence (PEF) refers to a phenomenon in which the optical signal of a fluorescent emitter located in the vicinity of a plasmonic nanostructure is amplified. In general, since plasmonic nanostructures react to external light in the form of elastic scattering, their own fluorescence emission level is low. However, localized surface plasmon resonance (LSPR) provides an environment in which the signal of a fluorescent emitter can be amplified by highly concentrated electromagnetic fields around plasmonic nanostructures. PEF was first discovered in the early 1980s, and factors that determine the signal amplification efficiency of fluorescent emitters have been identified during the decades of research. In recent years, it is attracting great attention by showing a fluorescence signal amplification effect of up to 1,000,000 times. This thesis contains the research contents of the fabrication and application of highly efficient PEF-active nanostructures. highly efficient PEF-active nanostructure

In Chapter 1, background information on plasmon-enhanced fluorescence is described, which is helpful in understanding the research conducted in Chapter 2 and 3. Specifically, the theoretical background of PEF, a major factor determining the enhancement efficiency of an optical signal, examples of PEF-active nanostructures, and applications of PEF are summarized.

In Chapter 2, core-shell nanocuboids that emits a strong and quantitative PEF signal were synthesized and applied to microarray-based miRNA detection.

In Chapter 3, the research contents of high yield synthetic strategy for Ag-based multilayer nanostructures with remarkable PEF activity in a broad wavelength range were described.

The research contents in Chapter 2 and Chapter 3 were conducted with the ultimate goal of the practical application of PEF phenomenon. In order for the fabricated PEF-active nanostructures to be practically utilized, the synthesized outputs have to generate uniform and stable signal. Also, in addition to simply confirming whether a fluorescent signal is amplified, it is necessary to prove whether there are comparative advantages over the conventional fluorescent materials in practical application fields. The microarray-based miRNA detection results in Chapter 2 can be said to have important significance as an example of directly demonstrating the superiority of performance through comparison with the existing fluorescent emitter under the same conditions.

**Keywords : plasmon-enhanced fluorescence, plasmonic nanostructure, bioapplication, miRNA detection, optical signal enhancement**

**Student Number : 2009-20319**

# Contents

<b>Abstract.....</b>	<b>i</b>
<b>Contents.....</b>	<b>vi</b>
<b>List of Figures.....</b>	<b>vii</b>
<b>Chapter 1. Introduction.....</b>	<b>1</b>
1.1. Plasmon-enhanced fluorescence.....	2
1.2. Fluorescence and Plasmon-enhanced fluorescence.....	4
1.3. Main points to consider in PEF.....	6
1.4. Types of PEF-active nanostructures.....	10
1.5. Applications of PEF.....	15
1.6. Challenges toward practical applications of PEF.....	21
1.7. Conclusions.....	23
1.8. References.....	24
<b>Chapter 2. DNA-Engineerable Ultraflat-Faceted Core-Shell Nanocuboids with Strong, Quantitative Plasmon-Enhanced Fluorescence Signals for Sensitive, Reliable MiroRNA Detection.....</b>	<b>44</b>
2.1. Introduction.....	45
2.2. Experimental Section.....	47
2.3. Results and Discussion.....	57

2.4. Conclusions.....	65
2.5. References.....	66
<b>Chapter 3. High Yield Synthesis of Multilayered Alternative Nanoplasmonic-Nanodielectric Amplifiers (MANNAs) for Broad Wavelength Range Plasmon-Enhanced Fluorescence.....</b>	<b>88</b>
3.1. Introduction.....	89
3.2. Experimental Section.....	91
3.3. Results and Discussion.....	94
3.4. Conclusions.....	98
3.5. References.....	99
<b>국문초록.....</b>	<b>108</b>

# List of Figures

## Chapter 1

- Figure 1.1.** Fundamentals of optical processes described with a Jablonski diagram ..... 31
- Figure 1.2.** Distance dependency of PEF activation process ..... 32
- Figure 1.3.** Effect of plasmonic peak wavelength and fluorescence excitation, emission wavelengths on PEF ..... 33
- Figure 1.4.** Au bowtie substrate-based single NIR fluorophore detection experiment ..... 34
- Figure 1.5.** Single-molecule PEF on Ag monomer and dimer particle ..... 35
- Figure 1.6.** PEF from single fluorophores end-linked to Au nanorods ..... 36
- Figure 1.7.** Au-based PEF-active nanostructures reported in N. J. Halas group ..... 37
- Figure 1.8.** Shell-isolated Ag nanoparticle/tip for PEF ..... 38
- Figure 1.9.** Spherical Au nanoparticle dimer PEF experiment using DNA origami technique ..... 39

**Figure 1.10.** PEF at plasmonic cavity between colloidal nanoparticle on 2D plasmonic film ..... 40

**Figure 1.11.** Representative research cases related to PEF biosensors ..... 41

**Figure 1.12.** Spatiotemporal delivery of QDs into a single living HeLa cell using SnO<sub>2</sub> nanowire endoscope ..... 42

## Chapter 2

**Figure 2.1.** Schematic illustration of synthetic pathway for fluorescence-amplified nanocuboid (FANC) and fluorescent silica shell-coated FANC (FS-FANC) for maximized plasmon-enhanced fluorescence (PEF) ..... 71

**Figure 2.2.** TEM image, dimensions and optical properties of the synthesized AuNRs ..... 72

**Figure 2.3.** Quantification of the number of Alexa 647<sup>TM</sup> oligonucleotides on AuNR surface ..... 73

**Figure 2.4.** Quantification of incorporated Alexa Fluor<sup>TM</sup> 647 fluorophores in the silica shell of FS-NC ..... 74

**Figure 2.5.** Characterization of FANCs ..... 75

<b>Figure 2.6.</b> Fluorescent oligonucleotide design for FANCs .....	76
<b>Figure 2.7.</b> TEM image, dimensions and optical properties of the synthesized AuNRs .....	77
<b>Figure 2.8.</b> Fluorescence measurements of FANCs .....	78
<b>Figure 2.9.</b> Theoretical modeling of FANCs .....	79
<b>Figure 2.10.</b> Formation of FS-FANC and fluorescence measurement .....	80
<b>Figure 2.11.</b> TEM images of FS-FANCs (a) and FS-NCs (b) .....	81
<b>Figure 2.12.</b> Schematic illustration of microarray-based miRNA detection using FS-FANCs .....	82
<b>Figure 2.13.</b> Microarray-based miRNA detection results using FS-FANCs .....	83
<b>Figure 2.14.</b> The long term stability of fluorescence signal of microarray spot.....	84
<b>Figure 2.15.</b> Microarray-based miRNA assay with FANCs .....	85
<b>Figure 2.16.</b> Microarray-based miRNA assay results with conventional fluorescence labels.....	86

**Figure 2.17.** Representative AFM images and the averaged area values at each concentrations..... 87

### **Chapter 3**

**Figure 3.1.** Schematic illustration of synthetic process of multilayered alternative nanoplasmonic-nanodielectric amplifiers (MANNAs) for broad wavelength range plasmon-enhanced fluorescence ..... 101

**Figure 3.2.** Synthesis of Ag-SiO<sub>2</sub> fluorescent nanoparticles ..... 102

**Figure 3.3.** A strategy for securing high dispersity in the process of forming silica shell step ..... 103

**Figure 3.4.** Characterization of Ag-SiO<sub>2</sub>-Ag MANNA ..... 104

**Figure 3.5.** Selection of broad wavelength range fluorophores ..... 105

**Figure 3.6.** Fluorescence measurements of MANNAs with four different types of fluorophores ..... 106

**Figure 3.7.** Simulation analysis of MANNA's fluorescence signal amplification ..... 107

# **Chapter 1**

## **Introduction**

## 1.1. Plasmon-enhanced fluorescence

When the plasmonic nanomaterial is irradiated with light source, the electromagnetic wave and free electron cloud at the plasmonic surface undergo collective oscillations called as resonance effect, and in the process, the density of the electromagnetic wave is greatly amplified.<sup>1,2</sup> Surface plasmon resonance (SPR) refers to the phenomenon of local energy excitation of plasmon on a flat plasmonic surface caused by collective oscillation of plasmonic material and electromagnetic waves. In particular, when this extremely concentrated electromagnetic field density occurs in a structure in a confined region in the nanometer range, it is called localized plasmon resonance (LSPR).<sup>3</sup> The research field, which utilizes SPR and LSPR as a tool for optical signal enhancement is called plasmon-enhanced spectroscopy and plasmon-enhanced fluorescence (PEF) is a major subject of plasmon-enhanced spectroscopy.

PEF is the phenomenon of obtaining improved luminescence performance when a fluorescent emitter is near the plasmon surface. PEF was first discovered in the early 1980s,<sup>4-7</sup> and theoretical and experimental research on PEF has been going on for decades.<sup>2,8-13</sup> Metal-enhanced fluorescence (MEF)<sup>9,14</sup> and surface-enhanced fluorescence (SEF)<sup>7,15</sup> are also widely used terminologies for PEF.<sup>11</sup> In general, plasmonic nanostructures do not induce high photoluminescence activity because they generate optical signals mainly in the form of elastic scattering.<sup>16</sup> Instead, localized surface plasmon resonance (LSPR) around the plasmonic nanostructures provides a highly enhanced electric field that can induce specific situations for the fluorescent emitter to experience signal amplification. The type of fluorescent emitter most commonly used in PEF is an organic fluorophore, and various kinds of quantum emitters such as quantum dots (QDs),<sup>17-21</sup> metal nanoclusters,<sup>22,23</sup> carbon dots (CDs),<sup>24-26</sup> upconversion nanoparticles,<sup>27,28</sup> and perovskites<sup>29-31</sup> are also being studied in PEF research. PEF not only provides improved emissions and reduced lifetimes, but also allows for an expansion of the fluorescence field by incorporating weak quantum emitters with plasmonic nanoplatform

design, simultaneously preventing photobleaching and offering imaging opportunities with a resolution much better than the diffraction limit.<sup>11</sup> It also combines plasmonic nanostructures with quantum emitters, opening a window for a new kind of optical probe. The state-of-the-art developments related to PEF are based on the delicate and smart coupling of excited fluorescent emitters and localized surface plasmon in nanostructures, where local field amplification leads to enhanced brightness and sensitivity of quantum emission.<sup>2,8,10,13,32</sup>

## 1.2. Fluorescence and Plasmon-enhanced fluorescence

The phenomenon in which energy is released in the form of light is called luminescence. The light emission is divided into fluorescence and phosphorescence according to the characteristics of the excited state.<sup>16</sup> The path of the electron in fluorescence process can be described by the Jablonski diagram (Figure 1.1).<sup>17</sup> The electrons in the ground state  $S_0$  (singlet spin state) are lifted to excited states ( $S_n$ ) when excited by external electromagnetic field radiation. The excited electrons release energy as they relax to lower energy level states, and at this time, energy is released in the form of light, which is called a radiative decay. The energy emitted in the form of light in a radiative decay is a fluorescent signal, and by radiative decay, the electrons return to their original ground state ( $S_0$ ). On the other hand, thermal energy can also be released to the surroundings by vibration or rotational relaxation of the excited electrons, which is called non-radiative decay. In the case of fluorescence, the transition of electrons occurs in a “spin-allowed” conversions, so the entire luminescence process takes a relatively short time comparing with phosphorescence. Contrastively, the so-called intersystem crossing takes place in phosphorescence. In intersystem crossing process, the excited electrons move to the excited triplet state and the phosphorescent signal is acquired by relaxation from the excited triplet state to the ground singlet state. As a result, phosphorescence produces luminescence signal by a “spin-forbidden” conversions, so re-emission of light by phosphorescence takes a longer time compared to re-emission of fluorescence.

The two most important factors determining the efficiency of fluorescence are quantum yield ( $Q_0$ ) and lifetime ( $\tau$ ). Both factors can be described by the radiative decay rate ( $k_r$ ) and non-radiative decay rate ( $k_{nr}$ ). The non-radiative decay rate is the sum of all kinds of decay rates for all non-radiative relaxation pathways leading to the electronic ground state ( $S_0$ ). The quantum yield is an index representing the proportion of light that corresponds to fluorescence among all the light emitted by a fluorescent emitter, and can be described as

$$Q_0 = k_r / (k_r + k_{nr}).$$

And the lifetime is defined as the average time an electron stays excited before it relaxes to an electronic ground state, and can be expressed as

$$\tau = 1 / (k_r + k_{nr}).$$

In general, fluorescent emitters with higher quantum yields and shorter lifetimes show better fluorescence efficiency. The fluorescence signal is proportional to the product  $P_0 \epsilon Q$ , except for the effect on the light collection efficiency of the optical measurement system, where  $P_0$  is the excitation power (photons  $s^{-1}$ ),  $\epsilon$  is the molar extinction coefficient ( $M^{-1} cm^{-1}$ ) of the emitter, and  $Q$  is the emission quantum yield of the emitter.

In situations where the fluorescent emitter is within the influence of the PEF, it interacts with the dense EM field formed by LSPR on the plasmonic surface. The fluorescent emitter is placed under an EM field amplified by the plasmonic surface and it can be expressed as  $|E| = (|E_{PEF}|) / (|E_0|)$ , where  $|E_{PEF}|$  is the local electromagnetic field intensity in the region that PEF occurs,  $|E_0|$  is the incident electromagnetic field intensity generated by the excitation source. On the other hand, the rate at which excited electrons are released also undergoes a change, which in turn affects the fluorescence efficiency of the fluorescent emitter. So the quantum yield of the PEF system is changed as ( $Q_{PEF}$ ). As a result, the enhanced fluorescence signal intensity of the PEF is proportional to the product  $[ \langle |E|^2 \rangle \cdot P_0 ] \epsilon Q_{PEF}$ .

### **1.3. Main points to consider in PEF**

#### **Distance between the fluorescent emitters and plasmonic nanosurface**

As the surface distance from the fluorescent emitter to the plasmon increases, a gradual transition from fluorescence quenching to fluorescence enhancement is observed until the optimal distance is reached where the nanostructure has a negligible effect on fluorescence phenomenon.<sup>33</sup> Depending on where the fluorescent emitter is placed, there is a competition between the coupling of the fluorescent emitter with the LSPR and the non-radiative energy transfer. The former is preferred over short distances to promote fluorescence enhancement, and the latter increases exponentially in direct or nearly direct contact resulting in a sharp decrease in quantum yield. For these reasons, fluorescent emitters are usually separated from the plasmon surface using various types of spacers to avoid direct contact or nearly direct contact in PEF studies. In the case of SERS, it is widely known that the enhancement factor is proportional to the fourth power of the local field ( $|E|^4$ ) because Raman radiation itself couples to LSPRs.<sup>34</sup> However, for PEF, the signal amplification process includes only the incident EM field, so that the PEF enhancement factor is proportional to the second power of the local field ( $|E|^2$ ).<sup>35</sup> Consequently, observing PEF phenomena experimentally is usually more difficult than observing SERS. This is because the enhancement factors are several orders magnitude lower than those of SERS.

Therefore, PEF researchers have focused on placing fluorescent emitters in the proper locations in the PEF-active system. Repeatedly, the fluorescent emitters of PEF systems are always in competition between the quenching process by energy transfer and the amplification process by enhanced EM field around plasmonic surface. This is the reason why the distance between the fluorescent emitters and the plasmonic surface must be finely adjusted. One of the most representative attempts to elucidate the fluorescent emitter-plasmon surface distance-dependence of PEF was found in a paper published by the by Lukas Novotny group in 2006

(Figure 1.2).<sup>36</sup> The authors measured the PEF activity of a single fluorescent emitter as a function of distance to a single Au nanoparticle and a single fluorescent emitter. The fluorescent emitter samples were spin-coated onto a glass coverslip at a concentration low enough so that only single molecules were observed in the focal radius of the observation device. After that, a polymer layer was introduced to measure the distance between the fluorescent molecules and Au nanoparticles, and the thickness of various polymers was pre-calibrated using AFM measurement. The fluorescence was measured when Au nanoparticle attached to the end of the optical fiber contacted the polymer layer, and the thickness of the pre-calibrated polymer was used as the distance ( $z$ ) between a single Au nanoparticle and a single fluorescent molecule. With this experimental setup, the emission rate was recorded as a function of the distance of a single Au nanoparticle to a single fluorescent emitter, and it was found that the maximum PEF activity appeared when the fluorescent emitter was  $\sim 5$  nm away from the plasmonic surface.

### **Excitation and emission of fluorescent emitters and resonance wavelengths of plasmonic nanostructure**

Another important factor in determining PEF performance other than distance is also the plasmonic resonance wavelength of the plasmonic nanostructure. The plasmon wavelengths of plasmonic nanostructures varies from ultraviolet to near-infrared spectral regions, depending on factors such as the types of plasmon substances, size, geometry, and composition of nanostructures.<sup>2,37</sup> Many researchers have sought to clarify the relationship between the plasmon resonance wavelength of plasmonic nanostructures and the absorption and emission wavelengths of fluorescent emitters that influence the activity of PEF. As one important example of such an effort, David S. Ginger's group measured molecular fluorescence on a single Ag nanoprism with different plasmon resonance wavelengths (Figure 1.3).<sup>38</sup> Specifically,

each of the Ag nanoprisms with various plasmon resonance wavelengths were spread out on a glass cover slip, and individual spectral information was obtained using single particle dark field spectroscopy. The fluorescent emitters were placed at a fixed distance from a single Ag nanoprism using double-stranded DNA as a spacer system. They found a strong correlation between the fluorescence activity of the emitter and the plasmon resonance of the single Ag nanoprism. The location of the plasmon peak in between the fluorophore's excitation and emission peaks provided an optimized circumstance for obtaining the largest intensity enhancement. It is widely accepted that for PEF optimization, fluorescent emitters must be located in regions with a high EM field density corresponding to the absorption and emission wavelengths of the emitter.

### **Hot spots for PEF**

In most PEF-active systems, the average EF typically ranges from ten to hundreds fold.<sup>11</sup> However, there are situations in which higher levels of signal amplification are limitedly possible. In some specific cases, some nanostructures can provide ultra--high local EM field sites and EFs can be achieved up to  $\sim 10^6$ -fold.<sup>39,40</sup> In general, the limited regions that provide such ultrahigh local electric fields are called a hot spots.<sup>41-44</sup> Typically, the hot spot of PEF is expressed through the few nanometer-sized nanogap regions generated in dimer or other multimeric nanostructures.<sup>45</sup> W. E. Moerner group succeeded in amplifying the fluorescence signal of the fluorescent emitter exciting at 780 nm by about 1350 times using Au bowtie dimeric nanostructure (Figure 1.4).<sup>46</sup> The authors explained that an EF of  $\sim 1340$  was obtained through the product of the increase in quantum efficiency ( $\sim 9$ ) and the increased in field enhancement ( $\sim 181$ ). For another example of hot spot for PEF, Le Ru group in 2011 reported an improvement in fluorescence emitted from fluorophore-labeled DNA using Ag nanoparticle aggregates at 532 nm excitation wavelength and EF value was  $\sim 740$ .<sup>45</sup> And S. Y. Chou group achieved a remarkable level of PEF EF of  $4 \times 10^6$ -fold through a three-dimensional plasmonic

nanoantenna dot array platform [Disk-coupled dots-on-pillar antenna array (D2PA)] with excitation at 785 nm.<sup>39</sup> The  $4 \times 10^6$ -fold is the highest value among the EF obtained through PEF study. They used SiO<sub>2</sub> spacer around the Au nanodots and optimized the thickness of the spacer to provide a large average fluorescence integrated enhancement.

However, most of these hyper-enhancement situations have been found in single-molecule measurements or specific “hot spot” regions that cannot be easily obtained or reproduced. Although experimentally high amplification of fluorescent signals can be achieved, the aspect that it is difficult to stably reproduce signals is a situation that slows down practical application of PEF through hot spot generation.

## 1.4. Types of PEF-active nanostructures

In the decades leading up to the present day, numerous different nanostructures have been used in the PEF research. In the early days of PEF studies, simple Au or Ag-based nanospheres or nanofilms were frequently utilized. For Au, inter-band transitions below the 600 nm wavelength region ( $\lambda < 600$  nm) severely reduce the fluorescent signals, so that the nanostructures that can have plasmon resonance wavelengths over 600 nm are preferred.<sup>47</sup> For the same reason, fluorescent emitters, which have excitation and emission wavelengths over 600 nm are also preferred. Since the optical properties of plasmon nanoparticles are sensitively dependent on their type, size and shape of plasmonic materials, it is important to develop a reliable high yield synthetic approach capable of producing a variety of plasmon nanostructures suitable for various fluorescent emitters used. There have been many attempts to advance PEF, and it can be largely divided into 2-dimensional plasmon nanostructures and colloidal nanoparticles from a structural aspect.

### 2D plasmonic nanostructures

2D nanoplatforms such as roughened surface or colloid-coated substrates have been frequently utilized in PEF research.<sup>47-49</sup> In these platforms, plasmonic islands or colloidal nanoparticles are randomly formed on the 2D plasmonic substrates,<sup>50,51</sup> and the roughened plasmonic structures produced in these way provide a certain level of electromagnetic field amplification environment throughout the surface. Generally, fluorescent emitters are sprayed onto the rough plasmonic substrate, and the concentration is corrected to measure the increase in fluorescence signal.<sup>52</sup> Alternatively, the PEF phenomenon is induced with a platform in which nanoparticles or nanoholes are periodically formed on the 2D plasmonic substrate.<sup>39</sup> In these 2D periodic plasmonic nanostructures, nanoparticles or periodic plasmonic patterns can be precisely constructed and adjusted with delicate distance control.<sup>[53][54]</sup> These features can be used to

systematically study the subtle changes in distance or dimensions and the periodicity of metal substrate patterns on PEF performance.

### **Colloidal nanoparticles**

The most widely used nanostructure for PEF is colloidal nanoparticles. All available structures, such as nanospheres,<sup>55,56</sup> nanocubes,<sup>57,58</sup> nanostars,<sup>59,60</sup> nanoprisms<sup>61,62</sup> were utilized for PEF study. Moreover, small aggregates and finely assembled nanostructures (eg. dimers and trimers) in PEF have been extensively explored because these types of nanostructures have particle-particle junction regions with hot spots for optical signal amplification. When plasmon nanoparticles are used for PEF studies, dielectric spacers or ligands are usually placed between the fluorescent emitters and the plasmon surface to carefully adjust the fluorescent emitter separation from the plasmon surface and avoid direct contact between them. In this regard, core-shell nanostructures including dielectric compositions for PEF have been intensively studied over the past 10 years.<sup>63-67</sup> Dielectric media such as silica or polymer are not only good spacers between the fluorescent emitter and the plasmonic surface, but also a stable supporter for the fluorescent emitter.<sup>68,69</sup> In other words, the fluorescent emitters can be stably held in the PEF-active region with a fixed position in the dielectric composition of the core-shell nanostructures, preventing fatal reduction of the fluorescence signal due to direct or nearly direct contact.

In 2007, J. R. Lakowicz group reported PEF control of Cy5 dye on Ag particle monomer and dimer system (Figure 1.5).<sup>70</sup> The Ag dimers were formed by hybridization with double-length single-stranded oligonucleotides, and the oligonucleotides contained a Cy5 fluorophore. The single fluorophore-level image analysis showed that single molecule fluorescence improved 7-fold in Ag monomer and 13-fold in Ag dimer compared to the free Cy5-modified oligonucleotides in the absence of Ag surface. The same group also published

single fluorophore image-based PEF research in 2010 (Figure 1.6).<sup>71</sup> The authors observed approximately 40-fold fluorescence enhancement of single Cy5 fluorophore which was end-linked to Au nanorods. The biotin-streptavidin chemistry was utilized for end-linking of Cy5 fluorophores on Au nanorods and single fluorophore events were revealed by time-tracking measurements of one-step photobleaching. The authors demonstrated that fluorescence enhancement of nanorod end-linked fluorophore was due to a combination of processes including local electric field concentration around the nanorods, alteration of the radiative decay rate. N. J. Halas group have reported the invention of several structures of Au-based PEF-active nanostructures (Figure 1.7).<sup>72,73</sup> They conducted studies of PEF through nanostructures Au nanoshells, Au nanorods, and Au nanomatryoshkas. Using the Au nanoshells and Au nanorods, they succeeded in improving the signals of the HAS-IR800 NIR fluorophore by 40 and 9 times, respectively. On the other hand, in the PEF study of Au nanomatryoshka structure, the theoretical basis for fluorescence amplification was provided through simulation without specifying specific fluorescence enhancement factor. In 2010, ultra-thin dielectric shell-coated plasmonic nanosurface research on SERS was published under the name of “shell-isolated nanoparticle-enhanced Raman spectroscopy (SHINERS)” by Z. Q. Tian group.<sup>74</sup> Since then, shell-isolated nanoparticles that induce signal enhancement while preventing direct contact of the signal material to the plasmonic surface through an ultra-thin dielectric layer formed with a compact density have been applied to PEF (Figure 1.8).<sup>75</sup> The shell-isolated Ag nanoparticle/tip called “shell-isolated nanoparticle enhanced fluorescence (SHINEF)” exhibited high stability and long-term PEF performance (~1000 fold enhancement). Meanwhile, in one interesting study, DNA origami was introduced as a tool to create hot spots for PEF activation (Figure 1.9).<sup>76</sup> DNA origami is a molecular self-assembly technique for fabricating ultrafine nanomaterials using oligonucleotide hybridization reaction.<sup>77,78</sup> P. Tinnefeld and coworkers used DNA origami to precisely control the nanogaps between

spherical Au nanoparticle dimers that act as PEF hot spots. The PEF signal was generated by placing two Au nanoparticles and a fluorescent emitter in a designated space of a 220 nm pillar-shaped DNA origami, and the degree of increase of the fluorescent signal according to the length of the nanogaps could be scanned by precisely controlling the design of the origami. Conclusively, they were able to achieve a maximum fluorescence signal amplification of ~100 under such a sophisticated system.

### **Colloidal nanoparticles on 2D film**

There are also research cases in which fluorescence amplification is achieved by hybridizing colloidal nanoparticles and 2D planar nanoplatforms. The key to this type of PEF-active nanostructure is to form a hot spot between the colloidal nanoparticle and the 2D nanostructure and place a fluorescent emitter at that location. Usually the area where the fluorescent emitter is placed is protected from quenching with a dielectric layer. Camposeo et al. developed NIR-PEF substrates based on micropatterned Au nanocages with a precise spatial control.<sup>79</sup> In their PEF nanoplatform, there are three different layers on 2D quartz substrate. At first Au nanocages are immobilized on the regions covered by APTES and SiO<sub>2</sub> layer, which acts as a spacer for delicate PEF control, is doped on top of it. And finally, an emissive layer composed of LD 700 fluorophore is placed over the SiO<sub>2</sub> spacer layer. In their work, the dependence of fluorescence enhancement on the distance between the nanocage layer and the emissive layer has been explored experimentally by finely tuning SiO<sub>2</sub> layer, and its theoretical validity has been demonstrated through simulation. Conclusively, when the distance at 80 nm, maximal fluorescence EF of 2.2-fold was confirmed in their Au nanocage-based PEF substrate. In similar approach, the M. Lin group conducted PEF studies on upconversion nanoparticle signal enhancement. In their layer by layer PEF substrate contains AuNRs-polyelectrolytes-upconversion nanoparticles trilayer structures.<sup>27</sup> The polyelectrolytes spacer layer is composed

of positively charged poly allylamine hydrochloride (PAH) and negatively charged sodium polystyrene sulfonate (PSS) and utilized as a fine-controller of PEF activity through thickness alteration. In conclusion, a maximum fluorescence EF of 22.6-fold was obtained when the thickness of spacer layer was 8 nm. Among the PEF studies in which colloidal particles and 2d planar plasmonic surfaces were combined, the most meaningful results were published by M. H. Mikkelsen group<sup>80,81</sup> and X. Liu group.<sup>82</sup> They commonly formed a plasmonic cavity between the Au film and the Ag nanocube and inserted a fluorescent emitter in the space. At first in 2015, Akselrod et al. used Ru dye as a fluorescent emitter embedded in spacer polymer layer and obtained ~80-fold fluorescence enhancement factor by scanning of the thickness of the spacer layer (Figure 1.10).<sup>80</sup> The most notable thing in this study is that the angle-resolved single particle fluorescence measurement technique was used. Using this technology, researchers were able to separate and obtain the fluorescence signal according to the detecting angle, which made it possible to consider the emission collection efficiency and the orientation of the fluorescence dipole, which cannot be performed in normal PEF studies. Through this specific approach to emission collection efficiency and fluorescence dipole orientation, they were able to achieve a close match between the experimental EF and the calculated EF. In 2015, CdSe/ZnS core-shell QD was introduced into the plasmonic cavity of the same PEF system.<sup>81</sup> They showed an increase in the spontaneous emission rate of a factor of 880 and simultaneously a 2,300-fold enhancement in the total fluorescence intensity of the QD. Meanwhile, X. Lu group introduced upconversion nanoparticles into the plasmonic cavity between Au film and Ag nanocube.<sup>82</sup> In particular, in this experiment, the fluorescent emitter independently formed a monolayer without spacer of the dielectric layer. Through precise control over the nanoparticle's local density of state, they could observe massive fluorescence EF up to four to five orders of magnitude.

## **1.5. Applications of PEF**

Fluorescence is actively and widely used in real life and academic research these days.<sup>83-88</sup> Ideally, PEF has high potential to replace conventional fluorescent emitters with better performance and higher functionality in all applications where fluorescence is currently utilized.<sup>12,13</sup> The amplified fluorescence signals can be obtained through the optimized PEF-active nanostructures. Furthermore, by taking full advantage of the unique properties of the nanoparticles, additional application-specific features such as high photostability,<sup>21</sup> multimodal imaging,<sup>89,90</sup> specific targeting,<sup>91,92</sup> and drug delivery<sup>92,93</sup> can be also obtained. Among the many applications of PEF research area, the two most reported fields, biosensors and single molecule detection, are further described below.

### **Biosensors**

The most active field of research for PEF's practical application is biosensors. Fluorescence in biosensors offers significant advantages over other methods. Fluorescent emitters effectively convert biological events into strong fluorescence signals that can be easily detected with optical detectors. The signal conversion processes induced by the fluorescence phenomenon are sensitive, fast, simple, and specific. And all these functions are essential features of biosensors. In addition to the strong fluorescence properties inherent in the field of biosensors, the optimized PEF-activated nanostructures provide higher sensitivity and photostability to biosensing systems. Moreover, the strong fluorescence signals of PEF help simplify system design by reducing the extra signal enhancement steps that are often used in biosensor setups. Furthermore, by providing additional functions in the processes of nanoparticle synthesis and ligand adhesion, PEF-active nanostructure can contribute to improving sensor selectivity and multi-sensing capabilities. For this reason, PEF has been used extensively in biosensor applications.

Representative research cases related to biosensors using PEF are summarized in Figure 1.11. The biosensors using PEF can be structurally divided into two types: a 2d planar surface and a colloidal nanoparticle system. Many types of sensing strategies for various biomolecules such as RNA, miRNA, DNA, virus antigen, etc. have been developed using these PEF biosensing platforms. One of the most widely used methods for PEF biosensor development is the deposition of pre-synthesized plasmonic nanoparticles on the surface of a planar substrate. The most important consideration in biosensing technology using a 2d planar surface is to control the distance between the fluorescent emitter and the plasmonic surface so that the beam signal does not disappear during the detection of the biomolecule. To this end, a dielectric layer is introduced between the fluorescence emitter and the plasmonic surface, or recognition molecules used for biomolecule detection naturally control the fluorescence signal reduction. As a representative example, L. Tang and coworkers developed an AuNR array biochip for target DNA detection (Figure 1.11a).<sup>94</sup> In the AuNR assembly ordered in an array standing perpendicular to the glass substrate, the electromagnetic field density between adjacent nanoparticles was dramatically enhanced compared to an ensemble of random AuNRs. Before the target DNAs are introduced, the fluorophores are closely adhered to the upper surface of the AuNR array biochip through molecular beacons, and the fluorescent signal is quenched. In this situation, the target DNA induces the unfolding of the molecular beacon, and the fluorophores are moved from the quenching region to the PEF range, thereby emitting a fluorescence signal.

It is important to develop colloidal PEF biosensors because most of the biological phenomena occur in nanometer-length scale. In the application process of a biosensor based on a colloidal nanoparticle system, the steps of fabrication of PEF-active nanostructures, attachment of functional materials, biomolecule recognition, and signal measurement are sequentially performed. Strategies for stably maintaining the fluorescence signal is essential in

the biosensor application field using colloidal nanoparticle systems, but there are also cases where the quenching of fluorescence light in the bio-recognition step is used as a detecting signal.

In certain cases, conformational flexibility of PEF-active nanostructure is useful for meeting the biosensing application requirements because PEF performance can be sensitively changed by external stimuli at biosensing environments such as temperature, light and pH.<sup>95,96</sup> A simple example for stimuli-responsive PEF biosensor has been carried out by L. Li group (Figure 1.11b).<sup>97</sup> They used hybrid nanoparticle with a Ag core and cross-linked poly(3-acrylamidephenylboronic acid-co-acryl acid, PAPBA-PAA) shell. The PAPBA-PAA shell region of the fabricated hybrid nanoparticles showed expansion and contraction behavior in response to changes in glucose concentration and pH, and accordingly, the fluorescence activity of Por<sup>4+</sup> molecules doped on the shell surface was changed, and functioned as a sensor. Meanwhile, the aggregation of plasmonic nanoparticles also functions as a major strategy for biosensing because aggregation process lead to the formation of hot spots, which in turn enhances the excitation rate of the fluorophore. The aggregation of plasmonic nanoparticles can be induced primarily through physical or chemical interactions triggered by the target analyte, and this process results in a rapid change in the fluorescence signal, which functions as a detection signal for that target substance. Zhu et al. suggested aggregation-induced biosensor using oligonucleotides as a trigger for aggregation of plasmon nanoparticles (Figure 1.11c).<sup>98</sup> In this approach, various types of plasmon nanoparticles, such as Au nanospheres, AuNRs or Au-Ag core-shell nanospheres, are gathered to form aggregation-induced hot spot generation to detect target DNA. The trigger for aggregation in this biosensor is the target DNA, and the fluorescence signal of the Cy5 fluorophore attached to the nanoparticles functions as a detectable signal as it undergoes large signal amplification during the aggregation of the nanoparticles by the target DNA. In Q.-H. Xu group's work in 2018, cysteine molecules were

used to induce aggregation of Au-Ag core-shell nanoparticles functionalized with rhodamine B isothiocyanate (RITC) fluorophores, resulting in hot spot generation among bimetallic nanoparticles (Figure 1.11d).<sup>99</sup> The fluorescence signal of RITC, which has been quenched because of short distance from the Au-Ag core-shell nanoparticle surface, is activated by the formation of plasmon hot spots by aggregation, so the concentration of cysteine molecules can be determined in the biosensor system. Most of the biosensors related to the aggregation of plasmonic nanoparticles have the advantage of having a simple system in which signals are confirmed only by introduction of a target molecule, but also has the disadvantage that it is difficult to secure reproducibility and quantification due to the nature of the random aggregation process.

The detection of intracellular biomarkers is one of the ultimate goals of the development of colloidal biosensors for early disease diagnosis. Cui et al. invented the Au nanocube-SiO<sub>2</sub> core-shell nanoprobe for the detection of intracellular biomarkers (Figure 1.11c).<sup>100</sup> The fluorescence signal of 5-carboxyfluorescein disappeared in the presence of Cu<sup>2+</sup> ions, and the fluorescence signal could be restored when pyrophosphate was added through the process of formation of the pyrophosphate-Cu<sup>2+</sup> complex. In their experiment, single nucleotide polymorphism could be detected by the process of rolling circle amplification coupled with the ligase chain reaction. In K.-M. Ng group's work, two sets of plasmon nanoparticles, functionalized with the anti-megalin and anti-podocin, respectively, were introduced for the tissue imaging of megalin and podocin in the glomeruli and tubules.<sup>101</sup> Using this nanoprobe, they could perform versatile and sensitive in-vivo imaging with intense color and enhanced fluorescence.

An interesting study on single-cell endoscopy by combining nanowires and plasmon-coupling effects was published by P. Yang and coworkers (Figure 1.12).<sup>102</sup> It is especially important to realize biological events inside a single cell to identify when and where

chemical/biological events occur at the cellular level, and single cell endoscopy can function as a powerful tool to achieve that goal. The authors has developed a nanowire-based optical probe that can be used as a material for endoscopy with high spatial and temporal resolution while delivering intracellular cargo with high spatial and temporal resolution. The authors developed a versatile, biocompatible nanowire-based optical probe for intracellular cargo delivery with high spatiotemporal precision. The optical probe was made of SnO<sub>2</sub> nanowire and QDs were conjugated with photocleavable linkers. When QDs were delivered, SnO<sub>2</sub> nanowire acted as a stable vehicle, and after reaching the target space, the photocleavable linker was cleaved through UV-irradiation, and the QDs were separated from the nanowire. After delivery, the SnO<sub>2</sub> nanowire was utilized as a nanowaveguide to activate the fluorescence signal of QDs, allowing subcellular imaging.

### **Single molecule detection**

In the past decades, fluorescence-based single molecule detection technology has had a profound impact on the fields of chemical and biological research because meticulous mechanistic investigation of single molecule level behavior is important for clearly revealing and understanding chemical biological reactions. The PEF technology, which can impart functionality with signal amplification capability, is the most suitable material for use in single molecule detection research. As discussed in previous section, W. E. Moerner group reported single molecule detection strategy using Au bowtie nanoantennas fabricated on PMMA transparent substrate.<sup>46</sup> The authors manufactured Au bowtie nanoantenna pattern on PMMA substrate by electron-beam lithography and sprayed low concentration of NIR fluorophore TPQDI. At hot spots located in the Au bowtie nanoantenna gap region, the electric field enhancement was more than 100-fold and tracking of the single molecule fluorescence signal yielded up to 1340-fold enhancement factor. In the finite-difference time-domain calculation,

optical PEF enhancement occurred at the center of the Au bowtie nanogap, and it was shown that the fluorescent signal gradually decreased when approaching the triangular tip due to the large energy loss of the plasmonic surface. M. Orrit and coworkers reported a single molecule fluorescence enhancement up to 1100-fold with high time resolution enabled by femto-second interval measurements.<sup>103</sup> The authors tracked single molecule fluorescence signal of crystal violet (CV) diffusing around the Au nanorod coated on glass slide. As individual fluorophore explores the electric field profile near the plasmonic nanoparticle, the molecule occasionally diffuses to the most favorable position where the fluorescence enhancement occurs maximally. By monitoring the fluorophore's diffusion with a high enough time resolution, the highest amplification points can be determined quantitatively. Although this experiment is not about the development of nanostructures with permanently 1100-fold fluorescence amplification performance, it shows the possibility that a very large level of signal enhancement can occur when the fluorophores are properly positioned at the optimal position, even in a typical nanostructure such as Au nanorod. The X. Zhang group have used the technique of single molecule super-resolution optical fluorescence microscopy to explore two-dimensional imaging of the fluorescence enhancement profile of single molecule, and reported the first direct measurement of single hot spots as small as 15 nm with an accuracy down to 1.2 nm.<sup>104</sup> The maximum fluorescence EFs measured at the hot spots reached 54-fold for aluminum thin film and 136-fold for silver nanoparticle clusters.

## **1.6. Challenges toward practical applications of PEF**

PEF has the advantage of having a brighter light intensity than fluorescence and can be given additional functionality by utilizing the properties of nanoparticles. Therefore, theoretically, there is sufficient possibility that it can be replaced with better performance in the field where conventional fluorescent emitters are used. However, until now, it is very rare that PEF has been used by replacing fluorescent emitters in practical applications. Although there may be differences in detailed points to be solved according to specific application fields, the following are the common challenges that PEF-active nanostructures must have prior to practical application to replace fluorescent emitters. At first, PEF-active nanostructures with high EFs must be reproducibly synthesized with high-yield synthesis. The reproducibility can be said to be the most important part of any practical applications. For PEF plasmonic nanostructures that sensitively change the fluorescence signal according to the detailed location of the fluorescent emitter, it is most important to synthesize structures that stably emit uniform signals in high yield synthetic strategies. Second, the prepared PEF nanostructure should have universality for the application field. The emission wavelength used in the situation where the fluorescence phenomenon is applied is diverse. In addition, in order to impart specific functionality to the PEF-active nanostructures, various ligands or biomolecules are often required to be attached. Therefore, the higher the activity of the nanostructure over a wide range of light emission wavelengths and the higher the degree of freedom when imparting functionality, the closer it is to practical fluorescence applications. The third major challenge is securing stability. The stability discussed here ultimately means the stable expression of the fluorescent signal, which in many cases is related to the structural stability of the plasmonic nanostructure. Most of the PEF-active nanostructures are fabricated under clean and optimized synthetic conditions, but the environment in which they must reveal signals is not. The PEF-active nanostructure must maintain a stable even in harsh environments such as a solution with high ionic strength filled

with unknown biomolecules, a rapidly changing temperature, or a condition that is stored for a long time under dried state. For this, the plasmonic nanostructure containing a fluorescent emitter must have strong resistance to external stimuli, and the emitter's position within the nanostructure must be kept constant regardless of changes in the external environment. Finally, it must be clearly demonstrated that PEF performs better than fluorescence in applications where fluorescence is currently dominant. In most PEF studies, the fluorescence EF, which discusses the performance of PEF, is presented as a measure of how much PEF-active nanostructures amplify the fluorescence signal. However, in most cases, it has not been reported how advanced the conventional fluorescent emitters can achieve in practical application situations. From the end user's point of view, it is difficult to substitute the existing fluorescent emitters based on the high fluorescence EFs. Because it is said that nanostructures that effectively amplify fluorescent signals have been invented, and as mentioned in this paragraph, there are a number of obstacles that those materials must overcome before their actual applications. Therefore, rather than simply how much the fluorescence signal is amplified, revealing how much the result obtained from the fluorescence signal can be developed will ultimately become a more decisive basis for replacing the previously used fluorescence emitters with PEF-active nanostructures.

## 1.7. Conclusions

Synthesis of plasmonic nanostructures, especially Au and Ag, has undergone tremendous progress over the past decades. And plasmonic nanostructure-mediated fluorescence offers an advanced approach for nanoscale detection and imaging and is gaining attention as a major spectroscopic tool in biology and materials science. Interest in this field is expanding, especially in areas such as biosensor and single molecule detection, by achieving things that conventional fluorescent emitters cannot accomplish. Researchers at PEF have been deeply investigating the interactions between localized surface plasmon and nearby molecules, and the final goal will be to understand and control the communication between plasmonic nanomaterials and individual fluorescent emitters. The applications of PEF have increased rapidly during the last ten years, however, PEF has not yet successfully replaced the experiments performed by conventional fluorescent emitters. As discussed in the previous section, PEF-active nanostructures have challenges that need to be elucidated not only about the effect of signal amplification, but also versatility, stability, and performance comparison in practical applications. In addition, modeling and simulation of PEF mechanism, as well as standardization of various processes for substrate fabrication and data analysis in real and harsh media, must also be preceded. Although many challenges remain, PEF is expected to outperform conventional fluorescence in the long term, thanks to its excellent signal amplification capabilities and high ease of function mounting.

## 1.8. References

- [1] M. S. Tame, K. R. McEnery, Ş. K. Özdemir, J. Lee, S. A. Maier, M. S. Kim, *Nat. Phys.* **2013**, *9*, 329.
- [2] M. Ha, J. H. Kim, M. You, Q. Li, C. Fan, J. M. Nam, *Chem. Rev.* **2019**, *119*, 12208.
- [3] K. M. Mayer, J. H. Hafner, *Chem. Rev.* **2011**, *111*, 3828.
- [4] C. Y. Chen, I. Davoli, G. Ritchie, E. Burstein, *Surf. Sci.* **1980**, *101*, 363.
- [5] *Opt. Lett.* **1980**, *5*, 368.
- [6] D. A. Weitz, S. Garoff, C. D. Hanson, T. J. Gramila, J. I. Gersten, *J. Lumin.* **1981**, *24–25*, 83.
- [7] M. Moskovits, *Rev. Mod. Phys.* **1985**, *57*, 783.
- [8] J. Dong, Z. Zhang, H. Zheng, M. Sun, *Nanophotonics* **2015**, *4*, 472.
- [9] Y. Jeong, Y. M. Kook, K. Lee, W. G. Koh, *Biosens. Bioelectron.* **2018**, *111*, 102.
- [10] M. A. Badshah, N. Y. Koh, A. W. Zia, N. Abbas, Z. Zahra, M. W. Saleem, *Nanomaterials* **2020**, *10*, 1.
- [11] J.-F. Li, C.-Y. Li, R. F. Aroca, *Chem. Soc. Rev.* **2017**, *46*, 3962.
- [12] J. R. Lakowicz, K. Ray, M. Chowdhury, H. Szmecinski, Y. Fu, J. Zhang, K. Nowaczyk, *Analyst* **2008**, *133*, 1308.
- [13] T. Ming, H. Chen, R. Jiang, Q. Li, J. Wang, *J. Phys. Chem. Lett.* **2012**, *3*, 191.
- [14] C. D. Geddes, J. R. Lakowicz, *J. Fluoresc.* **2002**, *12*, 121.
- [15] E. Fort, S. Grésillon, *J. Phys. D. Appl. Phys.* **2008**, *41*, DOI 10.1088/0022-3727/41/1/013001.
- [16] C. Albrecht, *Anal. Bioanal. Chem.* **2008**, *390*, 1223.
- [17] M. Levitus, *Angew. Chemie Int. Ed.* **2011**, *50*, 9017.
- [18] A. G. Brolo, S. C. Kwok, M. D. Cooper, M. G. Moffitt, C.-W. Wang, R. Gordon, J. Riordon, K. L. Kavanagh, *J. Phys. Chem. B* **2006**, *110*, 8307.

- [19] C. Belacel, B. Habert, F. Bigourdan, F. Marquier, J.-P. Hugonin, S. Michaelis de Vasconcellos, X. Lafosse, L. Coolen, C. Schwob, C. Javaux, B. Dubertret, J.-J. Greffet, P. Senellart, A. Maitre, *Nano Lett.* **2013**, *13*, 1516.
- [20] Y. Jin, X. Gao, *Nat. Nanotechnol.* **2009**, *4*, 571.
- [21] B. Ji, E. Giovanelli, B. Habert, P. Spinicelli, M. Nasilowski, X. Xu, N. Lequeux, J.-P. Hugonin, F. Marquier, J.-J. Greffet, B. Dubertret, *Nat. Nanotechnol.* **2015**, *10*, 170.
- [22] X. Feng, T. Han, Y. Xiong, S. Wang, T. Dai, J. Chen, X. Zhang, G. Wang, *ACS Sensors* **2019**, *4*, 1633.
- [23] J.-M. Liu, J.-T. Chen, X.-P. Yan, *Anal. Chem.* **2013**, *85*, 3238.
- [24] C. Li, Y. Zhu, X. Zhang, X. Yang, C. Li, *RSC Adv.* **2012**, *2*, 1765.
- [25] R. Bukasov, Z. Kunushpayeva, A. Rapikov, S. Zhunussova, A. Sultangaziyev, O. Filchakova, *J. Fluoresc.* **2020**, *30*, 1477.
- [26] R. Bukasov, O. Filchakova, K. Gudun, M. Bouhrara, *J. Fluoresc.* **2018**, *28*, 1.
- [27] A. L. Feng, M. L. You, L. Tian, S. Singamaneni, M. Liu, Z. Duan, T. J. Lu, F. Xu, M. Lin, *Sci. Rep.* **2015**, *5*, 1.
- [28] J. Dong, W. Gao, Q. Han, Y. Wang, J. Qi, X. Yan, M. Sun, *Rev. Phys.* **2019**, *4*, 100026.
- [29] L. Xu, Y. Qiang, K. Xiao, Y. Zhang, J. Xie, C. Cui, P. Lin, P. Wang, X. Yu, F. Wu, D. Yang, *Appl. Phys. Lett.* **2017**, *110*, DOI 10.1063/1.4985294.
- [30] L. Gu, K. Wen, Q. Peng, W. Huang, J. Wang, *Small* **2020**, *16*, 2001861.
- [31] X. Wu, Y. Li, L. Wu, B. Fu, G. Liu, D. Zhang, J. Zhao, P. Chen, L. Liu, *RSC Adv.* **2017**, *7*, 35752.
- [32] M. T. Yarakı, Y. N. Tan, *Chem. - An Asian J.* **2020**, *15*, 3180.
- [33] A. I. Dragan, E. S. Bishop, J. R. Casas-Finet, R. J. Strouse, J. McGivney, M. A. Schenerman, C. D. Geddes, *Plasmonics* **2012**, *7*, 739.

- [34] E. C. Le Ru, P. G. B. T.-P. of S.-E. R. S. Etchegoin, Eds. , Elsevier, Amsterdam, **2009**, pp. xxi–xxiii.
- [35] R. A. Alvarez-Puebla, N. Pazos-Perez, L. Guerrini, *Appl. Mater. Today* **2018**, *13*, 1.
- [36] P. Anger, P. Bharadwaj, L. Novotny, *Phys. Rev. Lett.* **2006**, *96*, 3.
- [37] J. Olson, S. Dominguez-Medina, A. Hoggard, L. Y. Wang, W. S. Chang, S. Link, *Chem. Soc. Rev.* **2015**, *44*, 40.
- [38] Y. Chen, K. Munechika, D. S. Ginger, *Nano Lett.* **2007**, *7*, 690.
- [39] L. Zhou, F. Ding, H. Chen, W. Ding, W. Zhang, S. Y. Chou, *Anal. Chem.* **2012**, *84*, 4489.
- [40] W. Zhang, F. Ding, W.-D. Li, Y. Wang, J. Hu, S. Y. Chou, *Nanotechnology* **2012**, *23*, 225301.
- [41] D.-K. Lim, K.-S. Jeon, H. M. Kim, J.-M. Nam, Y. D. Suh, *Nat. Mater.* **2010**, *9*, 60.
- [42] D.-K. Lim, K.-S. Jeon, J.-H. Hwang, H. Kim, S. Kwon, Y. D. Suh, J.-M. Nam, *Nat. Nanotechnol.* **2011**, *6*, 452.
- [43] P. Gu, W. Zhang, G. Zhang, *Adv. Mater. Interfaces* **2018**, *5*, 1800648.
- [44] H. K. Lee, Y. H. Lee, C. S. L. Koh, G. C. Phan-Quang, X. Han, C. L. Lay, H. Y. F. Sim, Y. C. Kao, Q. An, X. Y. Ling, *Chem. Soc. Rev.* **2019**, *48*, 731.
- [45] R. Gill, E. C. Le Ru, *Phys. Chem. Chem. Phys.* **2011**, *13*, 16366.
- [46] A. Kinkhabwala, Z. Yu, S. Fan, Y. Avlasevich, K. Müllen, W. E. Moerner, *Nat. Photonics* **2009**, *3*, 654.
- [47] S. Kim, J. M. Kim, J. E. Park, J. M. Nam, *Adv. Mater.* **2018**, *30*, 1.
- [48] J. Kümmerlen, A. Leitner, H. Brunner, F. R. Aussenegg, A. Wokaun, *Mol. Phys.* **1993**, *80*, 1031.
- [49] K. Aslan, K. McDonald, M. J. R. Previte, Y. Zhang, C. D. Geddes, *Chem. Phys. Lett.* **2008**, *464*, 216.
- [50] L. V Stebounova, E. Guio, V. H. Grassian, *J. Nanoparticle Res.* **2011**, *13*, 233.

- [51] A. M. El Badawy, T. P. Luxton, R. G. Silva, K. G. Scheckel, M. T. Suidan, T. M. Tolaymat, *Environ. Sci. Technol.* **2010**, *44*, 1260.
- [52] T. Yamaguchi, T. Kaya, H. Takei, *Anal. Biochem.* **2007**, *364*, 171.
- [53] H. Li, J. Wang, F. Liu, Y. Song, R. Wang, *J. Colloid Interface Sci.* **2011**, *356*, 63.
- [54] B. Yang, N. Lu, D. Qi, R. Ma, Q. Wu, J. Hao, X. Liu, Y. Mu, V. Reboud, N. Kehagias, C. M. S. Torres, F. Y. C. Boey, X. Chen, L. Chi, *Small* **2010**, *6*, 1038.
- [55] Y. Sun, Y. Xia, *Science* **2002**, *298*, 2176.
- [56] M. Grzelczak, J. Pérez-Juste, P. Mulvaney, L. M. Liz-Marzán, *Chem. Soc. Rev.* **2008**, *37*, 1783.
- [57] M. Yi, D. Zhang, X. Wen, Q. Fu, P. Wang, Y. Lu, H. Ming, *Plasmonics* **2011**, *6*, 213.
- [58] D. W. Jung, J. M. Kim, H. J. Yun, G. R. Yi, J. Y. Cho, H. Jung, G. Lee, W. S. Chae, K. M. Nam, *RSC Adv.* **2019**, *9*, 29232.
- [59] I. G. Theodorou, P. Ruenraroengsak, D. A. Gonzalez-Carter, Q. Jiang, E. Yagüe, E. O. Aboagye, R. C. Coombes, A. E. Porter, M. P. Ryan, F. Xie, *Nanoscale* **2019**, *11*, 2079.
- [60] I. G. Theodorou, Z. A. R. Jawad, Q. Jiang, E. O. Aboagye, A. E. Porter, M. P. Ryan, F. Xie, *Chem. Mater.* **2017**, *29*, 6916.
- [61] Z. Buch, V. Kumar, H. Mangain, S. Chawla, *Chem. Commun.* **2013**, *49*, 9485.
- [62] Y. You, Q. Song, L. Wang, C. Niu, N. Na, J. Ouyang, *Nanoscale* **2016**, *8*, 18150.
- [63] O. G. Tovmachenko, C. Graf, D. J. van den Heuvel, A. van Blaaderen, H. C. Gerritsen, *Adv. Mater.* **2006**, *18*, 91.
- [64] D. Gontero, A. V. Veglia, A. G. Bracamonte, D. Boudreau, *RSC Adv.* **2017**, *7*, 10252.
- [65] J. Zhang, Y. Fu, F. Mahdavi, *J. Phys. Chem. C* **2012**, *116*, 24224.
- [66] S. Sun, I. L. Rasskazov, P. S. Carney, T. Zhang, A. Moroz, *J. Phys. Chem. C* **2020**, *124*, 13365.
- [67] L. Wang, Q. Song, Q. Liu, D. He, J. Ouyang, *Adv. Funct. Mater.* **2015**, *25*, 7017.

- [68] K. Kim, Y. M. Lee, H. B. Lee, K. S. Shin, *ACS Appl. Mater. Interfaces* **2009**, *1*, 2174.
- [69] J. Yang, F. Zhang, Y. Chen, S. Qian, P. Hu, W. Li, Y. Deng, Y. Fang, L. Han, M. Luqman, D. Zhao, *Chem. Commun.* **2011**, *47*, 11618.
- [70] J. Zhang, Y. Fu, M. H. Chowdhury, J. R. Lakowicz, *Nano Lett.* **2007**, *7*, 2101.
- [71] Y. Fu, J. Zhang, J. R. Lakowicz, *J. Am. Chem. Soc.* **2010**, *132*, 5540.
- [72] R. Bardhan, N. K. Grady, J. R. Cole, A. Joshi, N. J. Halas, *ACS Nano* **2009**, *3*, 744.
- [73] C. Ayala-Orozco, J. G. Liu, M. W. Knight, Y. Wang, J. K. Day, P. Nordlander, N. J. Halas, *Nano Lett.* **2014**, *14*, 2926.
- [74] J. F. Li, Y. F. Huang, Y. Ding, Z. L. Yang, S. B. Li, X. S. Zhou, F. R. Fan, W. Zhang, Z. Y. Zhou, D. Y. Wu, B. Ren, Z. L. Wang, Z. Q. Tian, *Nature* **2010**, *464*, 392.
- [75] C. Y. Li, M. Meng, S. C. Huang, L. Li, S. R. Huang, S. Chen, L. Y. Meng, R. Panneerselvam, S. J. Zhang, B. Ren, Z. L. Yang, J. F. Li, Z. Q. Tian, *J. Am. Chem. Soc.* **2015**, *137*, 13784.
- [76] G. P. Acuna, F. M. Möller, P. Holzmeister, S. Beater, B. Lalkens, P. Tinnefeld, *Science* (80-. ). **2012**, *338*, 506 LP.
- [77] P. W. K. Rothmund, *Nature* **2006**, *440*, 297.
- [78] J. J. Funke, H. Dietz, *Nat. Nanotechnol.* **2016**, *11*, 47.
- [79] A. Camposeo, L. Persano, R. Manco, Y. Wang, P. Del Carro, C. Zhang, Z. Y. Li, D. Pisignano, Y. Xia, *ACS Nano* **2015**, *9*, 10047.
- [80] G. M. Akselrod, C. Argyropoulos, T. B. Hoang, C. Ciraci, C. Fang, J. Huang, D. R. Smith, M. H. Mikkelsen, *Nat. Photonics* **2014**, *8*, 835.
- [81] T. B. Hoang, G. M. Akselrod, C. Argyropoulos, J. Huang, D. R. Smith, M. H. Mikkelsen, *Nat. Commun.* **2015**, *6*, DOI 10.1038/ncomms8788.
- [82] Y. Wu, J. Xu, E. T. Poh, L. Liang, H. Liu, J. K. W. Yang, C. W. Qiu, R. A. L. Vallée, X. Liu, *Nat. Nanotechnol.* **2019**, *14*, 1110.

- [83] E. M. Carstea, J. Bridgeman, A. Baker, D. M. Reynolds, *Water Res.* **2016**, *95*, 205.
- [84] B. M. Dijkstra, H.-R. (J. R. . Jeltema, S. Kruijff, R. J. M. Groen, *Neurosurg. Rev.* **2019**, *42*, 799.
- [85] F. Leblond, S. C. Davis, P. A. Valdés, B. W. Pogue, *J. Photochem. Photobiol. B Biol.* **2010**, *98*, 77.
- [86] S. A. Hilderbrand, R. Weissleder, *Curr. Opin. Chem. Biol.* **2010**, *14*, 71.
- [87] R. Karoui, C. Blecker, *Food Bioprocess Technol.* **2011**, *4*, 364.
- [88] J. B. Fellman, E. Hood, R. G. M. Spencer, *Limnol. Oceanogr.* **2010**, *55*, 2452.
- [89] J. Kim, Y. Piao, T. Hyeon, *Chem. Soc. Rev.* **2009**, *38*, 372.
- [90] M. Sun, L. Xu, W. Ma, X. Wu, H. Kuang, L. Wang, C. Xu, *Adv. Mater.* **2016**, *28*, 898.
- [91] Y.-L. Luo, Y.-S. Shiao, Y.-F. Huang, *ACS Nano* **2011**, *5*, 7796.
- [92] L. A. Austin, B. Kang, M. A. El-Sayed, *Nano Today* **2015**, *10*, 542.
- [93] B. Kang, M. M. Afifi, L. A. Austin, M. A. El-Sayed, *ACS Nano* **2013**, *7*, 7420.
- [94] Z. Mei, L. Tang, *Anal. Chem.* **2017**, *89*, 633.
- [95] H. Ma, A. Li, Y. Xu, W. Zhang, J. Liu, *Eur. Polym. J.* **2015**, *72*, 212.
- [96] F. Tang, N. Ma, X. Wang, F. He, L. Li, *J. Mater. Chem.* **2011**, *21*, 16943.
- [97] J. Zhang, N. Ma, F. Tang, Q. Cui, F. He, L. Li, *ACS Appl. Mater. Interfaces* **2012**, *4*, 1747.
- [98] Z. Zhu, P. Yuan, S. Li, M. Garai, M. Hong, Q. H. Xu, *ACS Appl. Bio Mater.* **2018**, *1*, 118.
- [99] J. He, S. Li, D. Lyu, D. Zhang, X. Wu, Q. H. Xu, *Mater. Chem. Front.* **2019**, *3*, 2421.
- [100] Y. Cui, C. Niu, N. Na, J. Ouyang, *J. Mater. Chem. B* **2017**, *5*, 5329.
- [101] Y. H. Cheng, T. S. C. Tam, S. L. Chau, S. K. M. Lai, H. W. Tang, C. N. Lok, C. W. Lam, K. M. Ng, *Chem. Commun.* **2019**, *55*, 2761.
- [102] R. Yan, J. H. Park, Y. Choi, C. J. Heo, S. M. Yang, L. P. Lee, P. Yang, *Nat. Nanotechnol.* **2012**, *7*, 191.

- [103] H. Yuan, S. Khatua, P. Zijlstra, M. Yorulmaz, M. Orrit, *Angew. Chemie - Int. Ed.* **2013**, 52, 1217.
- [104] H. Cang, A. Labno, C. Lu, X. Yin, M. Liu, C. Gladden, Y. Liu, X. Zhang, *Nature* **2011**, 469, 385.

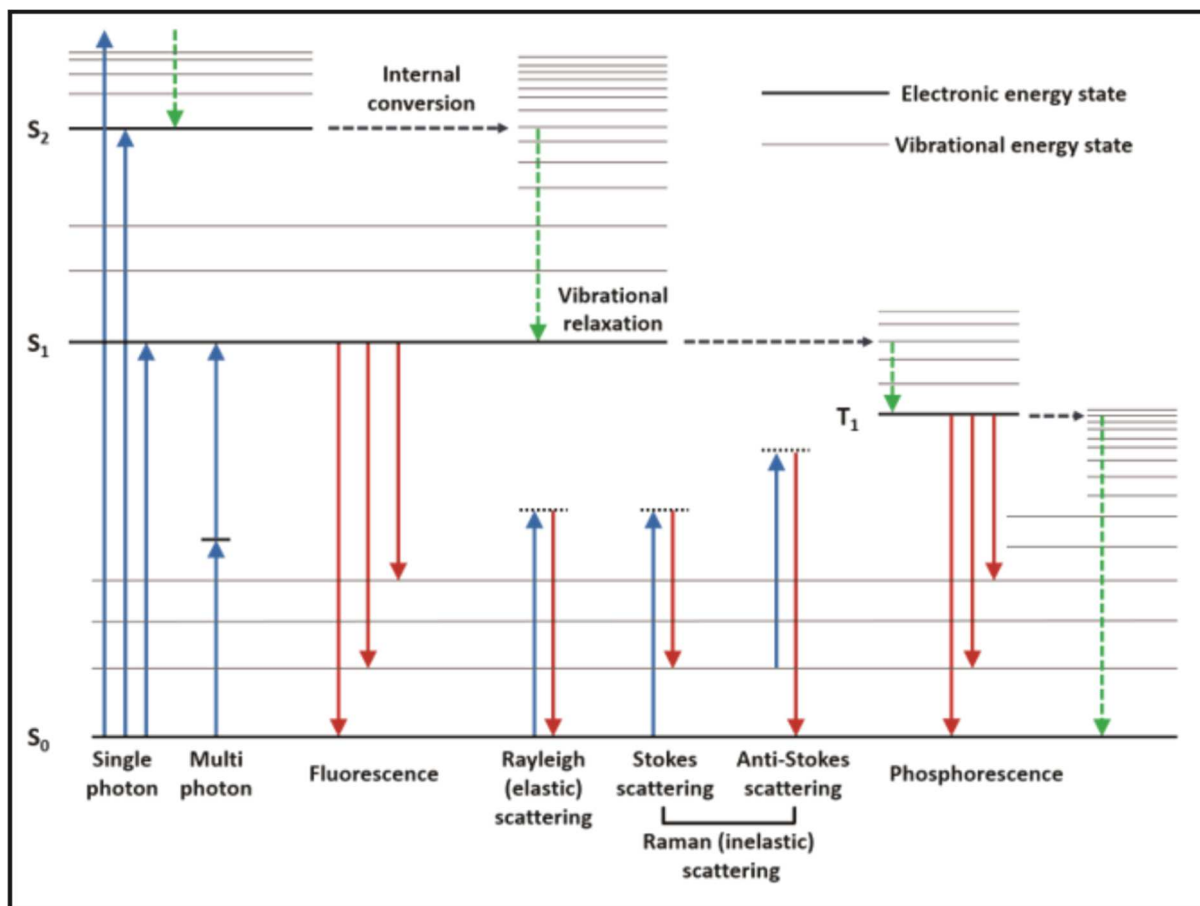


**Figure 1.1.** Fundamentals of optical processes described with a Jablonski diagram.

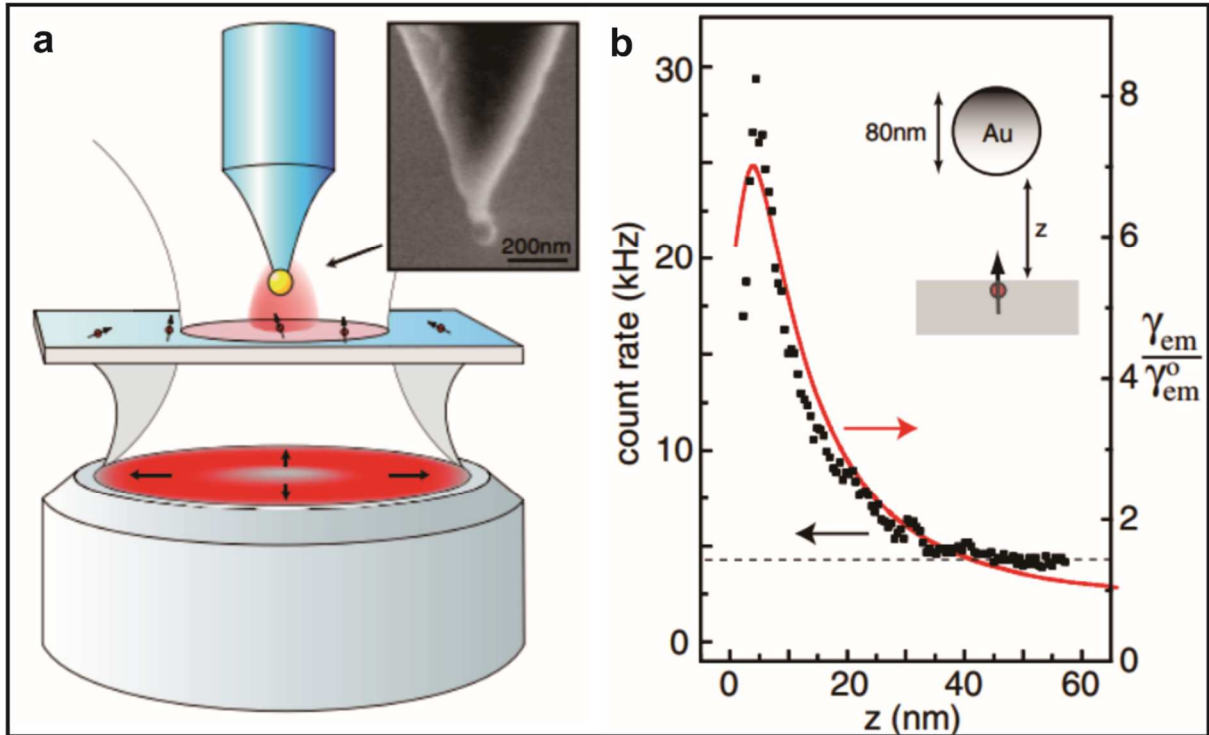


**Figure 1.2.** Distance dependency of PEF activation process. Schematic illustration of experimental arrangement to figure out a dependency of fluorescent emitter-plasmon surface distance for PEF (a) and result (b). The fluorescence rate of a single fluorescent emitter was represented as a function of  $z$ -distance to a single Au nanoparticle attached to the end of a pointed optical fiber. The fluorescence signal continued to increase to 5 nm and then decreased rapidly at a distance below that.

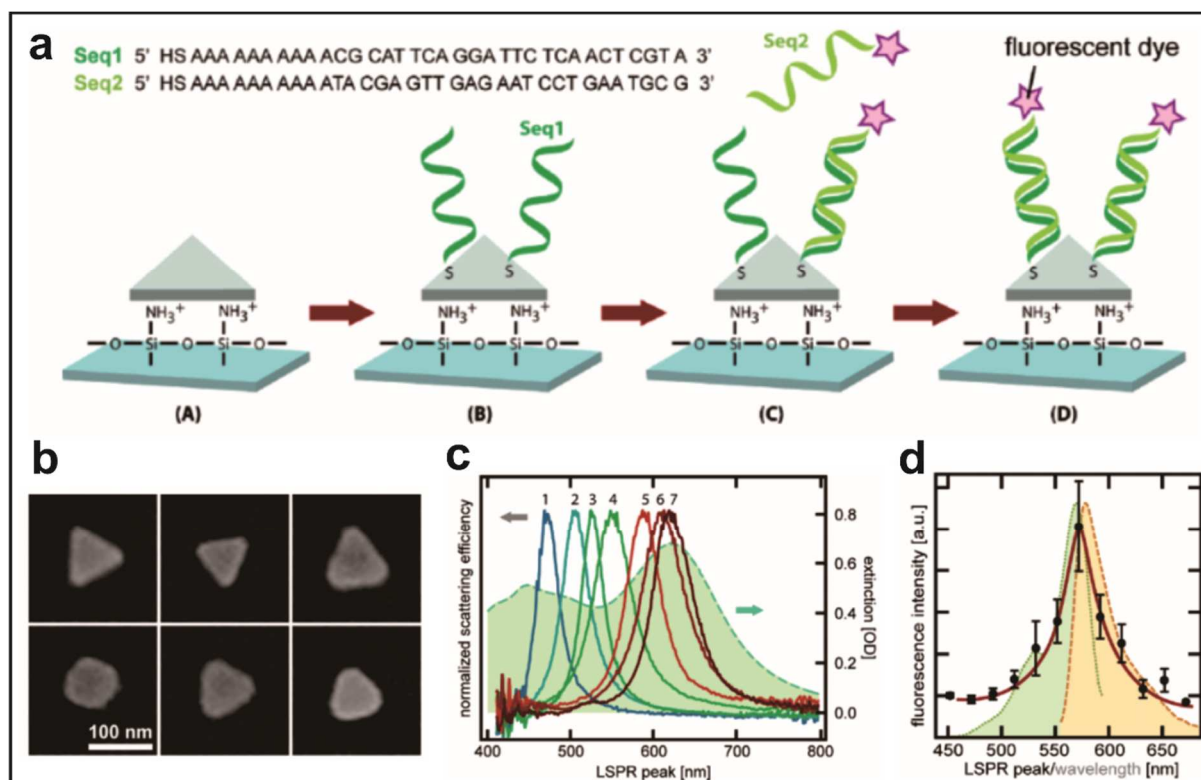


**Figure 1.3.** Effect of plasmonic peak wavelength and fluorescence excitation, emission wavelengths on PEF. The fluorescent emitters were placed on Ag nanoprisms by double stranded DNA (a). Various types of Ag nanoprisms were immobilized on a glass slide (b) and scattering spectra of individual Ag nanoprisms were obtained with darkfield optical microscopy (c). The fluorescence intensities of Rhodimine Red dyes were recorded as a function of the LSPR peak of the Ag nanoprisms in which they are located (d). The excitation spectrum and emission spectrum of Rhodamine Red dye is depicted as dotted line and dashed line in (d).

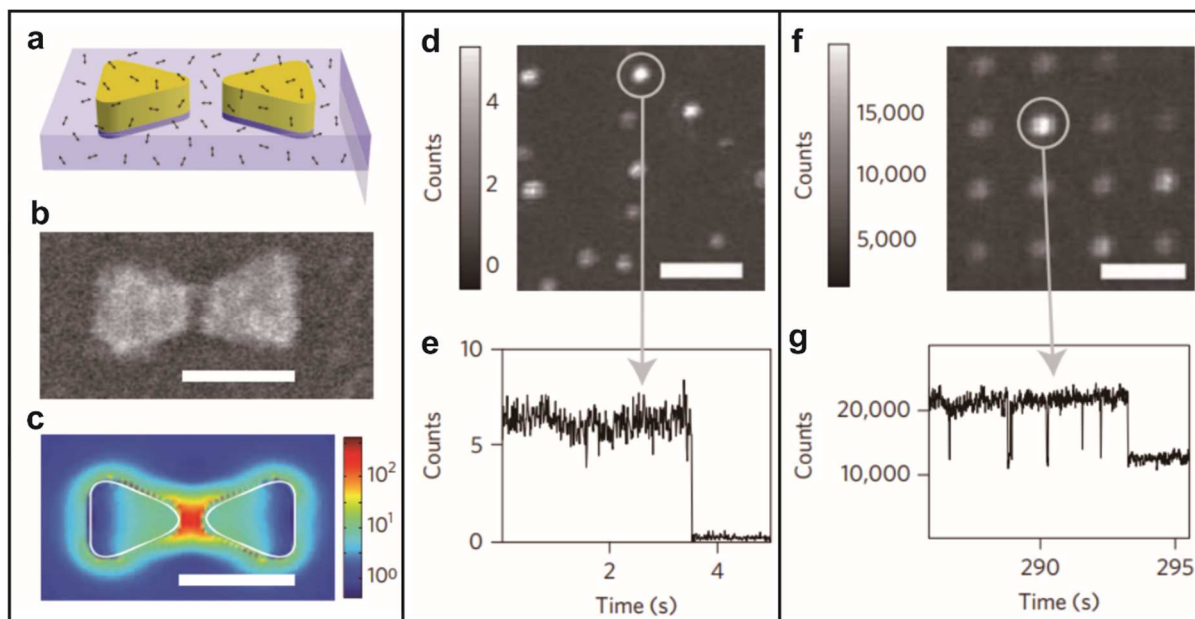


**Figure 1.4.** Au bowtie substrate-based single NIR fluorophore detection experiment. Schematic of diagram (a), SEM image (b), and finite-difference time-domain calculation of Au bowtie nanoantenna coated with *N,N'*-bis(2,6-diisopropyl-phenyl)-1,6,11,16-tetra-[4-(1,1,3,3-tetramethylbutyl)phenoxy]quaterrylene-3,4:13,14-bis(dicarboximide) (TPQDI) molecules (black arrows) in PMMA transparent substrate. Confocal fluorescence scan of a low concentration sample of TPQDI in PMMA without (d, e) and with (f, g) Au bowtie nanoantennas. The fluorescence time trace of a single TPQDI molecule spectrum shows Au bowtie nanoantennas induced fluorescence signal of fluorophore by a factor of 1,340-fold and one-step photobleaching is presented as evidence for single molecule detection

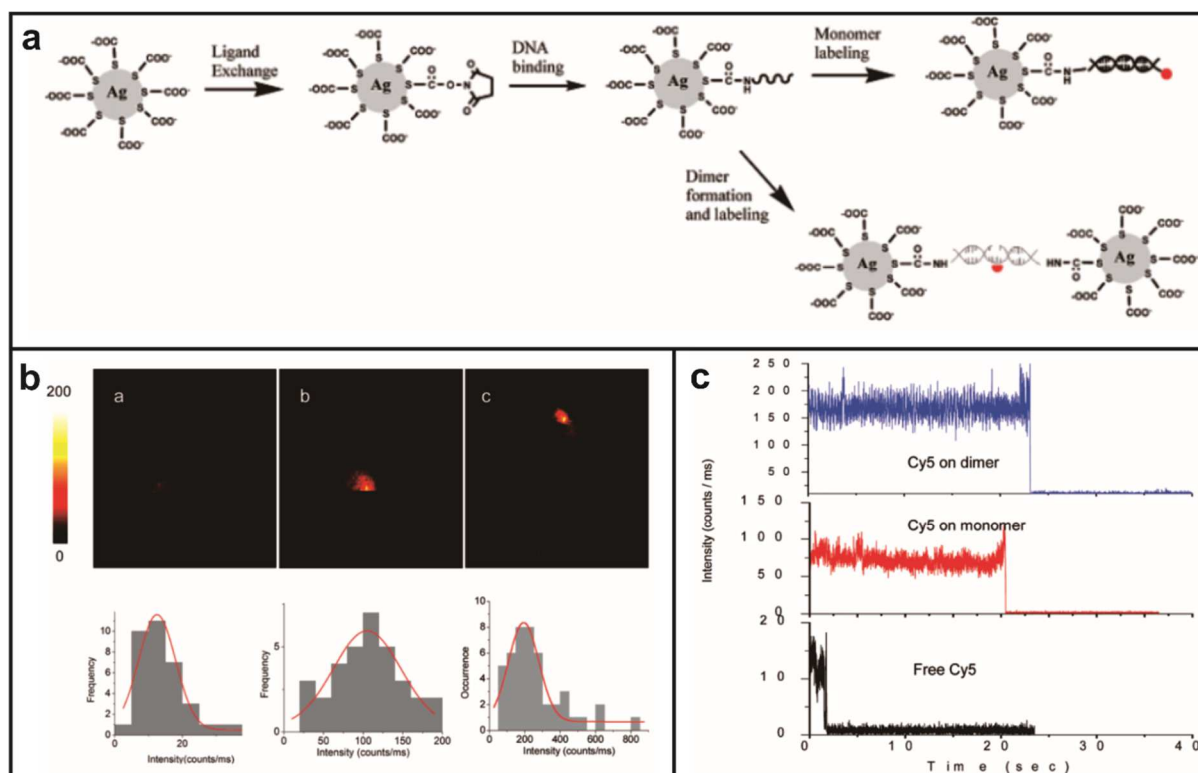


**Figure 1.5.** Single-molecule PEF on Ag monomer and dimer particle. Schematic illustration of preparing Ag dimers (a), representative fluorescence images (b) and time-traces (c) of single fluorophore. Ag dimers were prepared by hybridization of double-length oligonucleotide with oligonucleotides bound on Ag particle. The single fluorophore-based image analysis showed 7-fold and 13-fold fluorescence signal enhancement compared to free Cy5 for Ag monomer and Ag dimer systems respectively.

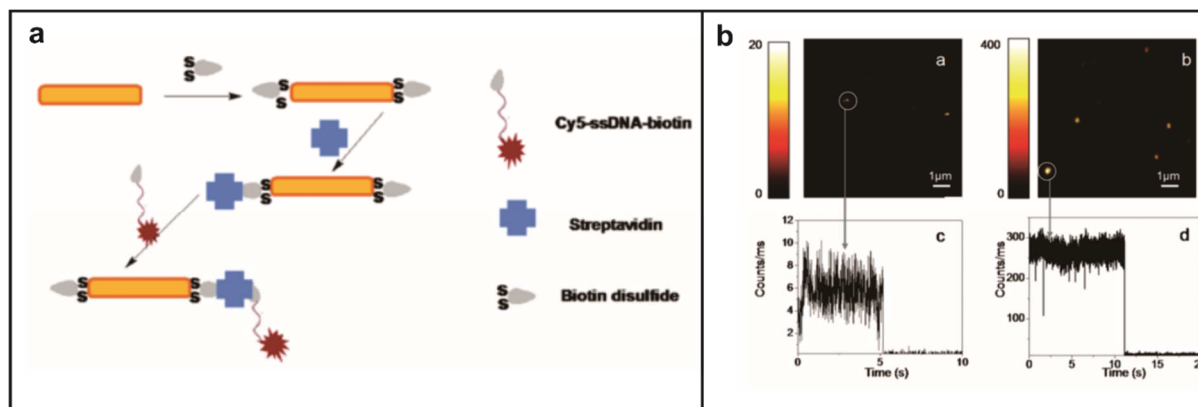


**Figure 1.6.** PEF from single fluorophores end-linked to Au nanorods. Schematic illustration describing conjugation method of a fluorophore-labeled ssDNA to a biotin end-capped Au nanorod (a) and single fluorophore fluorescence measurements (b). The single fluorophore end-linked to Au nanorod showed an approximately 40-fold signal enhancement.

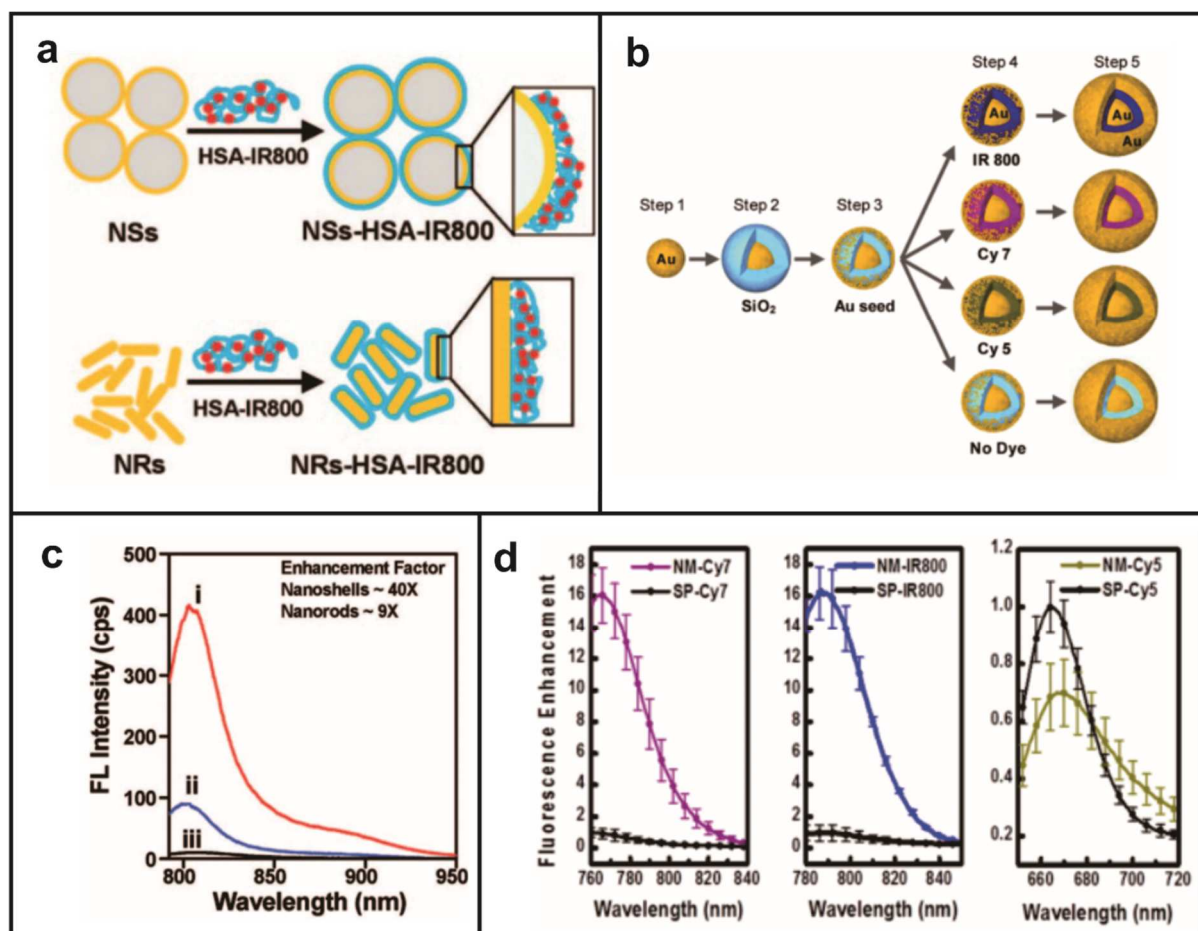


**Figure 1.7.** Au-based PEF-active nanostructures reported in N. J. Halas group. The Au Nanoshells, Au nanorods (a), and Au nanomatyoshka (b) were utilized to enhance fluorescence signal. The Au nanoshells and Au nanorods amplified fluorescence intensities of HAS-IR800 fluorophore by 40 and 9 times respectively (c). The Au shell formation around the Au-seeded Au-SiO<sub>2</sub> core shell nanoparticle [seeded precursor, step 3 in (b) ] enhanced three types of different fluorophores (d).

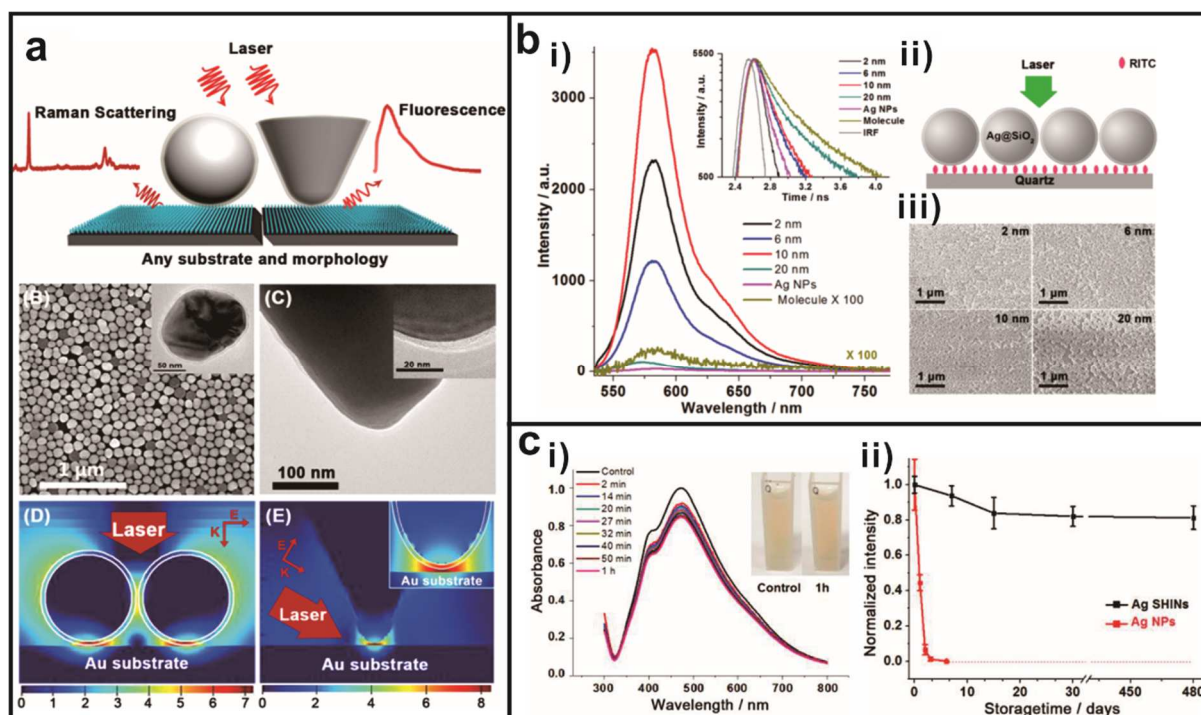


**Figure 1.8.** Shell-isolated Ag nanoparticle/tip for PEF. Schematic diagram and characterization of the shell-isolated Ag nanoparticle/tip nanostructures (Ag SHINs) (a), and PEF measurements (b) and stability test (c) of Ag SHINs. The fluorescence signal of RITC films modified by Ag SHINs with different shell thicknesses were measured and compared with the fluorescence signal of free RITC films, and the largest signal amplification was found in 10 nm (~1000 fold enhancement). The chemical stability of Ag SHINs was tested under 6 wt % H<sub>2</sub>O<sub>2</sub> solution. The extinction spectrum of Ag SHINs remained stable in the 6 wt % H<sub>2</sub>O<sub>2</sub> solution [i] in (c), and fluorescence intensity of Ag SHIN-coated substrate was maintained for a long time [ii] in (c).

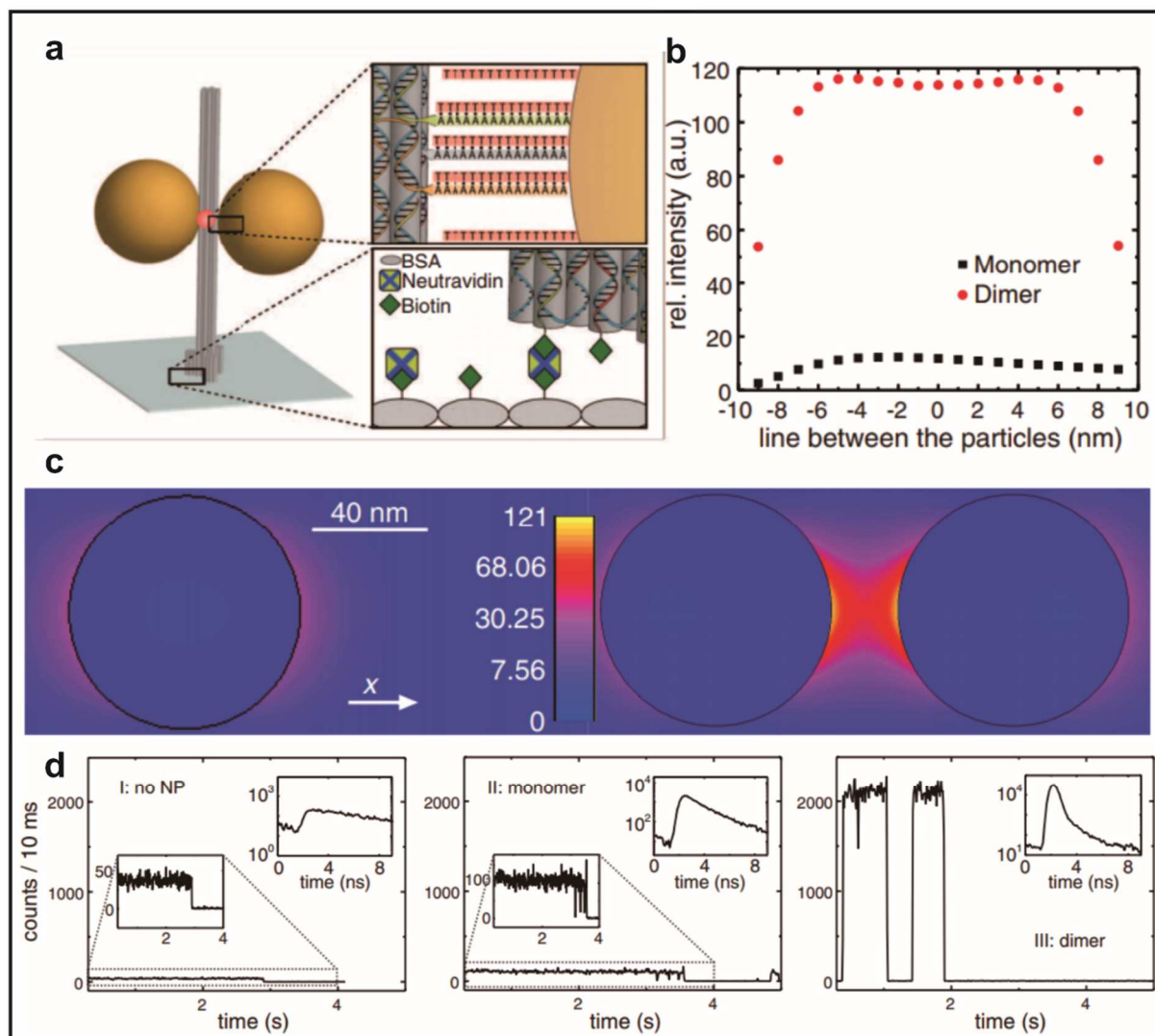


**Figure 1.9.** Spherical Au nanoparticle dimer PEF experiment using DNA origami technique. Sketch of the DNA origami pillar for forming AuNP dimer (a), numerical simulations of the fluorescence enhancement (b) and electric field intensity (c), and time tracking of fluorescence signal of the fluorophore only, AuNP monomer, and AuNP dimer (d)

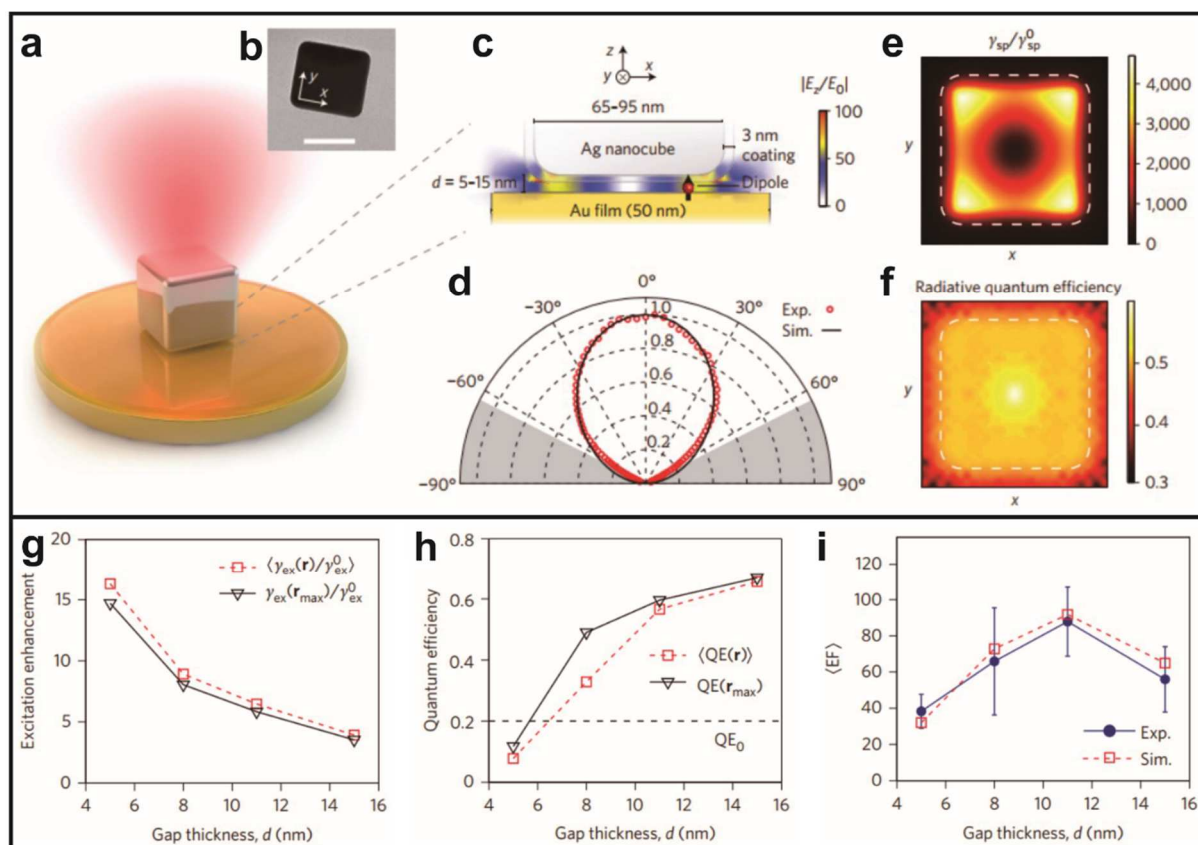


**Figure 1.10.** PEF at plasmonic cavity between colloidal nanoparticle on 2D plasmonic film. Schematic of a Ag nanocube on Au film separated by polyelectrolyte spacer layer (a), TEM image of a single Ag nanocube (b), schematic cross section of film-coupled Ag nanocube (c), simulated (black) and measured (red) radiation pattern from a single nanocube spot on Au film (d), simulation maps of enhancement of the spontaneous emission rate (e) and the quantum efficiency (f), calculated and experimental results of excitation enhancement (g), quantum efficiency (h), and EF (i). The radiation pattern of a Ru dye between a single Ag nanocube and Au film (d) was acquired by angle-resolved single particle fluorescence measurement system. In (g), simulated average excitation rate enhancement for Ru dye in plasmonic cavity (red) and excitation enhancement at the position of maximum emission rate enhancement (black) are shown. In (g), simulated average quantum efficiency (QE) as a function of gap thickness (red) QE at the position of maximum emission rate enhancement (black) are shown.

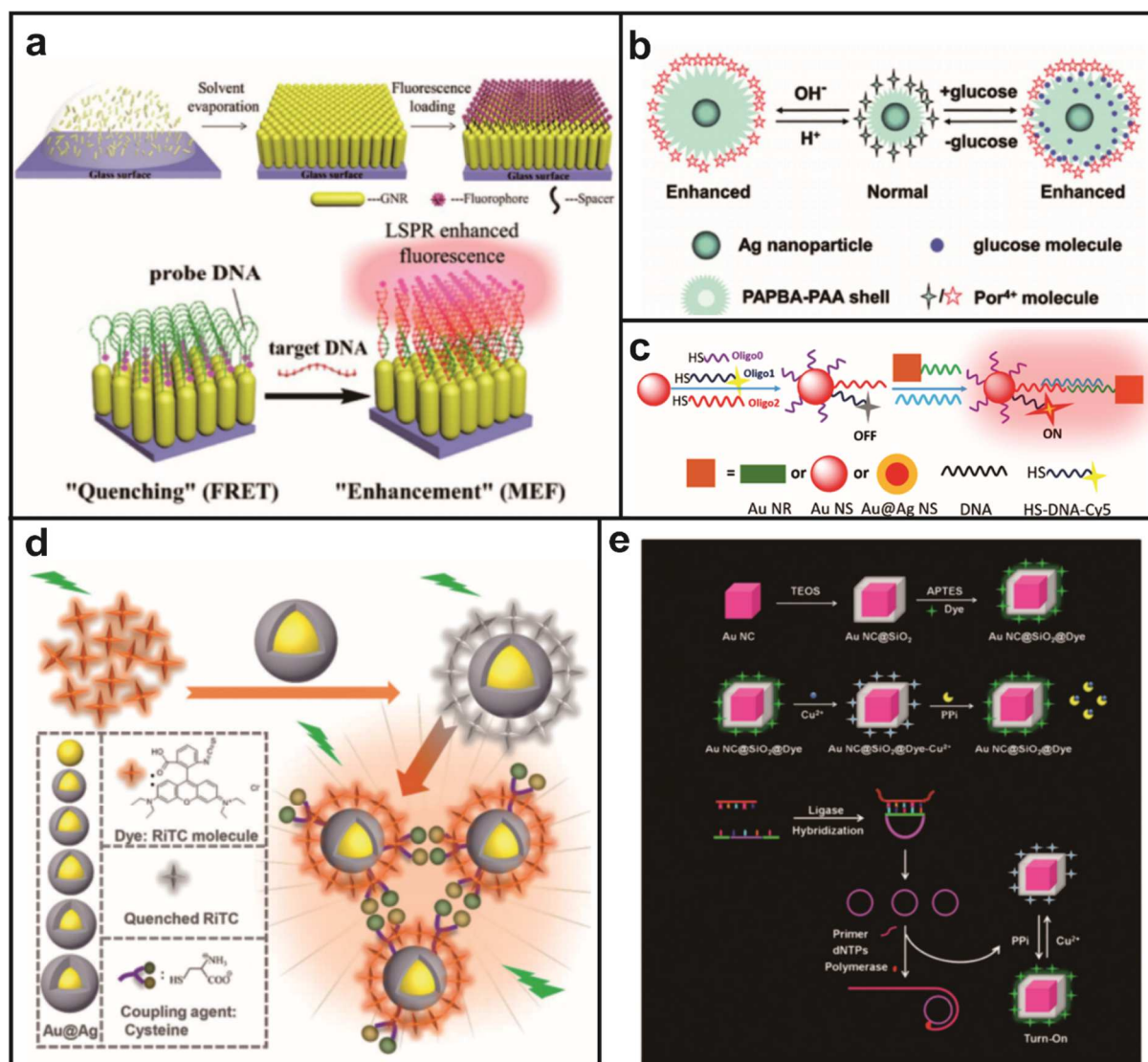


**Figure 1.11.** Representative research cases related to PEF biosensors. Schematic biosensing strategies of AuNR array biochip (a), stimuli-responsive PEF biosensor (b), aggregation-induced target DNA (c) and cysteine sensor (d), and Au nanocube-SiO<sub>2</sub> core-shell nanoprobe for the detection of intracellular biomarkers.

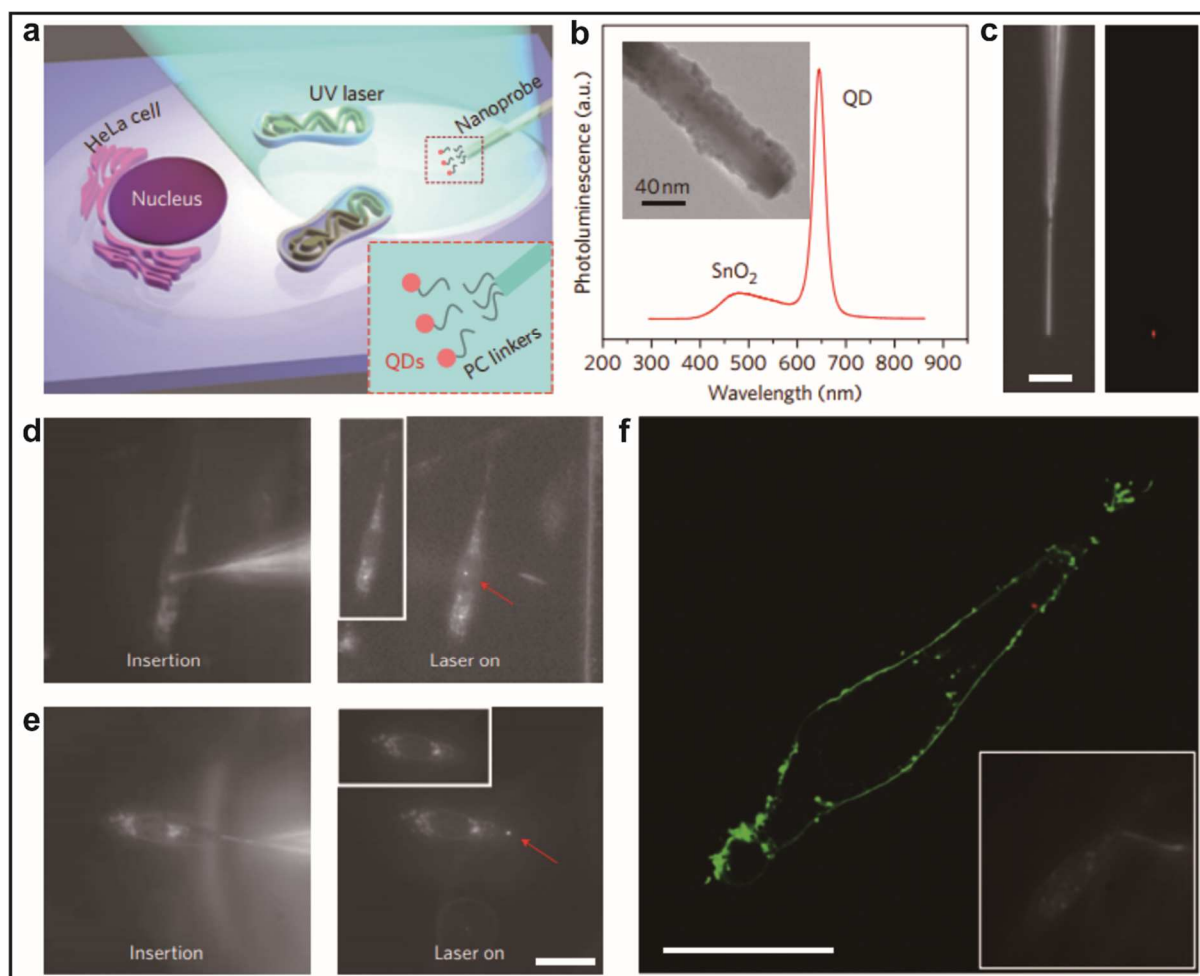


**Figure 1.12.** Spatiotemporal delivery of QDs into a single living HeLa cell using SnO<sub>2</sub> nanowire endoscope. Schematic of the spatiotemporal delivery of QDs into a living cell using a photoactivatable nanowire endoscope (a). Photoluminescence spectrum of a QD (emission, 655 nm)-conjugated SnO<sub>2</sub> nanowire endoscope excited with a focused 325 nm laser and TEM image of the QD-conjugated SnO<sub>2</sub> nanowire (b). Dark-field (left) fluorescence (right) images of the QD-conjugated SnO<sub>2</sub> nanowire endoscope (c). Dark-field images and fluorescence images showing a nanowire endoscope inserted into a cell nucleus (d) and cytoplasm (e) taken after UV irradiation (325 nm, 1 min) was focused on the nanowire tip. Fluorescence confocal image of HeLa cell, showing that the nanowire has delivered the QDs (red dot in the cytoplasm) within the cell membrane (green), which was labelled with an Alexa Fluor 488 conjugate of wheat germ agglutinin (f). The inset of (a) shows QDs conjugated to the nanowire

by photocleavable linkers and inset of (f) shows dark-field image of the cell during QD delivery with a nanowire endoscope. A 488 nm laser was used to excite both the cell membrane stain and the QDs.

## **Chapter 2**

**DNA-Engineerable Ultraflat-Faceted Core-Shell Nanocuboids  
with Strong, Quantitative Plasmon-Enhanced Fluorescence Signals  
for Sensitive, Reliable MiroRNA Detection**

## 2.1. Introduction

Plasmonic nanostructures have been of wide interest mainly due to their designable and useful optical properties including nanoantenna,<sup>1,2</sup> meta-optics,<sup>3,4</sup> surface-enhanced Raman scattering (SERS)<sup>5-10</sup> and plasmon-enhanced fluorescence (PEF) applications.<sup>11-16</sup> In particular, plasmonic metal nanostructures can enhance fluorescence signals of fluorophore dyes when fluorophores are placed near their surfaces,<sup>14,16-21</sup> and the distance between a fluorophore and metal surface is the critical parameter in controlling PEF intensity. In general, the distance needs to be a few nm in maximizing fluorescence enhancement and also in effectively diminishing quenching effect due to energy transfer. PEF nanostructures can be immediately utilized in various biomedical applications because many of the conventional biodetection and bioimaging platforms are based on fluorescence. As high as  $\sim 10^3$  PEF enhancement factor (EF) has been reported with a single-molecule measurement or near-infrared (NIR) dyes that have a low quantum yield.<sup>21-27</sup> However, it should be noted that one or a few molecule measurement-based FEF EF results, particularly with dried samples, could be misleading or overestimated, and ensemble-average measurement-based PEF EF with bulk solution samples has been only as high as  $10^1$ - $10^2$  with widely used high quantum-yield dyes.<sup>28-39</sup> Therefore, the key challenge could be controlling the distances between dyes and metal particle surface in an ultra-precise manner for a large number of particles and stabilizing these particles because the fluorescence signal of FEF probes can be enhanced or quenched very sensitively depending on the position of fluorophore dyes, particularly in actual application samples such as serum.<sup>14,16,40</sup>

Here, we designed and synthesized fluorescence-amplified nanocuboids (FANCs) that can generate strong, reproducible PEF signals, particularly after fluorescent silica shell formation, and developed microarray-based microRNA (miRNA) detection assays that can reliably detect miRNA from 100 aM to 1 pM concentration range (Figure 2.1). A fluorophore dye is modified to the tip of DNA to control the distance between the dye and metal particle

surface, and the other end of DNA is modified with a thiol to be anchored to Au nanoparticles. These functionalized DNA strands are then densely modified to Au nanorods (NRs), and Ag nanoshell is then grown on AuNRs to engineer to the distance between fluorophore dyes and Au surface to form FANCs with ultraflat surfaces. Importantly, we then stabilized and increased fluorescence signals from each particle by forming fluorescence silica shell-coated FANCs (FS-FANCs), which can also fixate fluorophore dye positions inside the shell while embedding more fluorophore dyes into the shell. It is critical to fix the location of optimally positioned fluorophore dyes by embedding them in a silica shell to minimize the fluorescence signal fluctuation and loss based on position changes of the modified dyes in solution. Computational modeling study results match well with the experimental results, and show that the vertex and vertex-neighboring areas of FANCs are the major areas for the strong fluorescence enhancement. We then used these FS-FANC probes for detecting miRNA targets that play key roles in multiple biological processes and diseases such as cancer, Alzheimer's disease, and myocardial disease<sup>41</sup> in a microarray platform. However, the microarray methods offer high-throughput capability but have relatively low sensitivity because sample size is typically small and there is no target amplification step.<sup>42,43</sup> We replaced chemical fluorescent tags with our FS-FANCs and acquired a very high sensitivity with a wide and reliable dynamic range (100 aM to 1 pM). The FS-FANC-based microarray results achieved  $>10^3$ -fold better sensitivity with a much more improved quantification range than chemical fluorophore-based miRNA microarray assays.

## 2.2. Experimental Section

### Reagents and Materials

Chemical reagents including  $\text{HAuCl}_4 \cdot 3\text{H}_2\text{O}$ , CTAB,  $\text{NaBH}_4$ , L-ascorbic acid,  $\text{AgNO}_3$ , sodium-dodecyl sulfate (SDS), sodium chloride (NaCl), dithiothreitol, CTAC, polyvinylpyrrolidone (PVP), EtOH, MeOH, (3-aminopropyl)-triethoxysilane (APTES), dimethylamine, tetraethyl orthosilicate (TEOS), acetonitrile, disuccinimidyl carbonate (DSC), N,N-Diisopropylethylamine (DIPEA), phosphate buffered saline (PBS), phosphate buffered saline with 0.05% TWEEN® 20, pH 7.4 (PBST), SSPE Buffer 20× Concentrate, SSC Buffer 20× Concentrate, sodium dodecyl sulfate (SDS), Bovine serum albumin (BSA), Succinic anhydride ( $\text{C}_4\text{H}_4\text{O}_3$ ), N-Hydroxysulfosuccinimide sodium salt (Sulfo-NHS,  $\text{C}_4\text{H}_4\text{NNaO}_6\text{S}$ ), Triethylamine ( $(\text{C}_2\text{H}_5)_3\text{N}$ ), N-(3-Dimethylaminopropyl)-N'-ethylcarbodiimide hydrochloride (EDC,  $\text{C}_8\text{H}_{17}\text{N}_3 \cdot \text{HCl}$ ), Glycerol ( $\text{HOCH}_2\text{CH}(\text{OH})\text{CH}_2\text{OH}$ ), 2-(N-morpholino)ethanesulfonic acid hydrate (MES hydrate) were purchased from Sigma-Aldrich (St. Louis, MO, USA). Diethyl pyrocarbonate (DEPC) was obtained from Biosesang (Seongnam-si, Gyeonggi-do, Korea). HPLC-purified fluorophore-modified thiolated oligonucleotides were purchased from IDT Inc. (Coralville, IA, USA) and reduced by using dithiothreitol (DTT, 0.1M) in a phosphate buffer (170 mM, pH = 8.0). The reduced oligonucleotides were then purified through a desalting NAP-5 column (Sephadex G-25 medium, DNA grade). NANOpure  $\text{H}_2\text{O}$  (>18.0 M $\Omega$ ), purified using a Milli-Q water purification system, was used for all experiments. Alexa Fluor™ carboxylic acid, succinimidyl ester fluorophores were purchased from Molecular Probes (Eugene, Oregon, USA). All HPLC-purified oligonucleotides for miRNA detection experiments were custom-synthesized at Integrated DNA Technologies, Inc. (Coralville, IA, USA) (Table S1). The mouse monoclonal antibody S9.6 directed to DNA/RNA hybrids was purchased from Kerafast (Boston, USA) or Millipore Sigma (Darmstadt, Germany). Secondary antibody detection reagents (Cy™5-

labeled goat anti-mouse IgG, purified goat anti-mouse IgG) were obtained from KPL (Gaithersburg, MD, USA). NSB9 NHS slides for microarray were purchased from NB POSTECH, Inc. (Pohang-si, Gyeongsangbuk-do, Korea). RNaseZap (Ambion, USA) was used to completely remove RNase contamination from experimental tools and glassware. 8-well gasket slides and microarray hybridization chambers were purchased from Agilent Technologies (Santa Clara, USA). The formvar/carbon coated copper grid (Ted Pella, Inc. Redding, CA, USA), HR-TEM (JEM ARM 200F, JEOL, Japan, 200 kV) and FEI Company (Hillsboro, Oregon, USA), 200 kV) equipped with energy dispersive spectroscopy (EDS) unit (EDAX) was used for elemental mapping and lattice analysis, and other TEM images were obtained using JEM-2100 (JEOL, Japan, 200 kV). Inductively coupled plasma emission spectrometer (ICP-ES, ICPS-7510, Shimadzu, Japan) was used to measure the mass concentration of AuNRs, and the steady state spectrofluorometer (FS5 Spectrofluorometer, Edinburgh Instruments Ltd, Kirkton Campus, UK) was used for fluorescence measurements. Field emission scanning electron microscope (FE-SEM, Helios 650, FEI, USA) was used for SEM measurements. A hybridization oven was purchased from N-BIOTEK, Inc. (Bucheon-si, Gyeonggi-do, Korea). A microarrayer (Q-Array Mini, Genetix) was used for fabricating DNA arrays. The fluorescence signal of the microarray was measured with fluorescence scanners (Axon GenePix 4000B and 4100A). Atomic force microscopy (AFM) images were obtained by NanoWizard III AFM (Bruker, Berlin, Germany) equipped with a fluorescence microscope (Zeiss, Oberkochen, Germany).

## **Preparation of AuNRs**

We prepared AuNRs in an aspect ratio value of  $\sim 4.0$  based on a seed-mediated method with slight modifications. The seed was prepared by mixing 5 ml of 0.5 mM  $\text{HAuCl}_4 \cdot 3\text{H}_2\text{O}$  solution with 5 ml of 0.2 M CTAB, followed by rapidly adding 600  $\mu\text{l}$  of ice-cooled 0.01 M  $\text{NaBH}_4$

solution. The seed solution was used for 2 hours after a reducing step. The 5 ml of 0.5 mM  $\text{HAuCl}_4 \cdot 3\text{H}_2\text{O}$  solution was mixed with 5 ml of 0.2 M CTAB solution, and 200  $\mu\text{l}$  of  $\text{AgNO}_3$  solution was added. 70  $\mu\text{l}$  of 78 mM L-ascorbic acid was added. After gently mixing, 12  $\mu\text{l}$  of seed solution was added and incubated over 4 hours. These AuNRs were characterized by TEM analysis, UV-visible spectroscopy and ICP-AES analysis (Figure 2.2). The size and aspect ratio of 202 AuNRs were analyzed by ImageJ software. The size of AuNR was 50.32 (4.26) nm  $\times$  12.81 (0.94) nm, and aspect ratio value was 3.95 (0.42). The ICP-AES analysis showed gold concentration of prepared AuNR solution was 69.5  $\mu\text{M}$ , when absorbance at 520 nm was 0.249, and calculated mole extinction coefficient ( $\epsilon$ ) at 520 nm was  $1.374 \times 10^9$ . The transverse and longitudinal modes appeared at 510 and 765 nm respectively.

### **Preparation of DNA-modified AuNRs**

We tethered Alexa Fluor<sup>TM</sup> 647-modified thiolated oligonucleotides to pre-synthesized AuNR surface. The sequence of Alexa Fluor<sup>TM</sup> 647-modified thiolated oligonucleotides is 5'-Alexa Fluor<sup>TM</sup> 647-CACGCGTTTCTCAAA-PEG<sub>6</sub>-AAAAAAAAAAA-(CH<sub>2</sub>)<sub>3</sub>S-3'. The melting temperature of this oligonucleotide in 50 mM NaCl solution is 52.7 °C, and the extinction coefficient at 260 nm is 291,600 M<sup>-1</sup>·cm<sup>-1</sup>. First, 1500  $\mu\text{l}$  of freshly reduced 5.25  $\mu\text{M}$  Alexa Fluor<sup>TM</sup> 647-modified thiolated oligonucleotide solution. At first, 1500  $\mu\text{l}$  of freshly reduced 5.25  $\mu\text{M}$  Alexa Fluor<sup>TM</sup> 647-modified thiolated oligonucleotides solution and 67.8  $\mu\text{l}$  of 10 % SDS solution were mixed with 4500  $\mu\text{l}$  of 1.16 nM pre-synthesized AuNR solution. The mixed solution was incubated for 30 minutes at room temperature. The solution was then adjusted to obtain a final phosphate concentration of 10 mM (pH 7.4) with 100 mM phosphate buffer and incubated at room temperature for 30 minutes. The adjusted solution was brought to 0.3 M NaCl by the addition of three aliquots of 2 M NaCl (10 mM PB, 0.1 % SDS) solution per every 20min in boiled water. After 1 hour from the last addition, the colloid solution was centrifuged

(9,500 rpm, 10 min) two times and the precipitate was redispersed in deionized water. Before Ag shell growth step, we measured OD at 520 nm by an UV-visible spectrophotometer to determine particle concentration.

### **Quantification of modified oligonucleotides per AuNR**

To determine the number of fluorophore-modified oligonucleotides loaded on each AuNR particle, the concentration of AuNR nanoparticles and the concentration of fluorescent oligonucleotides in each sample were measured. UV-visible spectrophotometer was used to determine the concentration of AuNR solution in each aliquot. The concentration of AuNR is directly related to the absorbance value via Lambert-Beer's law ( $A = \epsilon bc$ ). The mole extinction coefficient we used was  $1.374 \text{ M}^{-1}\text{cm}^{-1}$  at 520 nm. To determine the concentration of fluorescent oligonucleotides in each aliquot, 100  $\mu\text{l}$  of the oligonucleotides modified on AuNR solution was mixed with same volume of 100 mM KCN solution to destroy AuNR crystal structure, detaching oligonucleotides from AuNR surface. In this step, the concentration of oligonucleotides is diluted by factor of 2. After 2-hour incubation, the oligonucleotides were released into solution after incubation, and then fluorescence intensity of supernatant was measured. The fluorescent intensity was compared with free Alexa Fluor<sup>TM</sup> 647-modified thiolated oligonucleotides-based standard curve, and the three different batches were measured to obtain standard deviation (Figure 2.3). During the fluorescent measurements, the fluorophore was excited at 620 nm. Averagely, 464.2 fluorescent oligonucleotides were attached onto one AuNR particle.

### **Fluorescence measurements**

To analyze fluorescence activity and determine fluorescence enhancement factors, the steady state spectrofluorometer (FS5 Spectrofluorometer, Edinburgh Instruments Ltd, Kirkton

Campus, UK) was used. The quantum yield (QY) of the Alexa Fluor™ 647 modified on oligonucleotide was measured by the absolute quantum yield spectrometer (C13534-34, Hamamatsu Photonics, Shimokanzo, Japan). And the fluorescence enhancement factor was calculated as,

$$EF = \left( \frac{|(I_{PEF}) \cdot (C_{ref})|}{|(C_{PEF}) \cdot (I_{ref})|} \right)$$

where  $I_{PEF}$ ,  $C_{PEF}$  are integrated fluorescence intensity and concentration of fluorophores of FANC solution, and  $I_{ref}$ ,  $C_{ref}$  are reference integrated fluorescence intensity and concentration of fluorophores in free space.

### **Preparation of FS-FANCs**

To make FS-FANCs, FANC-4 was coated with polyvinylpyrrolidone (PVP). At first, 500  $\mu$ l of **FANC-4** solution (0.59 nM) was mixed with 50  $\mu$ l of 1 % SDS and 500  $\mu$ l of 2.5 % PVP (average MW = 40,000, in DIW). After 1 hour incubation at 25 °C, the solution was centrifuged twice and redispersed in 50  $\mu$ l of deionized water. For fluorescent silica shell, 2  $\mu$ l of 0.5 % (v/v, in EtOH) (3-aminopropyl)-triethoxysilane (APTES) was mixed with 40.0  $\mu$ l of carbonate buffer (pH 8.5) and 10  $\mu$ l of 0.8 mM (in DMF) carboxylic succinimidyl ester-tagged Alexa Fluor™ 647. After 12-hour incubation under room temperature, the solution was mixed with 50  $\mu$ l of prepared PVP-coated **FANC-4** (in deionized water) and incubated for 30 minutes. After that, 450  $\mu$ l of EtOH, 25  $\mu$ l of 1.0% (v/v, in EtOH) tetraethyl orthosilicate and 50.0  $\mu$ l of dimethylamine solution were added. The solution was incubated at 30 °C. After 2 hour incubation, 25  $\mu$ l of 0.25% (v/v, in EtOH) tetraethyl orthosilicate added and the solution was further incubated at 30 °C for 12 hours. The solution was mixed with 650  $\mu$ l of DMSO and centrifuged two times (5000 rpm, 15 min) and redispersed in 100  $\mu$ l DMF.

## **Preparation of FS-NCs**

The 500  $\mu$ l of AuNR solution (0.5 OD at 520 nm) was serially mixed with 500  $\mu$ l of 10 mM CTAC, 500  $\mu$ l of 1.0 mM AgNO<sub>3</sub> and 500  $\mu$ l of 0.1 M L-ascorbic acid. The relative ratios of reagents to AuNR are equivalent to **FANC-4** synthetic procedures. The mixture was incubated at 60 °C for 3 hours. After that solution was centrifuged twice and redispersed in 500  $\mu$ l of deionized water. The subsequent PVP coating and fluorescent silica shell formation processes were the same as those of preparation of FS-FANCs case.

## **Quantification of fluorophores in a silica shell**

To determine the number of fluorophores loaded on each FS-NC, 0.2 nM FS-NC solution was mixed with same volume of 100 mM KCN solution to destroy Au-Ag core-shell nanocuboid structure. In this step, the concentration of fluorophore is diluted by factor of 2. After 2-hour incubation, fluorescence intensity of the supernatant was measured. The fluorescent intensity was compared with free Alexa Fluor™ 647 fluorophore-based standard curve, and the three different batches were measured to obtain standard deviation (Figure 2.4). During the fluorescent measurements, the fluorophore was excited at 620 nm. Averagely, 463.8 fluorophores were embedded in one FS-NS particle.

## **Simulation Method**

The electric near-field, radiative enhancement, and QY were calculated with the boundary-element method using the MNPBEM toolbox. Since the metal-enhanced fluorescence consists of two steps, (enhanced electric field, and quenching due to the plasmonic nanoparticle), the enhancement factor of each fluorophore is represented as,

$$EF = \left( \frac{|\vec{p}(\lambda_{em}) \cdot \vec{E}(\lambda_{exc}, \vec{r})|}{|\vec{p}(\lambda_{em}) \cdot \vec{E}_0(\lambda_{exc}, \vec{r})|} \right)^2 \frac{Q_r}{Q_r^o}$$

where  $\lambda_{exc}$ ,  $\lambda_{em}$  are excitation (620nm), emission (668nm) wavelengths,  $\vec{p}$  is the electric dipole moment of a fluorophore.  $\vec{E}$  ( $\vec{E}_0$ ) is the incident electric field in the presence (absence) of the FANC particle,  $\vec{r}$  is the positions of the fluorophores. To consider the location ( $\vec{r}$ ) and orientation ( $\vec{p}$ ) of each fluorophore molecule, we first distributed 315 fluorophores to have the same distance from the core surface. The distance ranges from 7 nm to 12.5 nm. The fluorophores located at less than 3 nm away from the shell were considered as quenched. Finally,  $Q_r$  ( $Q_r^o$ ) is the QY of the fluorophore molecule in the presence (absence) of the FANC particle.  $Q_r$  is calculated from the radiative decay rate divided by total decay rate, and  $Q_r^o = 0.285$ . We only considered three principal axes as the dipole orientations and longitudinal polarization of the incident light.

### **Preparation of N-hydroxysuccinimide (NHS)-modified surface**

To generate an NHS group on surface, 9-acid dendron-modified slides (NB POSTECH, Inc.) were activated by immersing in an acetonitrile solution containing DSC (25 mM) and DIPEA (1.0 mM) for 2 h under nitrogen. After the reaction, the slides were washed with ethanol and dried for 2 h under vacuum (80 mTorr).

### **Fabrication of DNA probes on NHS-activated slides**

Amine-labeled probe DNA (20  $\mu$ M) dissolved in 3 $\times$  SSC buffer (pH 8.5) containing 0.17 mM SDS, 14.9 mM betaine, and 6.2 mM  $\text{NaN}_3$  were printed on the above NHS slides (NB POSTECH, Inc.) using a microarrayer (Q-Array Mini, Genetix) in a clean room (class 10,000). In order to use an 8-well gasket slide for the hybridization (*vide infra*), 3 x 3 spots at positions of each well were fabricated on NHS activated slides. After spotting, the slides were kept in a humidity chamber (67%) at room temperature overnight. Subsequently, the slides were washed

with 2× SSPE buffer (pH 7.4) containing 7.0 mM SDS at 37 °C for 10 min with stirring and rinsed with deionized water. The residual water was removed by centrifugation at 1,000g for 1 min, and the slides were dried under vacuum (80 mTorr) for 2 h. Dried slides were placed in a blocking solution containing 50 mM ethanolamine in PBS (pH 8.5) for 2 h with gentle shaking. Then the slides were washed with PBST and deionized water, and residual water was removed by centrifugation at 1,000g for 1 min, and the slides were kept under vacuum (80 mTorr).

### **Hybridization of target miRNAs with probe DNA spots**

To remove RNase enzymes, experimental utensils and glassware were cleaned with RNaseZap (Ambion) and ethanol, and deionized water was treated with diethyl pyrocarbonate (DEPC, 0.05% (v/v)) for 12 h and subsequently autoclaved. The synthetic target RNA and non-complementary RNA (miR 132-3p) were diluted to the desired concentration using 2× SSPE buffer (pH 7.4) containing 7.0 mM SDS. Samples containing 1 pM, 100 fM, 10 fM, 1 fM, 100 aM of miR-134, and 1 pM of miR-132-3p were prepared. The RNA solutions were denatured at 95 °C for 3 min and cooled on ice for 3 min, then 50 µL of each sample was loaded at a pre-assigned well of the gasket slide. After assembling the gasket slide with the microarrayed slide by using the chamber, the whole kit was placed in a hybridization oven (34 °C) for 18 h. After the hybridization, the slide was briefly rinsed with the hybridization buffer. Subsequently, the slide was placed in the hybridization buffer (45 °C) with stirring for 10 min, and the same washing process was followed with 0.2× SSC buffer. The residual liquid was removed by centrifugation at 1,000g for 1 min and the slides were stored at 4 °C.

### **Preparation of goat anti-mouse IgG antibody-tethered FS-FANC**

The 20 µL of prepared FS-FANC solution in DMF mixed with DMSO (80 µL), trimethylamine (2.0 µL) and succinic anhydride (1.0 mg/ml; 100 µL, in DMSO). The mixture was incubated at

30 °C for 20 min. After the incubation, the mixture was placed in a centrifuge and spun at 8500 rpm for 8 min to remove supernatant (two times), and then redispersed in 100 mL of 10 mM MES buffer (pH 5.5). For the EDC coupling 2.5 µL of 40 mM EDC·HCl (in 10 mM MES) and 2.5 mL of 100 mM sulfo-NHS (in 10 mM MES) were added to the FS-FANC solution, and the mixture was incubated for 15 min at 30 °C. After the incubation, goat anti-mouse IgG (1.0 mg/ml, 8 ml) was added to the mixture, and the solution was incubated for 12 h with shaking at 30 °C. The antibody-tethered FS-FANC was purified by centrifugation at 3,000 rpm and 6,000 rpm for 3 min for each to remove free antibody, and re-suspended in 100 µL of 0.10 % (w/v) BSA solution (in MES buffer). The centrifugation process was repeated two more times. After the third centrifugation, the solution was re-dispersed with 50 µL of 10 % (w/v) BSA solution (in pH 5.5 MES buffer) and diluted with 450 µL of PBST (0.2 M NaCl) before using.

### **MicroRNA detection using FS-FANCs**

To quantify the DNA/miR-134 duplex on a slide, S9.6 antibody was diluted in PBS with 0.05% (v/v) Tween 20 (PBST, pH 7.4) containing 2.0 % (w/v) BSA and the resulting solution (40 µL) was loaded at every well of the gasket slide. After assembling the gasket slide with the microarrayed slide by using the chamber, the whole kit was placed in a hybridization oven (34 °C) for 1h. After the incubation, the slide was washed with PBST buffer. The slide was then incubated with 60 µL of the above prepared goat anti-mouse IgG conjugated Si-FANCs for 1 h. Finally, the slide was plunged in PBST buffer twenty times, centrifuged for 1 min at 1,000 g to remove all residual liquid. And the slide was scanned in either an Axon GenePix 4000B or 4100A fluorescence scanner. Data were collected using GenePix Pro 7.0 program and analyzed using an in-house MATLAB program.

## **AFM imaging experiments**

To examine the correspondence between the fluorescence intensity and the number of Si-FANCs, AFM images were obtained in an ambient condition after the fluorescence scanning. The surface was imaged using NanoWizard III AFM (Bruker, Berlin, Germany) and PR-T190 monolithic silicon AFM probe (Probes, Seoul, Korea). Each spot was scanned in the intermittent contact mode at a scan rate of 0.30 Hz (Scanned area was  $80 \times 80 \mu\text{m}^2$ ;  $1024 \times 1024$  pixels). The particle number and the area occupied by the particles were obtained by using JPK data processing program and Image J program.

## 2.3. Results and Discussion

### Synthesis of FANCs

In a typical experiment, we first prepared Au nanorods (AuNRs) with an aspect ratio of  $\sim 4.0$  using a seed-mediated method with slight modifications of the published method.<sup>44</sup> We obtained AuNRs with  $50.32 \pm 4.62$  nm in length and  $12.81 \pm 0.94$  nm in width (the aspect ratio of  $3.95 \pm 0.42$ , Figure 2.2). The molar extinction coefficient ( $\epsilon$ ) at 520 nm is  $1.37 \times 10^9$ , and the transverse and longitudinal modes appear at 510 and 765 nm, respectively. We then modified Alexa Fluor<sup>TM</sup> 647-modified thiolated oligonucleotides to AuNRs, followed by salting process. We found  $\sim 464$  fluorescent oligonucleotides were modified per AuNR particle (Figure 2.3). Before the Ag shell growth step, we measured the OD at 520 nm with an UV-visible spectrophotometer to determine particle concentration.

Next, we formed an Ag shell on DNA-modified AuNRs (DNA-AuNRs) and gradually increased Ag shell thickness. We diluted AuNR solution to obtain 0.5 OD at 520 nm. The diluted AuNR solution (100  $\mu$ l) was serially mixed with CTAC, AgNO<sub>3</sub> and 0.1 M L-ascorbic acid solution, and incubated at 60 °C for 3 hours. The concentrations of reagents were 2.5, 5.0, 7.5, 10.0, 15.0 and 20.0 mM CTAC for FANC-1 to FANC-6, respectively, and 0.25, 0.50, 0.75, 1.0, 1.5 and 2.0 mM AgNO<sub>3</sub>, for FANC-1 to FANC-6, respectively. Please notice that the molar ratio between CTAC and AgNO<sub>3</sub> was maintained at 10. After incubation, the resulting solution was centrifuged at 7000 rpm (FANC-1 and FANC-2), 6000 rpm (FANC-3 and FANC-4) or 5000 rpm (FANC-5 and FANC-6) for 10 min and redispersed in deionized water.

We then analyzed the FANCs with TEM (Figure 2.5a) and UV-visible spectrometer (Figure 2.5b). As the amount of added Ag precursor increases, more dramatic spectroscopic changes have been observed. From FANC-1 to FANC-3, compared to AuNRs, broader transverse (510 nm) and longitudinal (765 nm) peak shapes were observed, and both peak intensities increased as a larger amount of Ag precursor was added (Figure 2.5b). From the

TEM images (Figure 2.5a), we can conclude the thicknesses of Ag shell for both longitudinal and transverse directions are quite similar. It is well known that AuNRs with an aspect ratio of 3~7 have [001] longitudinal growth direction and octagonal cross section enclosed by {100} and {110} facets, and at the end side, {110} and {111} facets are exposed at the truncated region.<sup>45</sup> At the early stages, thermodynamically driven conformal overgrowth occurred at the end and lateral regions of AuNR. When Ag growth step proceeded in CTAC capping agent, the epitaxial growth rates of {111} and {110} facets of AuNRs are faster than {100} facet.<sup>46,47</sup> As the Ag shell grows, Au-Ag core-shell particles gradually become enclosed by {100} facet of Ag, which would be tightly bound by CTAC. From FANC-3 to FANC-6, Ag shell has grown thicker to the transverse direction than longitudinal direction and the edges of FANCs are relatively sharp (Figure 2.5a). The end sides of the core-shell particles are believed to be enclosed by {100} facet faster than the lateral sides. We expect tightly bound CTAC on Ag surface interrupts shell growth, inducing the difference in the shell growth rate between transverse and longitudinal directions for FANC-3 to FANC-6. In the UV-visible spectra, four distinct plasmonic modes at 280 nm, 390 nm, 440 nm and 580 nm were observed, and these plasmon modes are similar to the results from other literatures.<sup>47-49</sup> The two highest-energy peaks are originated from the octupolar mode, and the lowest-energy peak and the second lowest-energy peak are ascribed to the longitudinal dipolar plasmon mode and transverse dipolar plasmon mode, respectively.<sup>50</sup> The presence of many of these plasmon modes in FANC nanostructures suggests the potential for fluorescence signal amplification at various wavelengths.

The detailed TEM analysis was performed using ImageJ software ([rsb.info.nih.gov/ij/](http://rsb.info.nih.gov/ij/); Figure 2.5c). For each FANC structure, >100 particles were analyzed. The transverse and longitudinal lengths of FANCs were increased from 12.8 nm to 36.1 nm and from 50.3 to 60.4 nm, respectively, indicating Ag shell thickness was more dominantly increased in the

transverse direction. The transverse and longitudinal shell thicknesses are 11.6 and 5.0 nm, respectively. The aspect ratio of FANCs was gradually decreased as the Ag shell became thicker (Figure 2.5c). We also checked the cuboid morphology of FANC-4 particles by a tilted SEM analysis (Figure 2.5d).

The direct contact of fluorophores with metal surface should be prevented to minimize fluorescence quenching caused by electron transfer, and thus, it will be helpful to theoretically explore the correlation between the distance/distribution of fluorophore dyes around nanoparticles and fluorescence signal intensity. In general, the persistence length (the criteria for the length that polymer chains can maintain a linearity) of a single-stranded oligonucleotide is estimated to be 1 nm or smaller,<sup>51,52</sup> but thiolated single-stranded oligonucleotides attached to nanoparticle surfaces can have fully or partly stretched conformation with a length close to the contour length (the maximum physically possible extension length of a polymer) of the single-stranded oligonucleotide.<sup>53-56</sup> In this experiment, a 6-subunit polyethylene glycol was placed between 10 and 15 nucleotide sequences (Figure 2.1 and Figure 2.6). By using values of 0.43 nm per base for oligonucleotides<sup>53,57</sup> and 0.28 nm per subunit for polyethylene glycol,<sup>58</sup> the contour length of the spacer oligonucleotide was estimated to be ~12.43 nm. According to the molecular dynamics simulation, the thiol linker group (-S(CH<sub>2</sub>)<sub>6</sub>-) does not contribute to the length of the oligonucleotide.<sup>54</sup> It should be noticed that the transverse shell thickness (11.6 nm) of a FANC-6 is similar to the theoretical contour length of Alexa Fluor<sup>TM</sup> 647-modified thiolated oligonucleotides while the longitudinal length of FANC-6 is shorter than the theoretical length of the fluorescent spacer oligonucleotide.

To further characterize the structural features of FANCs, we obtained the dark-field TEM image (Figure 2.5e) and elemental mapping images of FANC-4 (Figure 2.5f). The results show that, overall, AuNR core and Ag shell are well separated with little intermixing between Au and Ag atoms. The dark-field TEM image further confirms the formation of highly well-

defined cuboid structures with sharp Ag edges. In Figure 2.7, the high resolution TEM (HR-TEM) image and selected area electron diffraction (SAED) result is shown. The HR-TEM image displays a clear and continuous fringe, which has [001] lattice zone axis spacing of 2.0 Å and can be indexed as {200} of face-centered cubic (fcc) Ag. The corresponding SAED pattern showed square symmetry spots, confirming that the Ag shell is a single crystal enclosed by {100} facet. The clear fringes can be seen in the Ag shell edge area in the HR-TEM image representing its rectangular cross section bound by the {100} facet.

### **Fluorescence analysis of FANCs**

Next, the fluorescence intensities of the synthesized FANCs and were measured (Figure 2.8a). The integrated fluorescence intensity plot showed dramatic change of fluorescence intensity at different shell growth steps (Figure 2.8b). In order to calculate fluorescence enhancement factors, we treated Alexa Fluor<sup>TM</sup> 647-modified thiolated oligonucleotide-attached AuNRs and FANCs with potassium cyanide (KCN) to completely dissolve AuNPs and recover fluorophores by the chelation-mediated melting of Au and Ag particles. By comparing with the fluorescence intensity of free Alexa Fluor<sup>TM</sup> 647-modified thiolated oligonucleotides, we obtained the fluorescence enhancement factors (Figure 2.8c). The largest fluorescence enhancement factor was ~186 with the FANC-4 with 7.44 nm and 4.08 nm transverse and longitudinal Ag shell thicknesses, respectively. The fluorescence intensity was gradually decreased after FANC-4, mainly due to the quenching effect observed when the dyes are positioned too close to the Ag surface.

In order to examine the fluorescence signal amplification mechanism of the FANC system in detail, the theoretical enhancement factor values were calculated with the boundary-element method using the MNPBEM toolbox. To derive the theoretical enhancement factor, it was assumed that all the fluorophores are located at the same AuNR-fluorophore distance ( $d$ )

from the AuNR surface (Figure 2.9a) and the average value in the vertical surface space, in which the fluorophore is present, was evaluated (Figure 2.9b). From the prediction of the length of a single-stranded oligonucleotide used in the experiment, it was assumed that fluorophores can be distributed up to 12.43 nm (contour length) in the vertical direction on the AuNR surface. Thus, the distance ( $d$ ) between AuNR surface and a fluorophore was scanned from 7.0 nm to 12.5 nm, and the theoretical enhancement factors were calculated at 0.5 nm intervals for each FANC particle (Figure 2.9c). In the scanned  $d$  range, the EF value of FANC-4 was calculated as the highest EF value-generating structure, which is consistent with the experimental results, and the highest EF value appeared around  $d = 10$  nm. We compared the EF value of  $d = 10$  nm with the experimental data, and it was confirmed that the trend of the experimental value and the simulated value was largely coincided as a function of the FANC size (Figure 2.9d). In order to examine the mechanism of fluorescence signal amplification in the FANC system more closely, we constructed the 3-dimensional EF map at  $d = 10$  nm (Figure 2.9e). Through the 3-dimensional EF maps, it can be explicitly revealed that the points with high EFs are distributed for FANC-4 and other FANCs. The EF maps show that the fluorophores located in the longitudinal direction rather than in the transverse direction are more involved in signal amplification, and the region with the largest EF values was distributed in the vertex region of the cuboid. The maximum EF value of  $\sim 370$  was derived in the case of FANC-4. When the particle size gets larger than FANC-4 by forming thicker Ag shells, the fluorophores in the vertex area more quickly approach or contact the Ag surface than other regions, resulting in fluorescence signal quenching.

In PEF study, although it is considered that local EM field enhancement is the most important factor in determining fluorescence amplification efficiency,<sup>11-16</sup> many other factors such as plasmon coupling effect mediated by a non-radiative interaction,<sup>33,51,59</sup> radiative decay change in PEF,<sup>14-16,40</sup> and scattering profile<sup>14-16</sup> of plasmon nanostructures also affect the

fluorescence signal enhancement. When the Ag shell thickness varies in the FANC nanostructures, not only the distance between fluorophore and plasmonic particle surface but also plasmon modes should be considered simultaneously because the overall morphology and dimension of the FANCs are also changed, which means the electromagnetic field intensity and distribution are also altered. The thickness of the Ag shell and the length of the DNA serve as two main tunable parameters that allow for precisely controlling the distance between a fluorophore and metal particle surface. By complementarily adjusting these two main parameters with a precise synthetic handle, the most effective amplification conditions can be pinpointed in our PEF system.

### **Fluorescence silica shell formation**

To increase chemical and optical stability and further add fluorophore dyes per particle, we coated FANCs with fluorescent silica shells. For silica shell formation, we first synthesized PVP-coated FANC-4 structures, which are highly stable in EtOH solvent. We then formed fluorescent silica shells on FANC-4 particles using the Stöber method with slight modifications. We confirmed the formation of fluorescent silica shell-coated FANCs (FS-FANCs) by TEM analysis (Figure 2.10a and Figure 2.11). The size of FS-FANCs is ~150 nm, and importantly, each silica shell contained only one FS-FANC in most cases. We also checked fluorescence signal stability of FS-FANCs in PBS buffer solution with various salt concentrations. By measuring fluorescent activities of FANCs and FS-FANCs in PBS buffer, we found that FS-FANCs have highly improved stability in buffer solution compared to FANCs (Figure 2.10b).

To compare the fluorescence signal contributions by the PEF and silica-embedded fluorophore dyes, we also prepared fluorescent silica-coated core-shell nanocuboids (FS-NCs), without fluorophore-modified DNAs. We found that ~464 fluorophores were embedded in a

single FS-NC while a single FS-FANC contained 928 fluorophores (~464 thiolated fluorescent DNA strands per particle). When measured at the same particle concentration, the fluorescence intensity of FS-NCs was only 27.2% of the fluorescence intensity of FS-FANCs (Figure 2.10c). Consequently, the enhancement factors of FS-NCs and FS-FANCs are 70.5 and 185.6, respectively (Figure 2.10d), suggesting a large contribution of fluorescence amplification comes from the PEF.

### **Microarray-based miRNA detection assay**

Finally, we applied FS-FANCs to a microarray-based miRNA detection assay (Figure 2.12). For this application, miRNA-134 was used as a target, and is known as a brain-specific biomarker that regulates the dendritic spine development.<sup>60</sup> First, the amine-labeled probe DNA (Table S1), complementary to the target miRNA, was arrayed on an N-hydroxysuccinimide (NHS) dendron glass slide (spot size: ~80 nm in diameter). Subsequently, the target miRNA (1 pM – 100 aM) was hybridized with the probe DNA. For quantifying the formed miRNA/DNA hybrids, mouse monoclonal antibody S9.6 that binds to the hybrid in a sequence-independent manner ( $K_d = 1.2 \times 10^{-11}$  M) was allowed to bind to the hybrid,<sup>61,62</sup> and the FS-FANC-4-tethered goat anti-mouse secondary antibody was introduced subsequently.

The assay was run in PBS buffer (0.2 M NaCl), and the array was imaged with a fluorescence scanner in a dried state. The consistent fluorescence signals from the microarray spots show that the PEF activity of FS-FANCs remains stable even at a relatively high salt concentration and in a dried condition. On this microarray platform, 100 aM miRNA target can be detected, but considering the error bars, the reliable limit of detection (LOD) with secondary antibody-tethered FS-FANCs is 1 fM (40 zmol) (Figure 2.13). The miRNA target was quantitatively detected from 1 pM to 1 fM with FS-FANC-4 probes in a reliable manner (Figure 2.13b). Compared to other antibody-based small RNA detection on a microarray platform, the

sensitivity is improved >1000 folds.<sup>62</sup> In addition, the fluorescence signal of 1.0 pM spots was tracked for two weeks to check the temporal stability of FS-FANCs, and it was confirmed that the intensity was maintained during the term (Figure 2.14). We also performed the microarray-based miRNA detection using FS-NCs and a conventional fluorescence label (Cy<sup>TM</sup>5) with S9.6 antibody. The LOD for the assay with FS-NCs was 10 fM (0.4 amol), and the fluorescence signal intensity was only 39% of that with FS-FANC-4 labels at the same miRNA target concentration (Figure 2.15). We also performed the microarray-based miRNA detection assay using a conventional fluorescence label (Cy<sup>TM</sup>5) and S9.6 antibody, and the LOD for the assay was 1.0 pM (0.25 fmol), which matches well with the literature result (Figure 2.16).<sup>62</sup> In this conventional assay without using FANCs, the microarray spots from 1 pM to 10 fM could not be differentiated. When the fluorescence signal intensities of the microarrayed spots with FANC-4 labels and commercial fluorescence labels (Cy<sup>TM</sup>5) were compared at the same miRNA target concentration (1 pM), there was a significant signal intensity gap between these two (Figure 2.16c). To rigorously analyze and validate our assay results, the atomic force microscopy (AFM) was used to obtain the total area of the surface-captured nanoparticles per microarray spot for each target concentration (Figure 2.13c and Figure 2.17). There is a high correlation between fluorescence- and AFM-based nanoparticle imaging results with respect to both detection limit and dynamic range, and this further validates the reliability and robustness of FS-FANC-4 probes for biosensing applications.

## 2.4. Conclusions

We developed the DNA sequence and plasmonic nanoshell-engineering strategy with AuNRs to form ultraflat-faceted FANC structures and find the optimal Ag nanoshell thickness to reliably maximize PEF signals with these structures. With the optimized FANC structure (FANC-4), fluorescence signal was enhanced by ~186 folds. Computational modeling results with FANCs matched well with the experimental results, and show that our synthetic approach works well and the vertex and vertex-neighboring areas of the FANC-4 structure are mainly responsible for the strong EM-field generation and corresponding fluorescence enhancement. Furthermore, we incorporated more fluorophore dyes into particles to further increase fluorescence signal intensity per particle, fixed the distances between fluorophore dyes and flat silver shells, and stabilized FANC particles by forming fluorescent silica shells on the FANCs. Importantly, we achieved a high sensitivity ( $>10^3$ -fold higher than conventional fluorophore dye-based miRNA assays) in the microarray-based miRNA detection scheme with a dynamic range from 100 aM to 1 pM. The reliability of the fluorescence assay results was further confirmed by the AFM image analysis on the assayed microarray spots. The strategy and results shown here with FANCs offer the reliable designing principle and synthetic method for PEF probes and open the revenues for practical use of PEF probes for more sensitive and more reliable biosensing applications.

## 2.5. References

- [1] V. Giannini, A. I. Fernández-Domínguez, S. C. Heck, S. A. Maier, *Chem. Rev.* **2011**, *111*, 3888-3912.
- [2] M. S. Tame, K. R. McEnery, Ş. K. Özdemir, J. Lee, S. A. Maier, M. S. Kim, *Nat. Phys.* **2013**, *9*, 329-340.
- [3] S. Kruk, Y. Kivshar, *ACS Photonics*. **2017**, *4*, 2638-2649.
- [4] N. Meinzer, W. L. Barnes, I. R. Hooper, *Nat. Photonics*. **2014**, *8*, 889-898.
- [5] M. Moskovits, *Rev. Mod. Phys.* **1985**, *57*, 783-826.
- [6] K. Kneipp, Y. Wang, H. Kneipp, L. T. Perelman, I. Itzkan, R. R. Dasari, S. Michael, *Phys. Rev. Lett.* **1997**, *78*, 1667-1670.
- [7] Y. C. Cao, R. Jin, C. A. Mirkin, *Science* **2002**, *297*, 1536-1540.
- [8] D.-K. Lim, K.-S. Jeon, H. M. Kim, J.-M. Nam, Y. D. Suh, *Nat. Mater.* **2010**, *9*, 60-67.
- [9] D.-K. Lim, K.-S. Jeon, J.-H. Hwang, H. Kim, S. Kwon, Y. D. Suh, J.-M. Nam, *Nat. Nanotechnol.* **2011**, *6*, 452-460.
- [10] J. Langer, D. Jimenez de Aberasturi, J. Aizpurua, R. A. Alvarez-Puebla, B. Auguie, J. J. Baumberg, G. C. Bazan, S. E. J. Bell, A. Boisen, A. G. Brolo, J. Choo, D. Cialla-May, V. Deckert, L. Fabris, K. Faulds, F. J. García de Abajo, R. Goodacre, D. Graham, A. J. Haes, C. L. Haynes, C. Huck, T. Itoh, M. Käll, J. Kneipp, N. A. Kotove, H. Kuang, E. C. Le Ru, H. K. Lee, J.-F. Li, X. Y. Ling, S. A. Maier, T. Mayerhöfer, M. Moskovits, K. Murakoshi, J.-M. Nam, S. Nie, Y. Ozaki, I. Pastoriza-Santos, J. Perez-Juste, J. Popp, A. Pucci, S. Reich, B. Ren, G. C. Schatz, R. P. Van Duyne, T. Vo-Dinh, Y. Wang, K. A. Willets, C. Xu, H. Xu, Y. Xu, Y. S. Yamamoto, B. Zhao, L. M. Liz-Marzán, *ACS Nano* **2020**, *14*, 28-117.
- [11] C. D. Geddes, J. R. Lakowicz, *J. Fluoresc.* **2002**, *12*, 121-129.

- [12] E. For; S. Grésillon, Surface Enhanced Fluorescence. *J. Phys. D: Appl. Phys.* **2008**, *41*, 013001.
- [13] J. R. Lakowicz, K. Ray, M. Chowdhury, H. Szmackinski, Y. Fu, J. Zhang, K. Nowaczyk, *Analyst* **2008**, *133*, 1308-1346.
- [14] T. Ming, H. Chen, R. Jiang, J. Wang, *J. Phys. Chem. Lett.* **2012**, *3*, 191-202.
- [15] J. Dong, Z. Zhang, H. Zheng, M. Sun, *Nanophotonics* **2015**, *4*, 472-490.
- [16] J.-F. Li, C.-Y. Li, R. F. Aroca, *Chem. Soc. Rev.* **2017**, *46*, 3962-3979.
- [17] P. Anger, P. Bharadwaj, L. Novotny, *Phys. Rev. Lett.* **2006**, *96*, 113002.
- [18] H. Mishra, B. L. Mali, J. Karolin, A. I. Dragan, C. D. Geddes, *Phys. Chem. Chem. Phys.* **2013**, *15*, 19538-19544.
- [19] A. I. Dragan, E. S. Bishop, J. R. Casas-Finet, R. J. Strouse, J. McGivney, M. A. Schenerman, C. D. Geddes, *Plasmonics* **2012**, *7*, 739-744.
- [20] G. P. Acuna, F. M. Möller, P. Holzmeister, S. Beater, B. Lalkens, P. Tinnefeld, *Science* **2012**, *338*, 506-510.
- [21] H. Yuan, S. Khatua, P. Zijlstra, M. Yorulmaz, M. Orrit, *Angew. Chem. Int. Ed.* **2013**, *52*, 1217-1221.
- [22] L. Su, H. Yuan, G. Lu, S. Rocha, M. Orrit, J. Hofkens, H. Uji-i, *ACS Nano* **2016**, *10*, 2455-2466.
- [23] R. Gill, E. C. Le Ru, *Phys. Chem. Chem. Phys.* **2011**, *13*, 16366-16372.
- [24] A. Kinkhabwala, Z. Yu, S. Fan, Y. Avlasevich, K. Müllen, W. E. Moerner, *Nat. Photonics* **2009**, *3* 654-657.
- [25] L. Zhou, F. Ding, H. Chen, W. Ding, W. Zhang, S. Y. Chou, *Anal. Chem.* **2012**, *84*, 4489-4495.
- [26] W. Zhang, F. Ding, W.-D. Li, Y. Wang, J. Hu, S. Y. Chou, *Nanotechnology* **2012**, *23*, 225301.

- [27] M. D. Furtaw, J. P. Anderson, L. R. Middelndorf, G. R. Bashford, *Plasmonics* **2014**, *9*, 27-34.
- [28] T. Ming, L. Zhao, Z. Yang, H. Chen, L. Sun, J. Wang, C. Fan, *Nano Lett.* **2009**, *9*, 3896-3903.
- [29] R. Bardhan, N. K. Grady, J. R. Cole, A. Joshi, N. J. Halas, *ACS Nano* **2009**, *3*, 744-752.
- [30] A. Bek, R. Jansen, M. Ringler, S. Mayilo, T. A. Klar, J. Feldmann, *Nano Lett.* **2008**, *8*, 485-490.
- [31] J. Zhang, Yi, M. H. Chowdhury, J. R. Lakowicz, *Nano Lett.* **2007**, *7*, 2101-2107.
- [32] M. R. Gartia, J. P. Eichorst, R. M. Clegg, G. L. Liu, *Appl. Phys. Lett.* **2012**, *101*, 023118.
- [33] N. S. Abadeer, M. R. Brennan, W. L. Wilson, C. J. Murphy, *ACS Nano* **2014**, *8*, 8392-8406.
- [34] P. P. Pompa, L. Martiradonna, A. D. Torre, F. D. Sala, L. Manna, M. D. Vittorio, F. Calabi, R. Cingolani, R. Rinaldi, *Nat. Nanotechnol.* **2006**, *1*, 126-130.
- [35] C. Ayala-Orozco, J. G. Liu, M. W. Knight, Y. Wang, J. K. Day, P. Nordlander, N. J. Halas, *Nano Lett.* **2014**, *14*, 2926-2933.
- [36] A. R. Guerrero, R. F. Aroca, *Angew. Chem. Int. Ed.* **2011**, *50*, 665-668.
- [37] J. Asselin, P. Legros, A. Grègoire, D. Boudreau, *Plasmonics* **2016**, *11*, 1369-1376.
- [38] J. Zhang, Fu, Yi, M. H. Chowdhury, J. R. Lakowicz, *Nano Lett.* **2007**, *7*, 2101-2107.
- [39] I. O. Osorio-Román, A. R. Guerrero, P. Albella, R. F. Aroca, *Anal. Chem.* **2014**, *86*, 10246-1251.
- [40] Y. Jeong, Y.-M. Kook, K. Lee, W.-G. Koh, *Biosens. Bioelectron.* **2018**, *111*, 102-116.
- [41] N. Bushati, S. M. Cohen, *Annu. Rev. Cell Dev. Biol.* **2007**, *23*, 175-205
- [42] Y. Cheng, L. Dong, J. Zhang, Y. Zhao, Z. Li, *Analyst* **2018**, *143*, 1758-1774.
- [43] G. Gines, R. Menezes, W. Xiao, Y. Rondelez, V. Taly, *Mol. Aspects Med.* **2020**, *72*, 100832

- [44] B. Nikoobakht, M. A. El-Sayed, *Chem. Mater.* **2013**, *15*, 1957-1962.
- [45] Z. L. Wang, M. B. Mohamed, S. Link, M. A. El-Sayed. *Surf. Sci.* **1999**, *440*, L809.
- [46] Y. Ma, W. Li, E. C. Cho, Z. Li, T. Yu, J. Zeng, Z. Xie, Y. Xia, *ACS Nano* **2010**, *4*, 6725
- [47] K. Park, L. F. Drummy, R. A. Vaia. *J. Mater. Chem.* **2011**, *21*, 15608
- [48] R. Jiang, H. Chen, L. Shao, Q. Li, J. Wang, *Adv. Mater.* **2012**, *24*, OP200-OP207.
- [49] B. N. Khlebtsov, Z. Liu, J. Ye, N. G. Khlebtsov, *J. Quant. Spectrosc. Ra.* **2015**, *167*, 64-75.
- [50] Y. Chen, K. Munechika, D. S. Ginger, *Nano Lett.* **2007**, *7*, 690-696.
- [51] S. B. Smith, Y. Cui, C. Bustamante, *Science* **1996**, *271*, 795-799.
- [52] J. B. Mills, E. Vacano, P. J. Hagerman, *J. Mol. Biol.* **1999**, *285*, 245-257.
- [53] W. J. Parak, T. Pellegrino, C. M. Micheel, D. Gerion, S. C. Williams, A. P. Alivisatos, *Nano Lett.* **2003**, *3*, 33-36.
- [54] O.-S. Lee, G. C. Schatz, *J. Phys. Chem. C.* **2009**, *113*, 2316-2321.
- [55] A. Singh, H. Eksiri, Y. G. Yingling, *J. Polym. Sci., Part B: Polym. Phys.* **2011**, *49*, 1563-1568.
- [56] J. M. Carnerero, A. Jimenez-Ruiz, P. M. Castillo, R. Prado-Gotor, *ChemPhysChem* **2017**, *18*, 17-33.
- [57] B. Tinland, A. Pluen, J. Sturm, G. Weill, *Macromolecules* **1997**, *30*, 5763-5765.
- [58] F. Oesterhelt, M. Rief,; H. E. Gaub, *New Journal of Physics* **1999**, *1*, 6.1-6.11.
- [59] K. Aslan, Z. Leonenko, J. R. Lakowicz, C. D. Geddes, *J. Fluoresc.* **2005**, *15*, 643-654.
- [60] R. Fiore, S. Khudayberdiev, M. Christensen, G. Siegel, S. W. Flavell, T.-K. Kim, M. E. Greenberg, Schratt, *EMBO J.* **2009**, *28*, 697-710.
- [61] S. J. Boguslawski, D. E. Smith, M. A. Michalak, K. E. Mickelson, C. O. Yehle, W. L. Patterson, R. J. Carrico, *J. Immunol. Methods* **1986**, *89*, 123-130.

- [62] Z. Hu, A. Zhang, G. Storz, S. Gottesman, S. H. Leppla, *Nucleic Acids Res.* **2006**, *34*, e52.
- [63] A. H. Alhasan, D. Y. Kim, W. L. Daniel, E. Watson, J. J. Meeks, C. S. Thaxton, C. A. Mirkin, *Anal. Chem.* **2012**, *84*, 4153-4160.
- [64] T. Ueno, T. Funatsu, *PLoS One* **2014**, *9*, e90920.

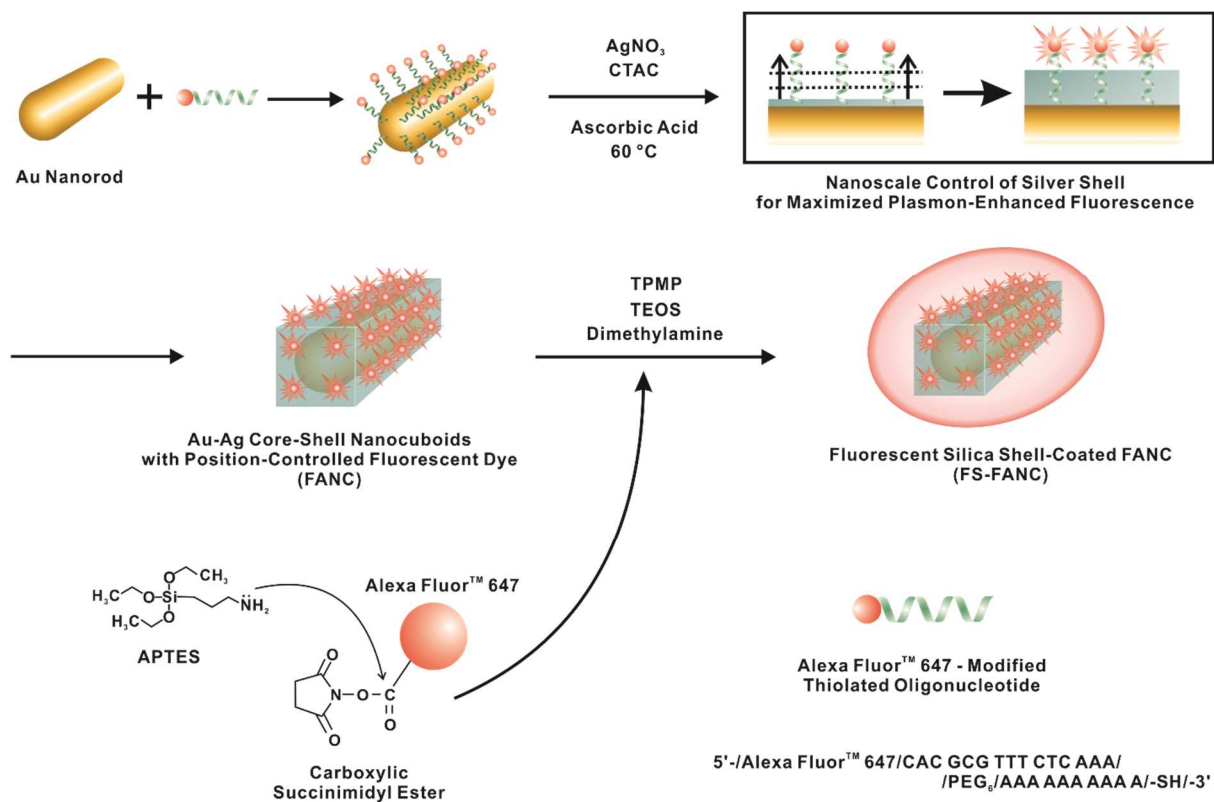
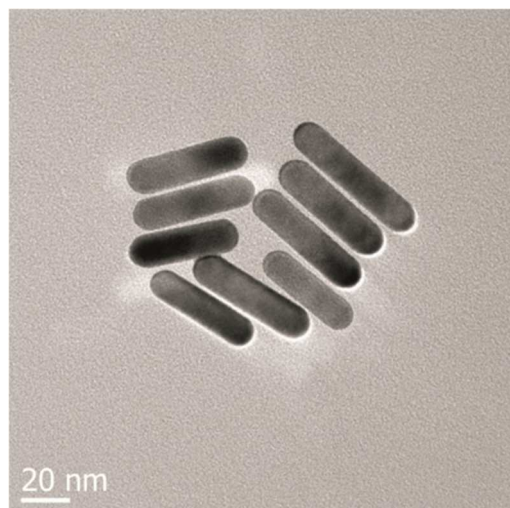


**Figure 2.1.** Schematic illustration of synthetic pathway for fluorescence-amplified nanocuboid (FANC) and fluorescent silica shell-coated FANC (FS-FANC) for maximized plasmon-enhanced fluorescence (PEF).



Dimension (nm)	50.32(4.26) x 12.81(0.94)
Aspect ratio	3.95(0.42)
Transverse mode (nm)	510
Transverse mode (nm)	765
$\epsilon_{520\text{nm}}$ ( $\text{M}^{-1}\text{cm}^{-1}$ )	$1.374 \times 10^9$

**Figure 2.2.** TEM image, dimensions and optical properties of the synthesized AuNRs. The AuNRs were analyzed by UV-visible spectroscopy, TEM and ICP-AES.

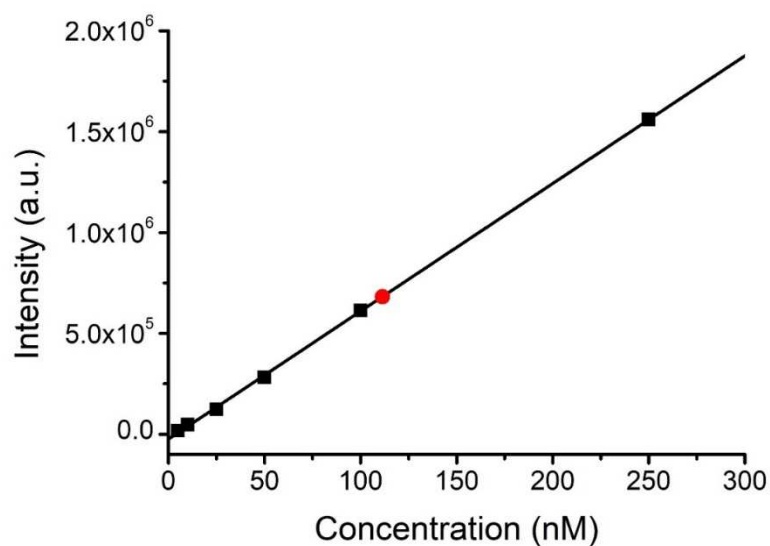


**Figure 2.3.** Quantification of the number of Alexa 647<sup>TM</sup> oligonucleotides on AuNR surface. The red dot represents the average fluorescence intensity of Alexa Fluor<sup>TM</sup>-modified thiolated oligonucleotides released from 0.24 nM AuNR solution treated with KCN solution. By comparing the average intensity with the standard curve of free Alexa Fluor<sup>TM</sup> 647-modified oligonucleotides, the average concentration of oligonucleotides attached on 0.24 nM AuNRs was calculated. The calculated average concentration of oligonucleotides was 111.4 nM, and ~464 Alexa Fluor<sup>TM</sup> 647-modified thiolated oligonucleotides were attached per AuNR.

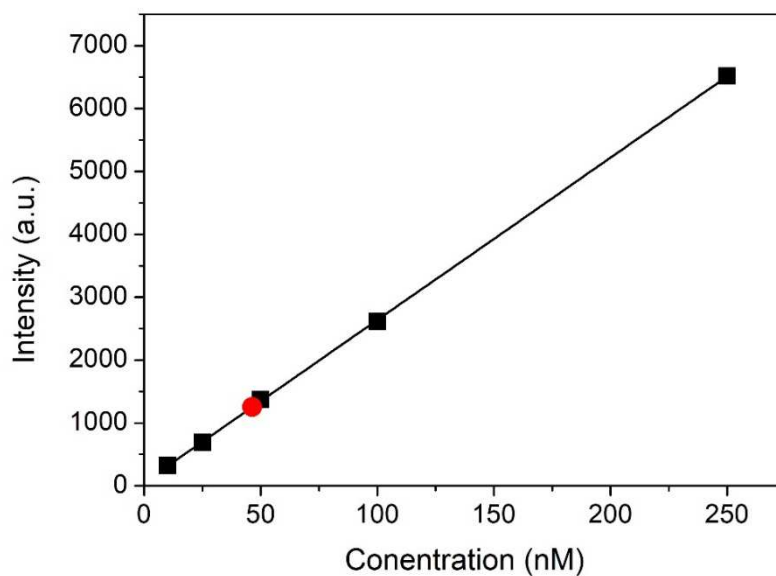


**Figure 2.4.** Quantification of incorporated Alexa Fluor<sup>TM</sup> 647 fluorophores in the silica shell of FS-NC. The red dot represents the average fluorescence intensity of Alexa Fluor<sup>TM</sup> 647 dyes released from the 0.1 nM FS-NC solution treated with KCN solution. By comparing the average intensity with the fluorescence standard curve of free Alexa Fluor<sup>TM</sup> 647 fluorophores, the average concentration of fluorophores embedded in silica shell of FS-NCs was calculated. The calculated average concentration of fluorophores was 43.4 nM, and ~463.8 Alexa Fluor<sup>TM</sup> fluorophores were embedded in a silica shell.

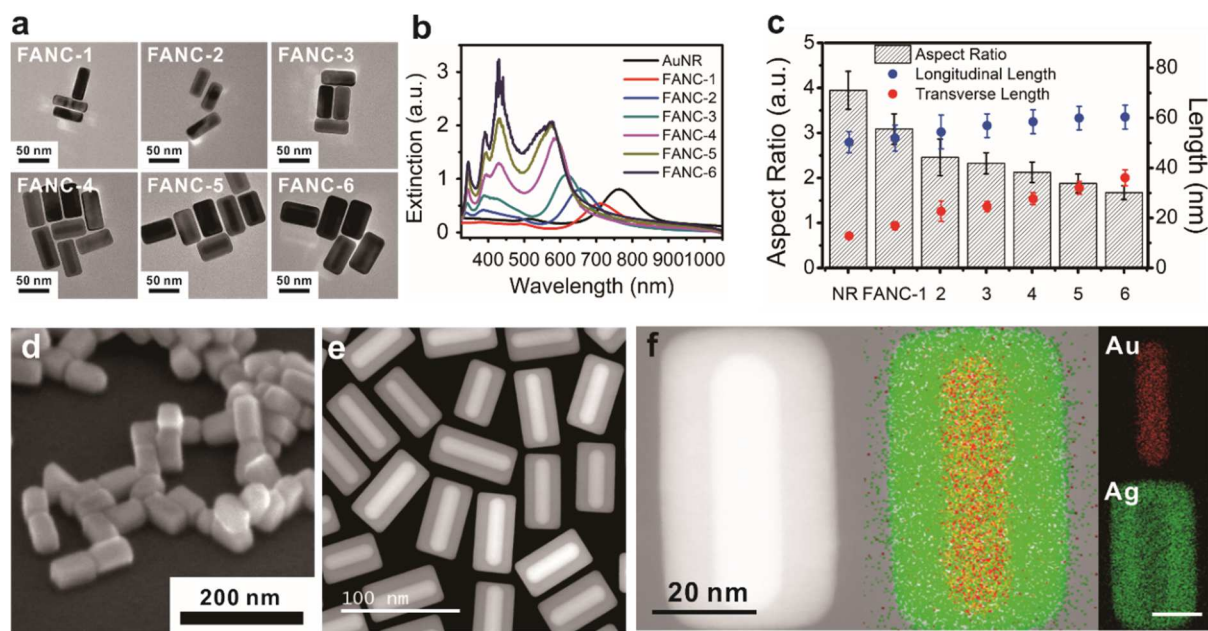


**Figure 2.5.** Characterization of FANCs. The TEM images (a) and UV-visible spectra (b), and TEM image-based statistical analysis of FANCs. The SEM image (d), dark-field TEM image (e), and EDS mapping of FANC-4 (f). The concentrations of nanoparticles in (b) are 0.18 nM for AuNR and 0.06 nM for FANCs, respectively.

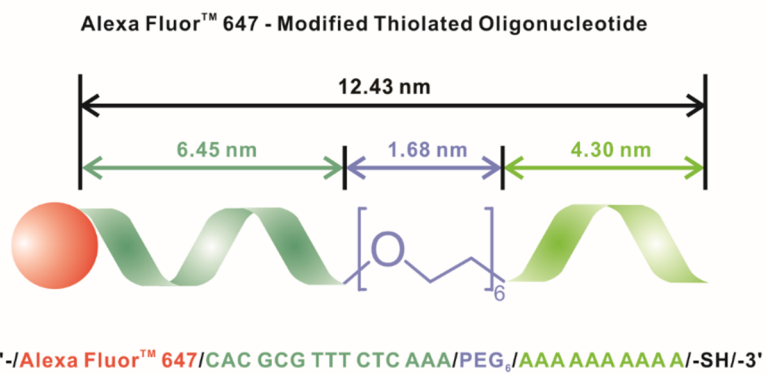


**Figure 2.6.** Fluorescent oligonucleotide design for FANCs.

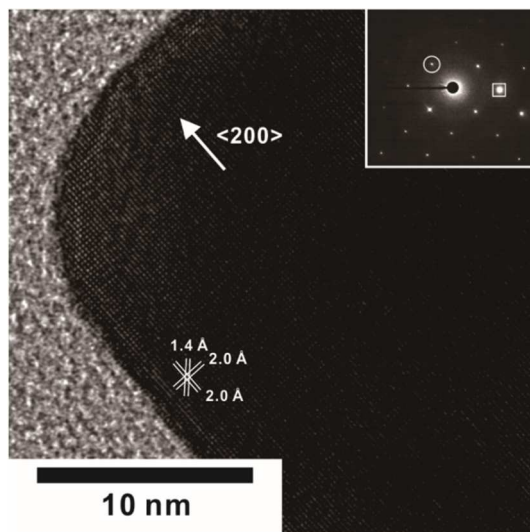


**Figure 2.7.** TEM image, dimensions and optical properties of the synthesized AuNRs. The AuNRs were analyzed by UV-visible spectroscopy, TEM and ICP-AE□

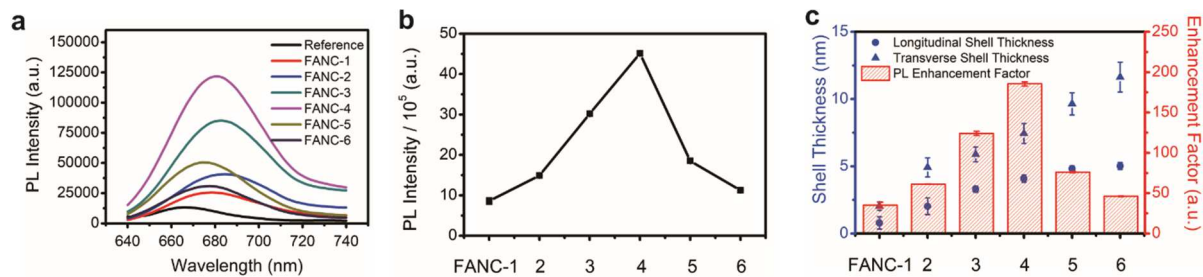


**Figure 2.8.** Fluorescence measurements of FANCs. The fluorescent spectra (a), integrated PL intensity (b), and shell thickness-dependent enhancement factor plot of FANCs (c).

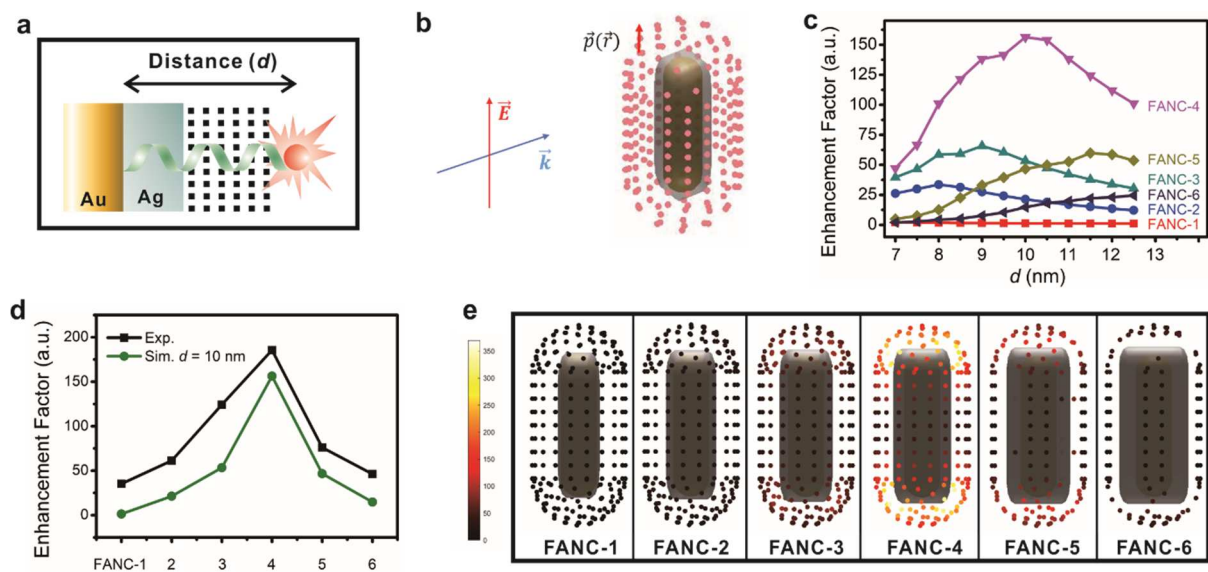


**Figure 2.9.** Theoretical modeling of FANCs. The definition of  $d$  (a) used in simulation, simulation scheme (b), enhancement factor (EF) simulation according to  $d$  (c), comparison of experimental and simulated EF values at  $d = 10$  nm (d), and EF maps of FANCs (e).

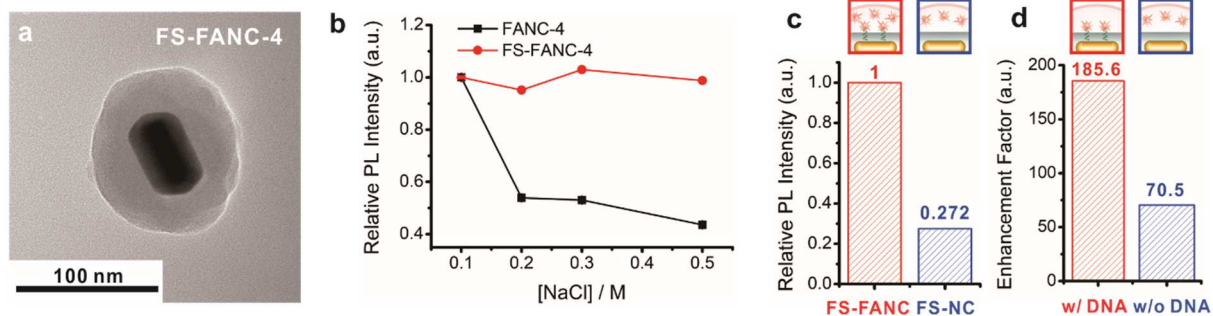


**Figure 2.10.** Formation of FS-FANC and fluorescence measurement. The TEM image of FS-FANC-4 (a), and fluorescence stability test of FANC-4 and FS-FANC-4 (b). The comparison of fluorescence activity between FS-FANC and FS-NC (c) and the comparison of enhancement factor between precisely controlled and randomly distributed fluorophores (d).

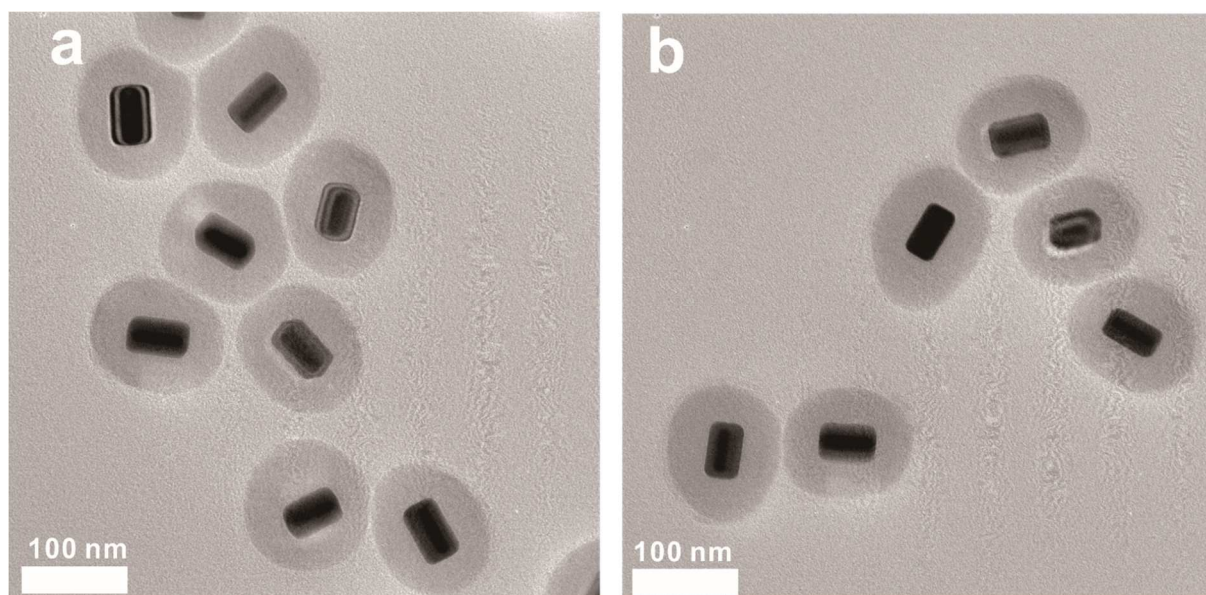


**Figure 2.11.** TEM images of F-FANCs (a) and F-NCs (b).

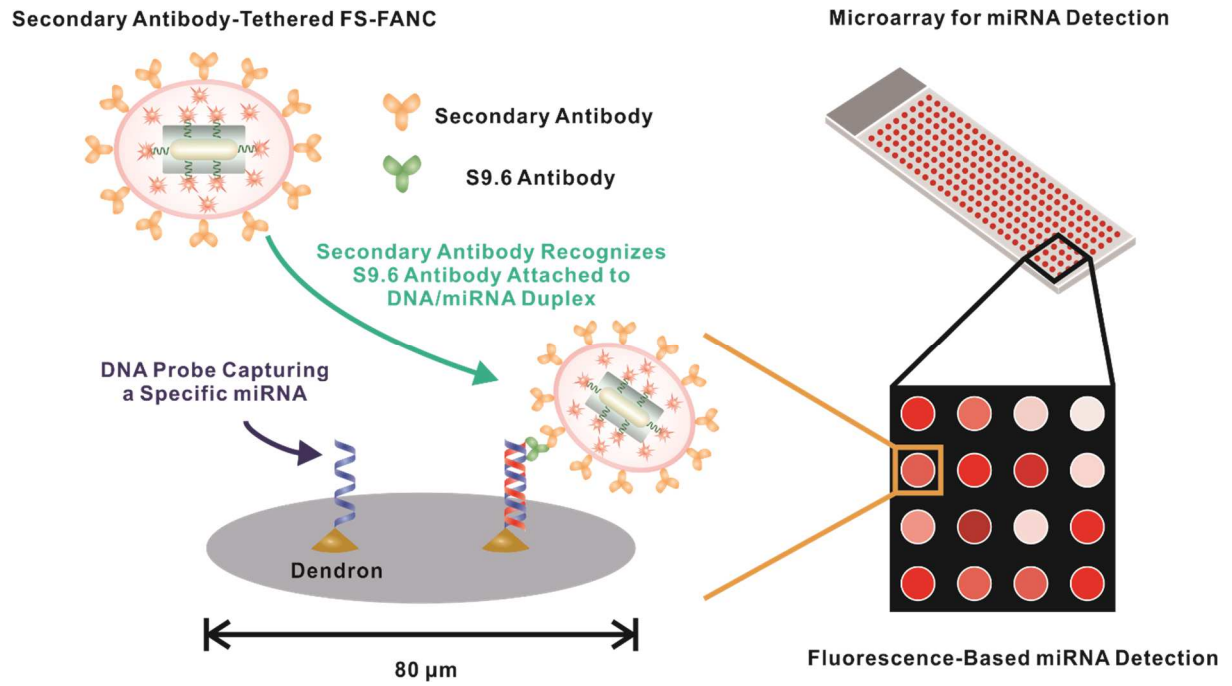


**Figure 2.12.** Schematic illustration of microarray-based miRNA detection using FS-FANCs.

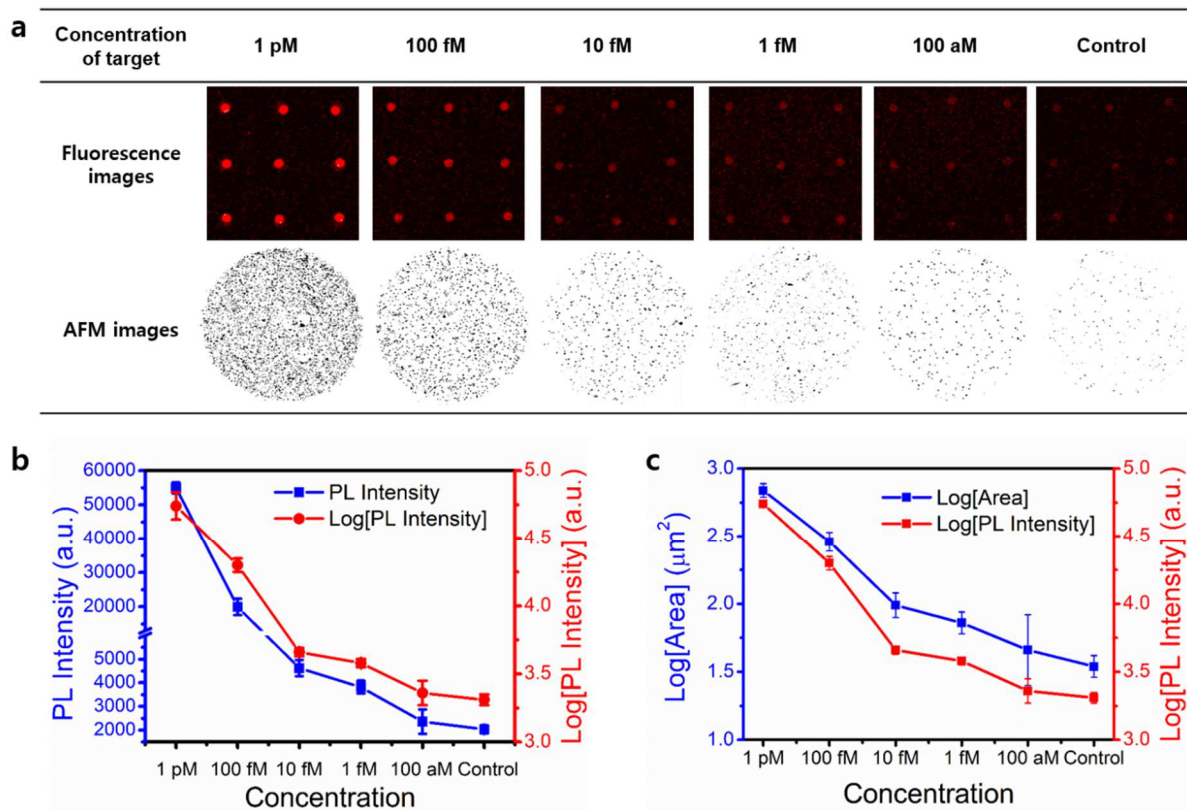


**Figure 2.13.** Microarray-based miRNA detection results using FS-FANCs. The fluorescence image-based microarray assay results (top row) and AFM image-based nanoparticle area tracking analysis (bottom row) (a). FS-FANC-4-based miRNA detection results (b). The correlation between FS-FANC-4 assay and particle-covered area results. Each data point and error bar in b and c was obtained from 9 microarray spots (c).

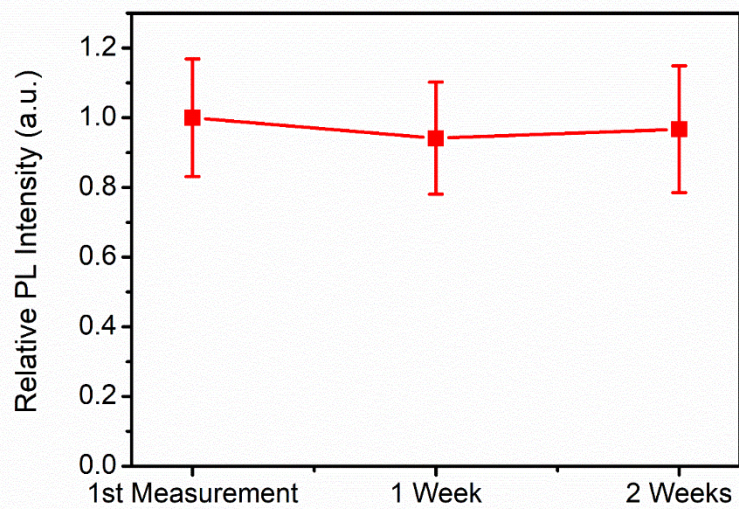


**Figure 2.14.** The long term stability of fluorescence signal of microarray spot. The fluorescence intensity of 1.0 pM spots was maintained for two weeks.

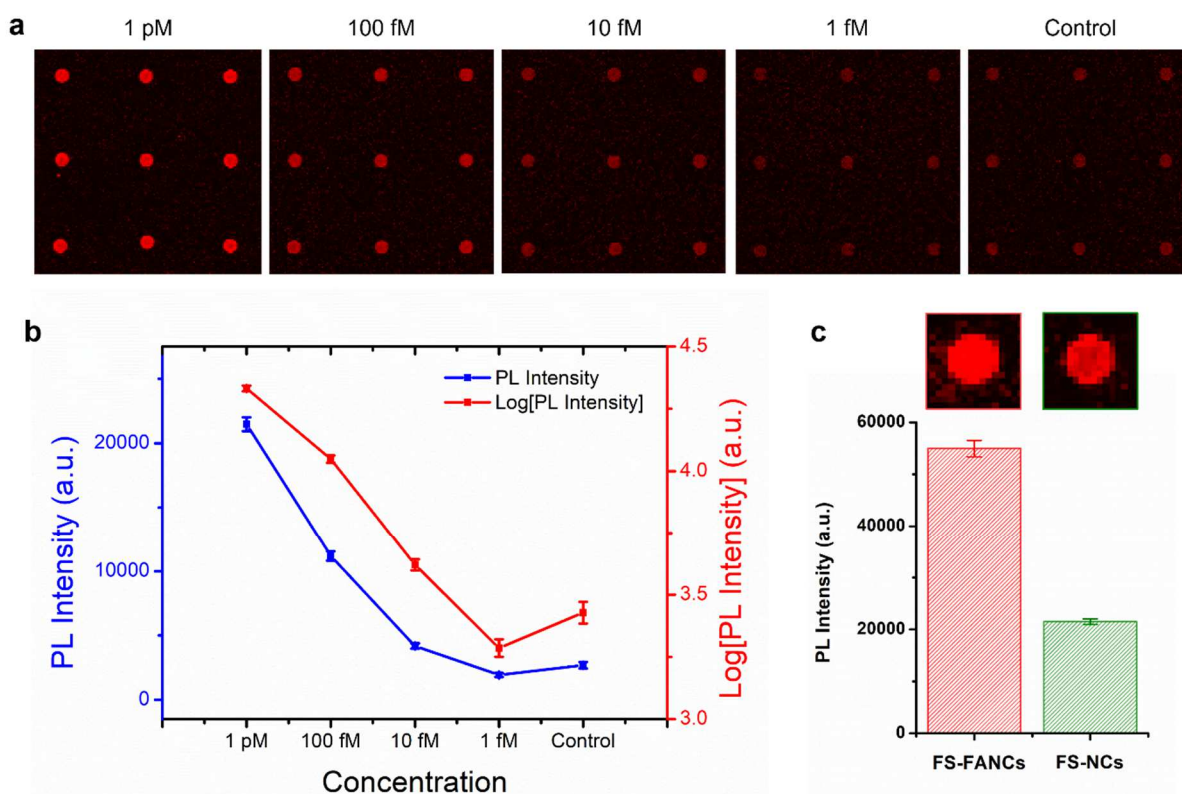


**Figure 2.15.** Microarray-based miRNA assay with FQ-NCs. The fluorescence images (a) and fluorescence intensity plots (b) with varying target miRNA-134 concentrations. Comparison of the fluorescence signal intensities between FQ-FANCs and FQ-NCs with 1.0 pM target miRNA-134 concentration (c). Each data point in (b) was obtained from 9 spots, and the error bars represent standard deviations. Anti-mouse IgG-modified FQ-NCs were used in the assay.

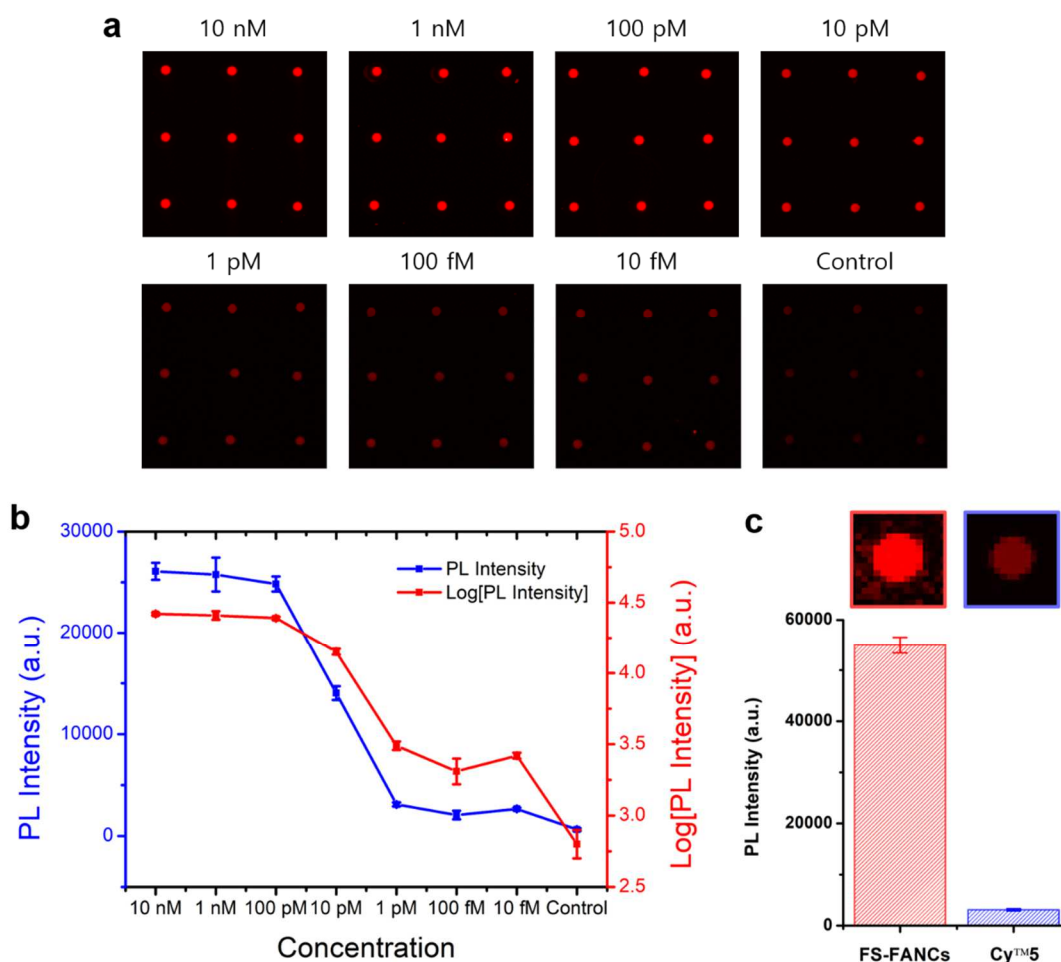


**Figure 2.16.** Microarray-based miRNA assay results with conventional fluorescence labels (Cy<sup>TM</sup>5) and F $\square$ -FANCs. The fluorescence images (a) and fluorescence intensity plots (b) with varying target miRNA-134 concentrations. (c) The comparison of the fluorescence signal intensities between F $\square$ -FANC and Cy<sup>TM</sup>5 labels with 1 pM target miRNA-134 concentration. Each data point in (b) was obtained from 9 spots, and the error bars represent standard deviations. Cy<sup>TM</sup>5-labeled goat anti-mouse IgG and anti-mouse IgG-modified F $\square$ -FANCs were used in the assays.

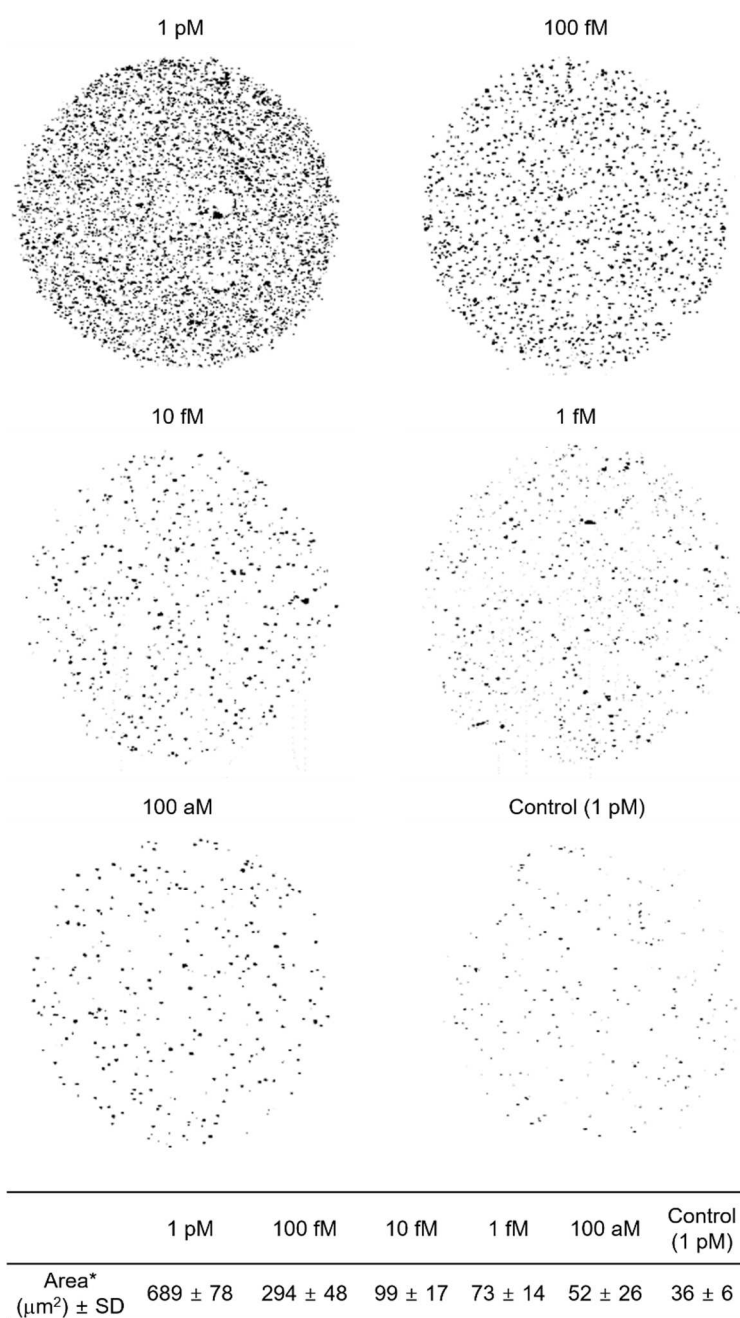


**Figure 2.17.** Representative AFM images and the averaged area values at each concentration. Nine spots at each concentration were imaged with AFM. \*The average value from 9 images for each case. SD represents standard deviation.

## **Chapter 3**

### **High Yield Synthesis of Multilayered Alternative Nanoplasmonic- Nanodielectric Amplifiers (MANNAs) for Broad Wavelength Range Plasmon-Enhanced Fluorescence**

### 3.1. Introduction

For practical fluorescence utilizations, signal enhancement over broad wavelength range is highly required because the regions of emission wavelengths used in various types of applications are different.<sup>1-3</sup> Plasmon-Enhanced Fluorescence (PEF) is a powerful tool to amplify fluorescence signals, and although numerous studies have been conducted, it is rare that a fluorescence signal of a wide emission wavelength range is effectively augmented through a single platform.<sup>4-8</sup> For broad range fluorescence enhancements, PEF-active nanostructures must have an enhanced electric field over a wide range of wavelengths, and at the same time, the fluorophores must be located in a space where the electric field is strongly concentrated, avoiding the quenching phenomenon.<sup>9-11</sup>

Multilayered alternative nanoplasmonic-nanodielectric nanostructures with a built-in dielectric nanogap have emerged as a promising platform for optical signal amplification.<sup>12-16</sup> In plasmonics, dielectric nanogap between plasmonic nanosurfaces plays a significant role in generating enormously amplified optical signals by effectively focusing electric field in a confined space.<sup>16,17</sup> The optically activated nanogap regions located in a plasmonic cavity between a metallic core and a metallic shell in multilayered alternative nanoplasmonic-nanodielectric nanostructures remain structurally stable because it is filled with dielectric material in it.<sup>14,18</sup> In particular, it effectively controls the dissipation of the optical signal through charge transfer that occurs when the optical reporter directly contacts the plasmonic surface. Furthermore, LSPR wavelengths can be adjusted in a wide spectral range through dimension control of each layer.<sup>15,19</sup>

Several studies have been conducted to increase optical signals using multilayer nanostructures by placing the optical reporters in the dielectric nanogap, and most of them were about SERS.<sup>18,20,21</sup> In the case of SERS, the distance range between the reporter and the metal surface where the fatal signal loss occurs is relatively smaller compared to PEF.<sup>22,23</sup> Also, it is

generally easier for SERS to observe the PEF phenomenon experimentally because the Raman enhancement factor is proportional to the second power of the local field ( $|E|^4$ ), whereas the Raman enhancement factor is proportional to the fourth power of the local field ( $|E|^4$ ).<sup>24</sup> The performance of Ag nanocrystals in enhancing Raman and fluorescence signals has been generally found to be better than Au nanocrystals, Ag has been preferred as an amplification material in PEF studies where it is more difficult to measure signal amplification.<sup>25</sup> N. Halas and coworkers presented a representative example of fluorescence enhancement using Au-based multilayer nanostructures.<sup>14</sup> They fabricated Au nanomatryoshka structures embedding NIR fluorophores in the inner dielectric layer and confirmed fluorescence enhancement process with agreement with theoretical calculation. However, the fluorescence enhancement factor of Au matryoshka nanostructures was calculated with seeded precursor particles, which possesses quenched state fluorophores, not with free fluorophores. Furthermore maximum enhancement factor value ~16-fold obtained by such a process is not very useful for practical application.

Here, we have designed and synthesized Ag-based multilayered alternative nanoplasmonic-nanodielectric fluorescence amplifiers (MANNA) that can produce a robust and reproducible PEF signal over a wide range of excitation wavelengths. As a proof of concept, fluorophores with various excitation wavelengths from 546 nm to 790 nm were used, and a significant degree of enhancement factors (EFs) was obtained for the entire range. Especially for NRI fluorophore case, it showed  $\sim 10^3$  fluorescence EF, which is difficult to attain in ensemble measurements in PEF research. The results of computational modeling through the boundary-element method matched well with the experimental results, which guarantees the reliability of signal enhancement of the MANNA PEF platform.

## 3.2. Experimental Section

### Reagents and Materials

Ag nanoparticles were purchased from Ted Pella, Inc. Chemical reagents including AgNO<sub>3</sub>, polyvinylpyrrolidone (PVP), EtOH, DMSO, (3-aminopropyl)-triethoxysilane (APTES), N'-(3-trimethoxysilylpropyl)diethylenetriamine (DETA), dimethylamine, tetraethyl orthosilicate (TEOS), ascorbic acid, Tween 20, formaldehyde, 3-(Trihydroxysilyl)propyl methylphosphate (TPMP) were purchased from Sigma-Aldrich (St. Louis, MO, USA). NANOpure H<sub>2</sub>O (>18.0 MΩ), purified using a Milli-Q water purification system, was used for all experiments. Alexa Fluor<sup>TM</sup> carboxylic acid, succinimidyl ester fluorophores were purchased from Molecular Probes (Eugene, Oregon, USA). The formvar/carbon coated copper grid (Ted Pella, Inc. Redding, CA, USA), TEM images were obtained using JEM-2100 (JEOL, Japan, 200 kV). Inductively coupled plasma emission spectrometer (ICP-ES, ICPS-7510, Shimadzu, Japan) was used to measure the mass concentration of AuNRs, and the steady state spectrofluorometer (FS5 Spectrofluorometer, Edinburgh Instruments Ltd, Kirkton Campus, UK) was used for fluorescence measurements.

### Preparation of Ag-SiO<sub>2</sub> core-shell nanoparticles

We first coated spherical Ag nanoparticles with polyvinylpyrrolidone (PVP, mw~40,000) in order to stabilize the particles in the EtOH solvent because silica shell formation proceeded in EtOH solvent. For this, 1.0 ml of 20 nm spherical Ag nanoparticles were mixed with 1.0 ml of 2.5 wt. % PVP solution, 1 ml of 1 mM AgNO<sub>3</sub> solution, 1.0 ml of 1 mM ascorbic acid, 1.0 ml of 10 mM NaCl solution and incubated for 1 hour at 60 °C. The solution was centrifuged at 6000 g for 10 min and redispersed in 1.0 ml of EtOH. In this step, Ag nanoparticle's diameter increased to 50 nm. After that, the PVP-coated Ag nanoparticles were coated with fluorescent

silica shell. For fluorescent silica shell, 2  $\mu\text{l}$  of 0.5 % (v/v, in EtOH) (3-aminopropyl)-triethoxysilane (APTES) was mixed with 40.0  $\mu\text{l}$  of carbonate buffer (pH 8.5) and 10  $\mu\text{l}$  of 0.8 mM (in DMF) carboxylic succinimidyl ester-tagged Alexa Fluor. After 12-hour incubation under room temperature, the solution was mixed with 400  $\mu\text{l}$  of 0.1 nM PVP-coated Ag nanoparticles and incubated for 30 minutes. After that, 450  $\mu\text{l}$  of EtOH, 10  $\mu\text{l}$  of 0.6 % (v/v, in EtOH) tetraethyl orthosilicate, 25.0  $\mu\text{l}$  of dimethylamine solution, and 50.0  $\mu\text{l}$  were added. The solution was incubated at 30 °C. After 2 hour incubation, 25  $\mu\text{l}$  of 0.25% (v/v, in EtOH) tetraethyl orthosilicate added and the solution was further incubated at 30 °C for 12 hours. The solution was mixed with 650  $\mu\text{l}$  of DMSO and centrifuged two times (5000 rpm, 15 min) and redispersed in 50.0  $\mu\text{l}$  of DMSO.

### **Preparation of DETA-coated Ag-SiO<sub>2</sub> core-shell nanoparticles**

At first, 50.0  $\mu\text{l}$  of prepared Ag-SiO<sub>2</sub> core-shell nanoparticle solution was mixed with 400  $\mu\text{l}$  of 1.0 % tween 20 (v/v, in DMSO), 4.0 wt. % dimethylamine (v/v, in DMSO), and  $5.0 \times 10^{-5}$  % DETA (v/v, in DMSO). The solution was incubated for 2 hours at 30 °C. After that, the solution was centrifuged two times (6000 g, 15 min) and redispersed in 50.0  $\mu\text{l}$  of deionized water (DIW).

### **Ag shell formation on DETA-coated Ag-SiO<sub>2</sub> core-shell nanoparticles**

For silver shell formation, 100  $\mu\text{l}$  of 0.25 nM of DETA-coated Ag-SiO<sub>2</sub> nanoparticles were mixed with 100  $\mu\text{l}$  of 1.0 mM AgNO<sub>3</sub> solution and incubated for 10 min. After that, 100  $\mu\text{l}$  of 0.37 wt. % formaldehyde solution and 100  $\mu\text{l}$  of 0.2 wt. % dimethylamine solution were added and incubated for 1 hour at room temperature. the solution was centrifuged two times (1000 g, 15 min) and redispersed in 100  $\mu\text{l}$  of deionized water (DIW).

## Fluorescence measurements

To analyze fluorescence activity and determine fluorescence enhancement factors, the steady state spectrofluorometer (FS5 Spectrofluorometer, Edinburgh Instruments Ltd, Kirkton Campus, UK) was used.

## Simulation Method

The electric near-field, radiative enhancement, and QY were calculated with the boundary-element method using the MNPBEM toolbox. Since the metal-enhanced fluorescence consists of two steps, (enhanced electric field, and quenching due to the plasmonic nanoparticle), the enhancement factor of each fluorophore is represented as,

$$EF = \left( \frac{|\vec{p}(\lambda_{em}) \cdot \vec{E}(\lambda_{exc}, \vec{r})|}{|\vec{p}(\lambda_{em}) \cdot \vec{E}_0(\lambda_{exc}, \vec{r})|} \right)^2 \frac{Q_r}{Q_r^0}$$

where  $\lambda_{exc}$ ,  $\lambda_{em}$  are excitation, emission wavelengths,  $\vec{p}$  is the electric dipole moment of a fluorophore.  $\vec{E}$  ( $\vec{E}_0$ ) is the incident electric field in the presence (absence) of the MANNA,  $\vec{r}$  is the positions of the fluorophores.  $Q_r$  ( $Q_r^0$ ) is the QY of the fluorophore molecule in the presence (absence) of the MANNA.  $Q_r$  is calculated from the radiative decay rate divided by total decay rate, and we used  $Q_r^0$  values notified by the company. We only considered three principal axes as the dipole orientations and transverse polarization of the incident light.

### 3.3. Results and Discussion

#### Synthesis of MANNAs

Creating core-shell hybrid structures of Ag and silica is generally difficult because of the low affinity between Ag and silica.<sup>26</sup> And in particular, forming Ag shells on silica layer often produces extremely non-uniform materials with low yield.<sup>27,28</sup> In order to build Ag-based highly uniform multilayered nanostructures, we introduced N'-(3-trimethoxysilylpropyl)diethylenetriamine (DETA) on a silica shell layer (Figure 3.1.) The DETA can be covalently bound to the silica surface through silylation reaction, and the diethylenetriamine moiety of DETA forms intermolecular transition metal ion chelation environment composed of two equivalent ethylenediamine ligands.<sup>29</sup> When Ag<sup>+</sup> ions are inserted into the solution after DETA is introduced into the silica surface, the ion concentration in the vicinity of the nanoparticles increases through the process of forming complex ions. We overcome the problem of low affinity between Ag and silica layer by using a molecule with high affinity for Ag<sup>+</sup> ion.

In the first synthetic step, fluorescent silica shells were formed on spherical Ag nanoparticles (Figure 3.2). 3-aminopropyltriethoxysilane (APTES) was reacted with Alexa fluor with carboxylic succinimidyl ester group, and a fluorescent silica shell was designed to surround spherical silver nanoparticles using the Stöber method with slight modifications. At this step, 3-(trihydroxysilyl)propyl methylphosphate (TPMP) was required to obtain homogenous Ag-SiO<sub>2</sub> core-shell nanoparticles (Figure 3.3). TPMP is a negatively charged silane group molecule, which induces electrostatic repulsion between nanoparticles in the process of forming a silica shell on the surface of Ag nanoparticles, helping the synthesized nanoparticles to have ultrahigh dispersity. In the absence of TPMP, it was frequently confirmed that two or more Ag nanoparticles existed in a multimeric form in a single silica shell. In conclusion, the Ag-SiO<sub>2</sub> core-shell nanoparticles synthesized by adding TPMP dominantly

included only one Ag nanoparticle (Figure 3.2b), and the extinction spectrum was also similar to the spherical Ag nanoparticles before the silica shell was deposited (Figure 3.2c). The weak red shift of the SPR peak seen in the extinction spectrum is due to the refractive index changed by silica shell surrounding the Ag core surface.<sup>30</sup>

Next, DETA was coated on the silica layer as a preparation for silver shell formation. The coating step was performed in DMSO solvent, and the surface charge of the nanoparticles before and after DETA fixation was changed from -13.35 ( $\pm 0.64$ ) to +17.6 ( $\pm 0.42$ ). After introducing DETA, the nanoparticles were dispersed in deionized water and incubated with Ag<sup>+</sup> ion for 10 minutes to combine Ag<sup>+</sup> and ethylenediamine by complex ion formation. After that concentrated Ag<sup>+</sup> ions on the surface of silica layer were reduced by formaldehyde (HCHO) and dimethylamine (DMA) in a solution where tween 20 functions as a stabilizer.

After 1 hour incubation, highly uniform and dispersive multilayered alternative nanoplasmonic-nanodielectric amplifiers (MANNAs) were produced (Figure 3.4). The synthesized MANNAs were averagely 52 nm (Ag core) -32 nm (SiO<sub>2</sub> layer) -12 nm (Ag shell) size, and difference in contrast of the multilayer was confirmed by TEM. Note that even after forming the Ag shell, the nanoparticles showed extremely homogeneous monomer distribution. As a result of analyzing a total of 672 particles based on the TEM images, 97.8 percent of the particles contained only one Ag-SiO<sub>2</sub> nanoparticle in the outermost silver shell structure, and this is because the electrostatic repulsive force due to TPMP and DETA that prevents nanoparticles from aggregation due to in the formation step of the first and second shells respectively. In Figure 3.4(b), simulated and experimental extinction spectra of MANNA was compared. The synthesized MANNA has SPR peaks corresponding to dipoles at 820 nm and 440 nm, which is similar to the multilayered structure made of Au.<sup>14</sup> It is noteworthy that at 600 nm, a quadrupole mode, which was not found in the general plasmonic multilayer structure, was experimentally discovered. The discovery of the quadrupole mode consistent with the

simulation results from the solution-based ensemble measurement is another important evidence that contains the uniformity of the MANNA structure.

## **Fluorescence analysis of MANNAs**

In order to prove the PEF activity in the broad wavelength range of MANNAs, we selected four fluorophores with different excitation and emission wavelengths, and their maximum excitation and emission wavelengths are indicated in the Figure 3.5. We named four different MANNAs according to the maximum emission wavelength of the inserted fluorophores (MANNA<sub>546</sub>, MANNA<sub>647</sub>, MANNA<sub>750</sub>, MANNA<sub>790</sub>), and the fluorescence intensities of MANNAs were compared with free dyes for calculating fluorescence EFs (Figure 3.6). To measure free dye fluorescence intensities, we treated MANNAs with potassium cyanide (KCN) to completely dissolve Ag atoms in nanostructures by chelation-mediated melting process. In conclusion, enhancement factors of 5.3-fold, 97.2-fold, 404.8-fold, and 2985.7-fold were obtained from MANNA<sub>546</sub>, MANNA<sub>647</sub>, MANNA<sub>750</sub>, and MANNA<sub>790</sub>, respectively. A fluorescence EF of  $\sim 10^3$ -fold is an extremely high value that is difficult to obtain by colloidal fluorescence measurements based on wet chemical synthesis in PEF,<sup>31,32</sup> except for single molecule or single particle-based experiments.<sup>33,34</sup>

To investigate the rationale of the high fluorescence EFs of MANNAs, we performed a near-field electric field map analysis and average EF calculation with the boundary-element method using the MNPBEM toolbox (Figure 3.7). The near-field electric field distributions were calculated at the four emission wavelengths during which the actual fluorescence measurements were made (520 nm, 620 nm, 725 nm, and 765 nm). In common in the four excitation wavelengths near-field images, the electromagnetic field density was high in the area between the core and the outer shell, and in general, the closer to the core, the higher the electromagnetic field density. Also, a stronger electromagnetic field was generated in the

dielectric layer toward the long wavelengths, which coincided with the trend of PEF activity according to the emission wavelength of MANNA. In addition to near-field, the fluorescence EFs are largely influenced by radiative enhancement and quantum yield. Therefore, considering these factors, we simulated the average EFs of fluorophores randomly distributed in the dielectric layer (Figure 3.7b). The average calculated EF results were consistent with the trend of EFs gained by the experimental measurements according to the excitation wavelength. The calculated values at all four wavelengths were lower than the experimental values, which implies that the actual positions of the fluorophores in the MANNA structures are not randomly distributed, but are located near the core surface with a higher probability.

### 3.4. Conclusions

We developed the high yield synthetic strategies for plasmonic multilayer-based fluorescence amplifier. The two silane group molecules, TPMP and DETA, played a major role in the extremely homogeneous synthesis of Ag-based multilayered alternative nanoplasmonic-nanodielectric nanostructures during the formation of silica and silver shells, In the nanostructure where the Ag layer and the silica dielectric layer are alternately located, the fluorescence signal in the broad wavelength range was enhanced efficiently. In a fluorescence experiment using four different types of fluorophores, a fluorescence EFs of 5 or more could be obtained for all regions, and in particular, EF up to  $10^3$ -fold was found in the NIR fluorophore. The fluorescence amplification process using MANNAs was explained through boundary-element method-based simulation, and it was confirmed that the experimental PEF activity trend is well-matched with calculation results. The strategies and results presented here with MANNAs provide a reliable designing principle and synthetic method for PEF-active nanostructures, suggesting the potential for more universal and reproducible applications of PEF.

### 3.5. References

- [1] M. Ha, J. H. Kim, M. You, Q. Li, C. Fan, J. M. Nam, *Chem. Rev.* **2019**, *119*, 12208.
- [2] D. Wei, S. Chen, Q. Liu, *Appl. Spectrosc. Rev.* **2015**, *50*, 387.
- [3] D. Chorvat Jr., A. Chorvatova, *Laser Phys. Lett.* **2009**, *6*, 175.
- [4] C. D. Geddes, J. R. Lakowicz, *J. Fluoresc.* **2002**, *12*, 121.
- [5] T. Ming, H. Chen, R. Jiang, Q. Li, J. Wang, *J. Phys. Chem. Lett.* **2012**, *3*, 191.
- [6] E. Fort, S. Grésillon, *J. Phys. D. Appl. Phys.* **2008**, *41*, DOI 10.1088/0022-3727/41/1/013001.
- [7] J.-F. Li, C.-Y. Li, R. F. Aroca, *Chem. Soc. Rev.* **2017**, *46*, 3962.
- [8] M. A. Badshah, N. Y. Koh, A. W. Zia, N. Abbas, Z. Zahra, M. W. Saleem, *Nanomaterials* **2020**, *10*, 1.
- [9] Y. Zhang, A. Dragan, C. D. Geddes, *J. Phys. Chem. C* **2009**, *113*, 15811.
- [10] J. Lee, S. Lee, M. Jen, Y. Pang, *J. Phys. Chem. C* **2015**, *119*, 23285.
- [11] A. I. Dragan, B. Mali, C. D. Geddes, *Chem. Phys. Lett.* **2013**, *556*, 168.
- [12] N. Fontaine, A. Picard-Lafond, J. Asselin, D. Boudreau, *Analyst* **2020**, *145*, 5965.
- [13] L. Pezzi, M. A. Iatì, R. Saija, A. De Luca, O. M. Maragò, *J. Phys. Chem. C* **2019**, *123*, 29291.
- [14] C. Ayala-Orozco, J. G. Liu, M. W. Knight, Y. Wang, J. K. Day, P. Nordlander, N. J. Halas, *Nano Lett.* **2014**, *14*, 2926.
- [15] A. K. Kodali, X. Llorca, R. Bhargava, *Proc. Natl. Acad. Sci.* **2010**, *107*, 13620 LP.
- [16] D.-K. Lim, K.-S. Jeon, J.-H. Hwang, H. Kim, S. Kwon, Y. D. Suh, J.-M. Nam, *Nat. Nanotechnol.* **2011**, *6*, 452.
- [17] D.-K. Lim, K.-S. Jeon, H. M. Kim, J.-M. Nam, Y. D. Suh, *Nat. Mater.* **2010**, *9*, 60.
- [18] L. Lin, H. Gu, J. Ye, *Chem. Commun.* **2015**, *51*, 17740.
- [19] Z. Jian, L. Jian-jun, Z. Jun-wu, *Plasmonics* **2011**, *6*, 527.

- [20] J. Zhou, Q. Xiong, J. Ma, J. Ren, P. B. Messersmith, P. Chen, H. Duan, *ACS Nano* **2016**, *10*, 11066.
- [21] M. K. Lee, T. Y. Jeon, C. W. Mun, J. D. Kwon, J. Yun, S. H. Kim, D. H. Kim, S. C. Chang, S. G. Park, *RSC Adv.* **2017**, *7*, 17898.
- [22] P. Anger, P. Bharadwaj, L. Novotny, *Phys. Rev. Lett.* **2006**, *96*, 3.
- [23] A. I. Dragan, E. S. Bishop, J. R. Casas-Finet, R. J. Strouse, J. McGivney, M. A. Schenerman, C. D. Geddes, *Plasmonics* **2012**, *7*, 739.
- [24] R. A. Alvarez-Puebla, N. Pazos-Perez, L. Guerrini, *Appl. Mater. Today* **2018**, *13*, 1.
- [25] R. Jiang, H. Chen, L. Shao, Q. Li, J. Wang, *Adv. Mater.* **2012**, *24*, 200.
- [26] K. Aslan, M. Wu, J. R. Lakowicz, C. D. Geddes, *J. Am. Chem. Soc.* **2007**, *129*, 1524.
- [27] J. Zhang, Y. Fu, J. R. Lakowicz, *J. Phys. Chem. C. Nanomater. Interfaces* **2009**, *113*, 19404.
- [28] J. Zhang, Y. Fu, F. Mahdavi, *J. Phys. Chem. C* **2012**, *116*, 24224.
- [29] Y. Choi, Y. Park, T. Kang, L. P. Lee, *Nat. Nanotechnol.* **2009**, *4*, 742.
- [30] D. Acharya, B. Mohanta, *AIP Conf. Proc.* **2017**, *1832*, 50155.
- [31] J. F. Li, C. Y. Li, R. F. Aroca, *Chem. Soc. Rev.* **2017**, *46*, 3962.
- [32] J. Dong, Z. Zhang, H. Zheng, M. Sun, *Nanophotonics* **2015**, *4*, 472.
- [33] G. M. Akselrod, C. Argyropoulos, T. B. Hoang, C. Ciraci, C. Fang, J. Huang, D. R. Smith, M. H. Mikkelsen, *Nat. Photonics* **2014**, *8*, 835.
- [34] Y. Wu, J. Xu, E. T. Poh, L. Liang, H. Liu, J. K. W. Yang, C. W. Qiu, R. A. L. Vallée, X. Liu, *Nat. Nanotechnol.* **2019**, *14*, 1110.

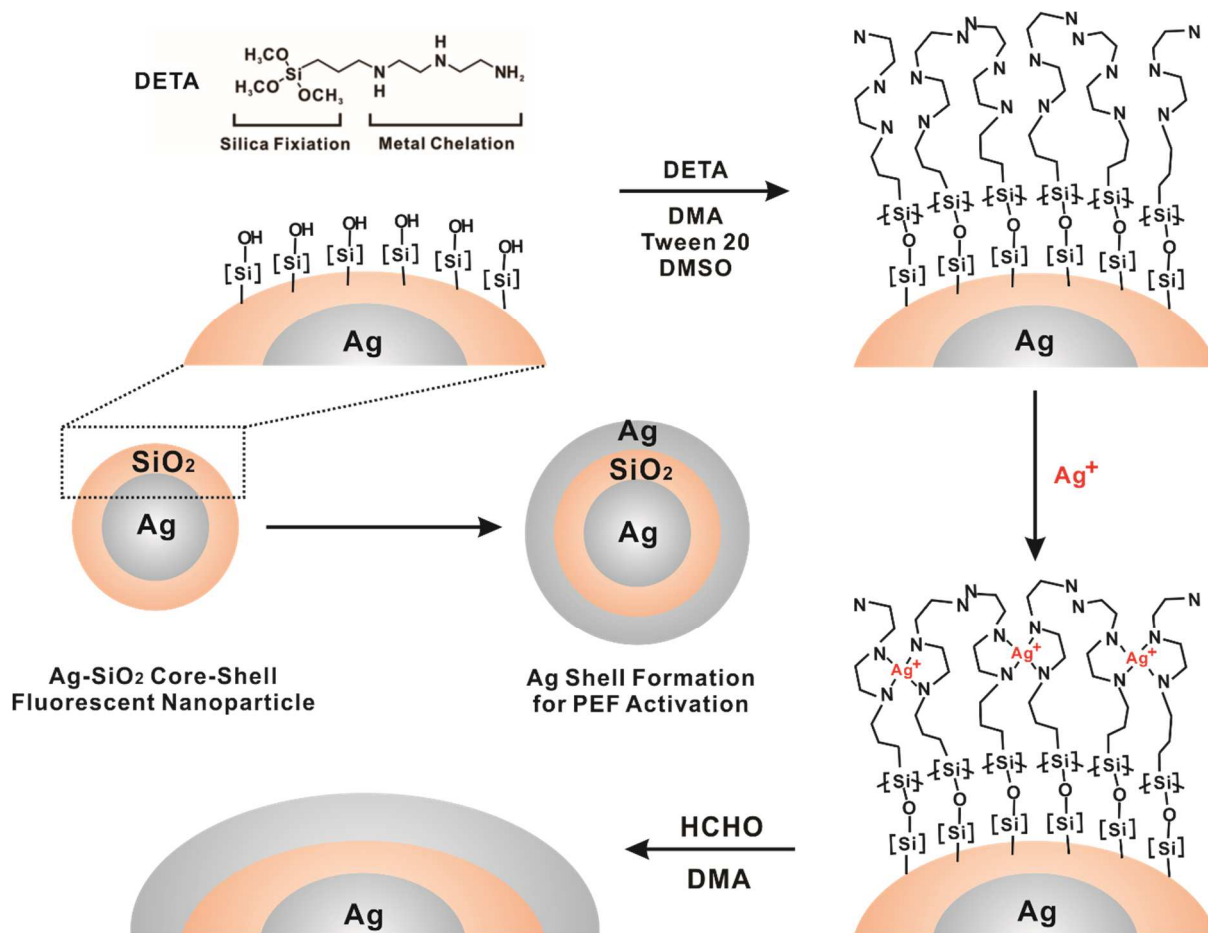


**Figure 3.1.** Schematic illustration of synthetic process of multilayered alternative nanoplasmonic-nanodielectric amplifiers (MANNAs) for broad wavelength range plasmon-enhanced fluorescence. In this scheme, N'-3-trimethoxysilylpropyl)diethylenetriamine (DETA) coating on silica shell layer induces metal ion chelation, making it possible to form a uniform Ag shell on silica layer.

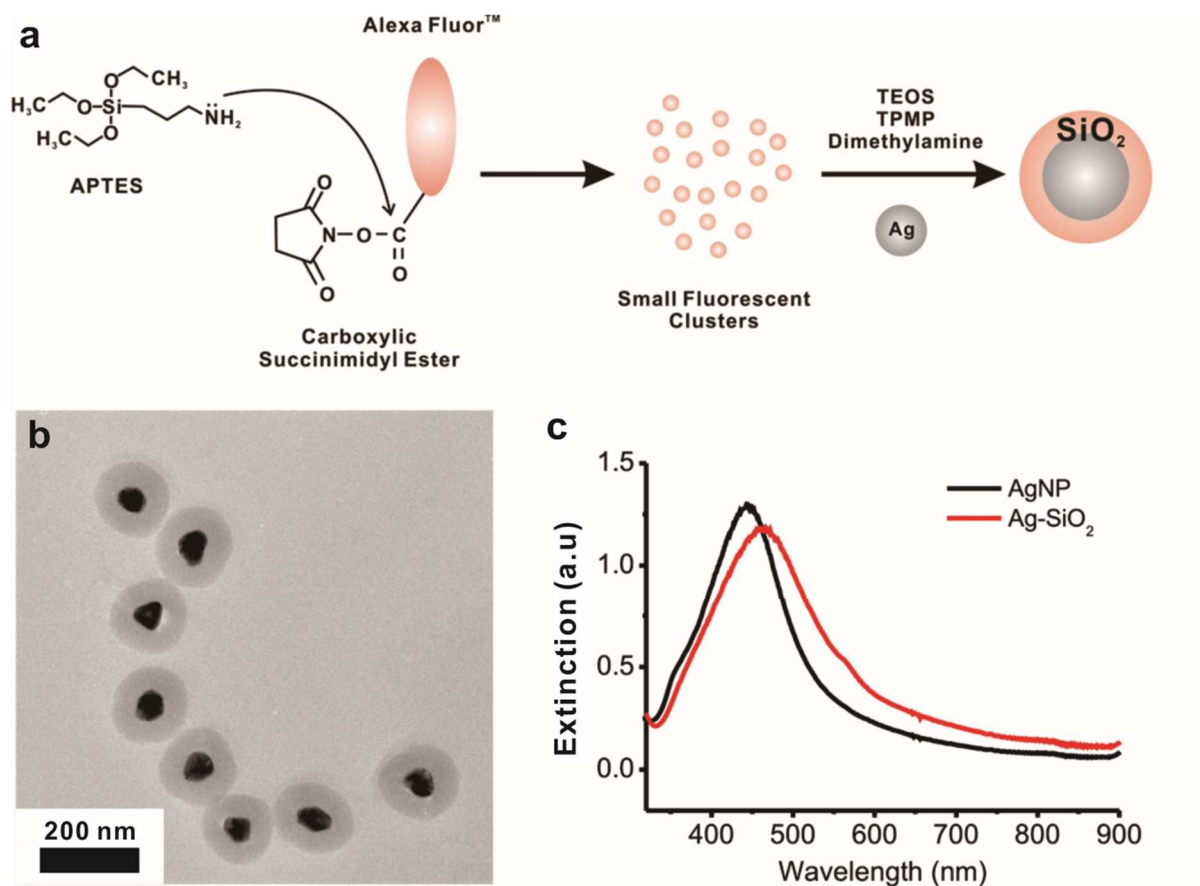


**Figure 3.2.** Synthesis of Ag-fluorescent SiO<sub>2</sub> nanoparticles. Schematic illustration of fluorescent silica shell formation of spherical Ag nanoparticle (a), The TEM image of Ag-fluorescent SiO<sub>2</sub> core-shell nanoparticles (b) and extinction spectrum of spherical Ag nanoparticles and Ag-fluorescent SiO<sub>2</sub> core-shell nanoparticles.

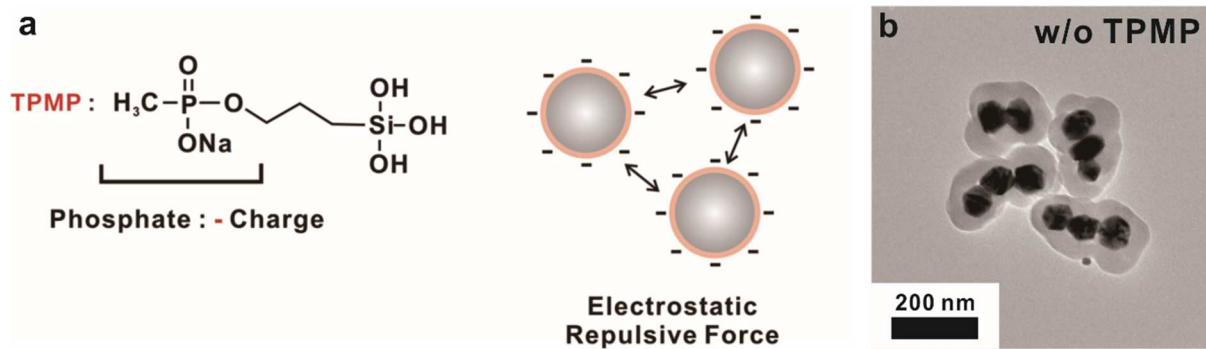


**Figure 3.3.** A strategy for securing high dispersity in the process of forming silica shell step. A negatively charged 3-(trihydroxysilyl)propyl methylphosphate (TPMP) plays a role of preventing Ag nanoparticles from adhering to each other by generating an electrostatic repulsive force between particles in the process of forming silica shells on spherical Ag nanoparticles.

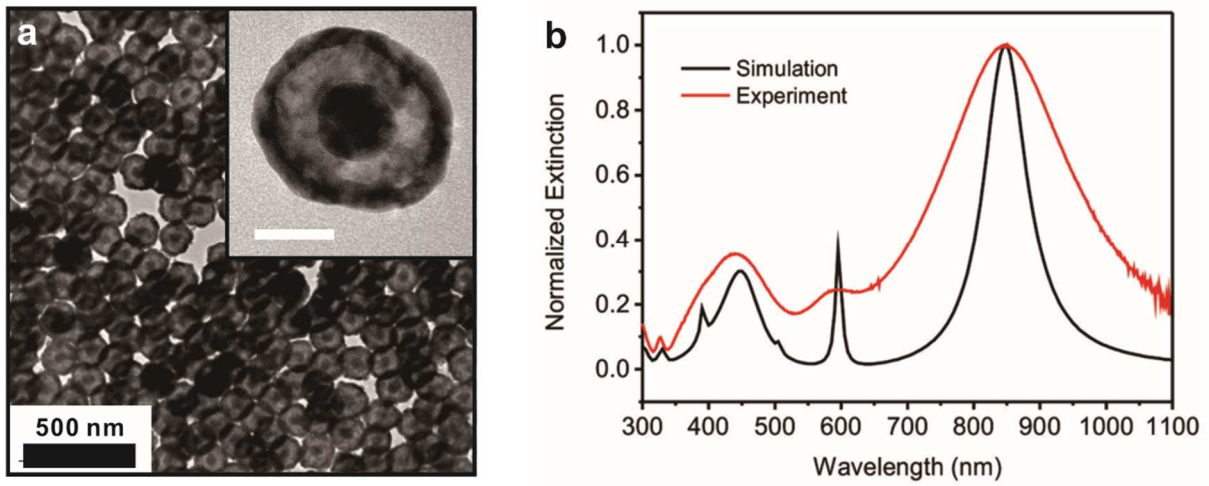


**Figure 3.4.** Characterization of Ag-SiO<sub>2</sub>-Ag MANNA. The TEM images (a) and normalized extinction (b) analysis of MANNA. In (b), simulated normalized extinction of MANNA is well-matched with experimental measurement. Scale bar in inset of (a) is 50 nm.

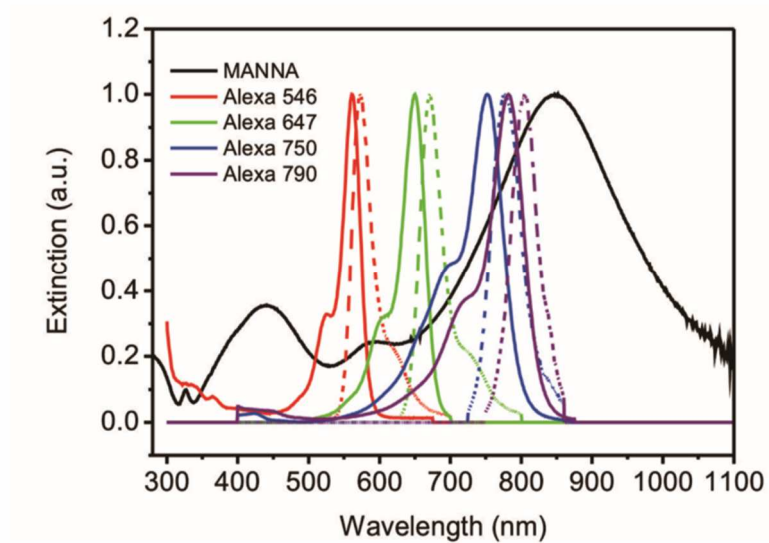


**Figure 3.5.** Selection of broad wavelength range of fluorophores. The excitation and emission spectra of used fluorophores are shown with extinction spectrum of MANNA.

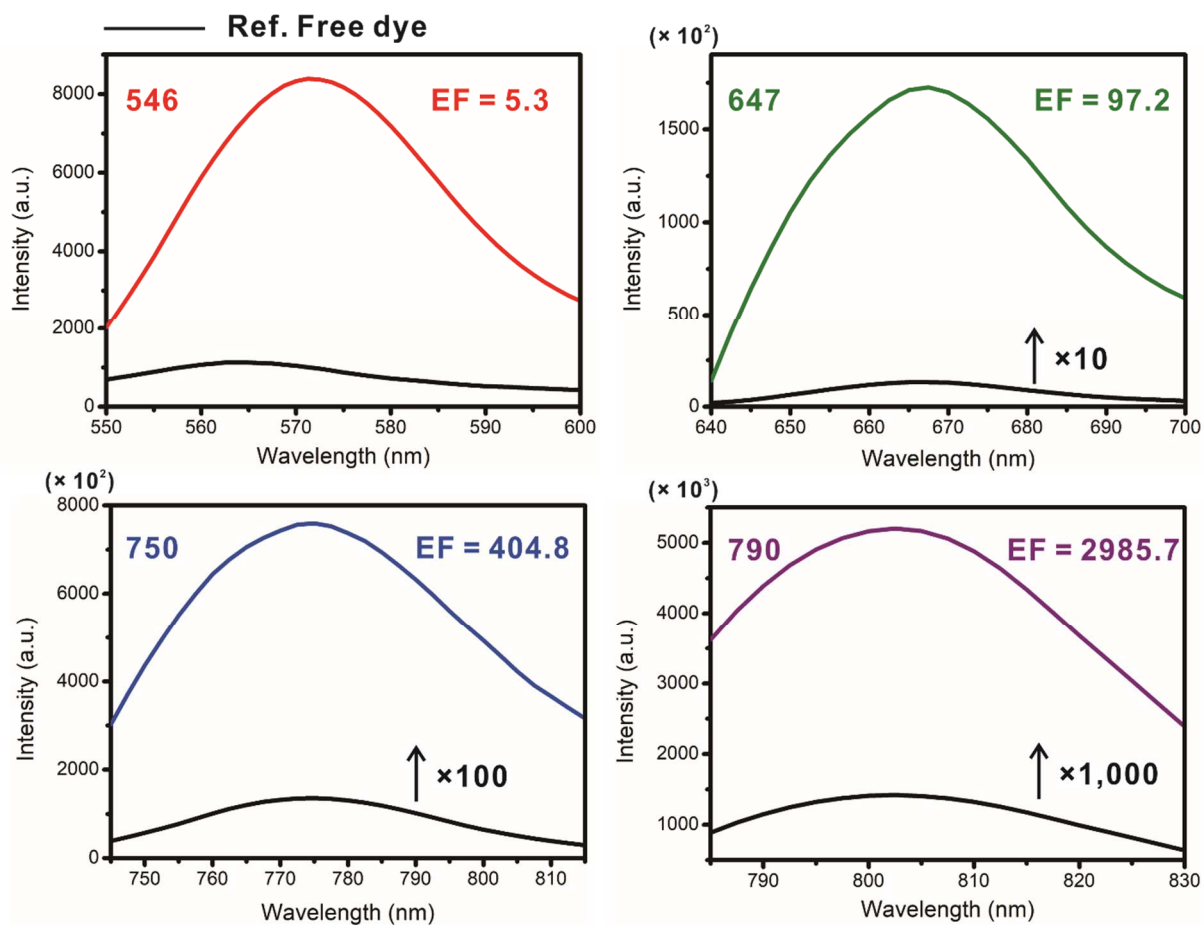


**Figure 3.6.** Fluorescence measurements of MANNAs with four different types of fluorophores. Excitation wavelength in measurements are 520 nm, 620 nm, 725 nm and 765 nm for MANNA<sub>546</sub>, MANNA<sub>647</sub>, MANNA<sub>750</sub> and MANNA<sub>790</sub> respectively.

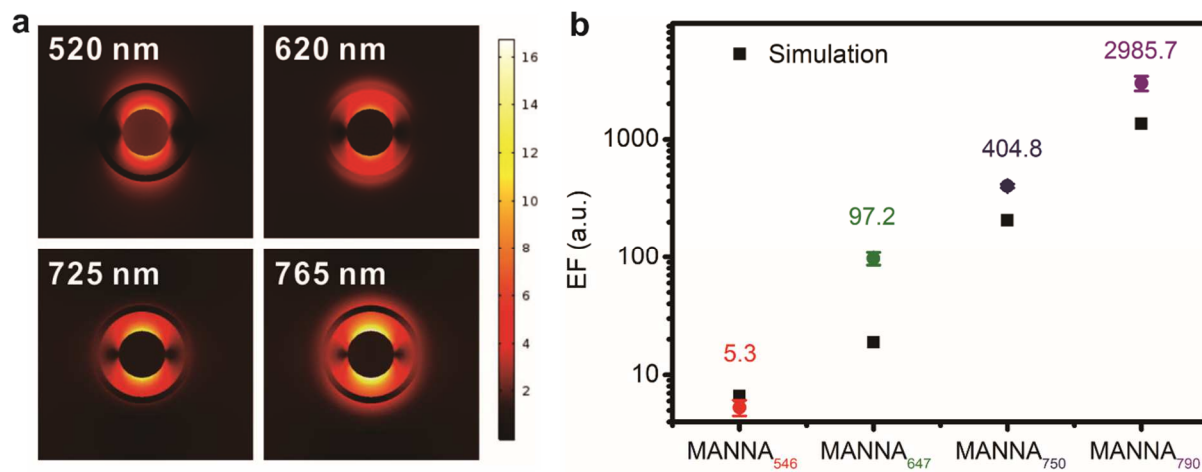


**Figure 3.7.** Simulation analysis of MANNA's fluorescence signal amplification. The near-field images of MANNA at the four different excitation wavelengths used in the fluorescence measurements (a) and comparison of EFs obtained by experiments and calculation (black).

## 국 문 초 록

### 플라즈몬 강화 형광 활성 나노구조의 합성 및 응용

플라즈몬 강화 형광(Plasmon-enhanced Fluorescence)은 플라즈모닉(plasmonic) 나노구조체에 근접해 위치한 형광체의 광신호가 증폭되는 현상을 일컫는다. 일반적으로 플라즈모닉 나노구조는 탄성 산란(elastic scattering)의 형태로 외부 빛에 반응하기 때문에 자체적인 형광 발광 정도는 매우 낮다. 그러나 국소 표면 플라즈몬 공명(localized surface plasmon resonance, LSPR)은 플라즈모닉 나노구조 주위에 전자기장을 고도로 밀집시킴으로써 형광체의 신호가 증폭될 수 있는 환경을 제공한다. 1980년대 초에 처음 발견된 플라즈몬 강화 형광은, 수십 년의 연구 기간을 거치는 동안 형광체의 신호 증폭 효율을 결정하는 요소들이 밝혀지며 최대 1,000,000 배에 달하는 광 신호 증폭 효과를 나타내 큰 주목을 받고 있다. 본 학위논문은 플라즈모닉 나노구조체를 기반으로 고효율의 플라즈몬 강화 형광 활성 나노구조를 제작하고 이를 응용한 연구내용을 담고 있다.

제 1 장에서는 제 2 장과 제 3 장에서 수행한 연구 내용을 이해하는 데에 도움이 되는 플라즈몬 강화 형광에 대한 배경 사항을 기술하였다. 구체적으로, 플라즈몬 강화 형광의 이론적 배경·광신호의 증폭 효율을 결정하는 주요한 요소·플라즈몬 강화 형광 활성 나노구조체의 예시·플라즈몬 강화 형광의 응용 예시가 요약되어 있다.

제 2 장에서는 데옥시리보핵산(deoxyribonucleic acid, DNA)을 매개로 하여  
강하고 정량적인 플라즈몬 강화 형광 신호를 방출하는 핵-껍질(core-shell)  
나노직육면체(nanocuboid)를 합성하고 이를 마이크로어레이(microarray) 기반  
마이크로알엔에이(microRNA) 검출에 응용한 연구 내용을 기술하였다.

제 3 장에서는 넓은 파장 범위의 플라즈몬 강화 형광 활성을 갖는 은 기반 다층  
나노구조를 고수율로 균일하게 합성한 연구내용을 기술하였다.

제 2 장과 제 3 장의 연구 내용은 공통적으로 플라즈몬 강화 형광 현상의 실제적  
응용을 궁극적인 목표로 설정하고 수행하였다. 제작된 플라즈몬 강화 형광 나노구조가  
실제적으로 활용되기 위해서는 합성된 결과물이 균일하고 안정적인 신호를 발생해야  
한다. 또한 단순한 신호의 증폭 여부를 확인하는 것에 더하여, 실제적 응용 상황에서  
기준에 사용되던 형광 물질에 비교 우위가 있는지를 증명하는 것이 필요하다. 제  
2 장에서의 마이크로어레이 기반 마이크로 RNA 검출 결과는 기준에 활용되는  
형광체와의 동일한 조건에서의 비교를 통해 성능 우위를 직접적으로 증명한 사례로서  
중요한 의미를 갖는다고 할 수 있다.

주요어 : 플라즈몬 강화 형광, 플라즈모닉 나노구조, 바이오응용, 마이크로 RNA 검지,  
광신호 증폭

학번 : 2009-20319